On the Magnetic Control of Endoscopic Robots

By

Piotr Robert Slawinski

Dissertation

Submitted to the Faculty of the

Graduate School of Vanderbilt University

in partial fulfillment of the requirements

for the degree of

DOCTOR OF PHILOSOPHY

in

Mechanical Engineering

August 9, 2019

Nashville, Tennessee

Approved:

Pietro Valdastri Ph.D.

Nabil Simaan Ph.D.

Keith L. Obstein M.D., M.P.H., F.A.S.G.E, F.A.C.G.

Nilanjan Sarkar Ph.D.

Thomas J. Withrow Ph.D.

ACKNOWLEDGMENTS

In the years leading up to the completion of this dissertation, I have been positively influenced by several individuals whom I will acknowledge here.

First, I extend my gratitude to my research advisors: Drs. Pietro Valdastri, Keith Obstein, and Nabil Simaan. Each of these individuals provided critical input on the overarching goals of the work as well as its implementation. I am indebted to my advisors for the support and the intellectual feedback they have provided over the years. I thank Pietro for bringing me into the STORM lab and providing me with countless learning opportunities, and Keith for his support, encouragement, and advice.

My gratitude goes out to fellow members of the STORM lab: Addisu Taddese, Federico Campisano, Gregorio Aiello, Kyle Musto, Joseph Norton, James Martin, Bruno Scaglioni, Lavinia Barducci *et al.* who have provided advice, assistance, encouragement, and camaraderie over the years. My PhD experience was vastly improved through my collaboration with Addisu on the magnetic endoscope project. Addisu has been both a mentor and dear friend. His innate curiosity, guidance, and selflessness enhanced the day-to-day lab life and encouraged the exchange of ideas that led to parts of this dissertation. I thank Federico for the countless discussions, advice, and help throughout our years in the lab. I thank the members of A.R.M.A. lab for their friendship and discussions, as well as Myrtle Daniels, Jean Miller and Chris Lindsey for their assistance.

My graduate school experience may not have been possible without the influence of Dr. Benjamin Terry. My first research experience was in Ben's lab where, even though I was a new undergraduate student, he entrusted me with leading a project; an experience that eventually led to my desire to study robotics at a graduate level. I wish to also acknowledge Dr. Shane Farritor for his guidance over the years.

I thank my girlfriend Ella Wesly for her encouragement during my final years of graduate school. My days were made brighter by having her by my side. Finally, I thank my dear parents, Iwona and Robert, for their support, patience, and hard work that allowed for my academic journey

to continue to this point. This dissertation would not have been possible without the sacrifices they have made throughout my life.

Acknowledgements of specific contributions (not including advisors):

- **Chapter 2:** Dr. Addisu Z. Taddese lead development of a mathematical foundation of magnetic control work and their initial validations [1, 2], to which I contributed in a second-author role.

- **Chapter 3:** Dr. Taddese contributed to the retroflexion work in terms of method-development and conducting experiments. Kyle B. Musto, then an undergraduate researcher in STORM Lab, made significant contributions to optimization strategy, algorithm development, and benchtop experimentation of the retroflexion approach.

- **Chapter 4:** The work of this chapter was a collaborative one with Dr. Joseph C. Norton who is currently a postdoctoral researcher at the University of Leeds. Dr. Norton lead project management, device design (to which I contributed), and experimental design (to which I contributed). Dr. Norton developed the media, outside of data, for the manuscript that came out of this work. Mr. James W. Martin contributed to the experimental validations in this work.

- **Chapter 6:** Dr. Taddese provided useful discussions on estimation strategies that inspired the direction of the project.

Acknowledgements of funding sources: I would like to also thank the funding mechanisms that enabled my graduate work: The National Institute of Biomedical Imaging and Bioengineering, USA of the National Institutes of Health under award no. R01EB018992, and National Science Foundation, USA under grant no. CNS-1239355 and no. IIS-1453129, and National Science Foundation Graduate Research Fellowship Program under grant no. 1445197. Any opinions, findings, conclusions, or recommendations expressed in this dissertation are my owrn and do not necessarily reflect the views of the National Institutes of Health or the National Science Foundation.

TABLE OF CONTENTS

LIST OF TABLES

LIST OF FIGURES

LIST OF ABBREVIATIONS

μUS	microultrasound
ADR	Adenoma detection rate
CL	closed-loop
CT	computed tomography
DoF	degree-of-freedom
EFA	echo-finder algorithm
EM	extracorporeal magnet
EPM	extracorporeal permanent magnet
EUS	endoscopic ultrasound
FBG	fiber Bragg gratings
FE	flexible endoscope
GI	gastrointestinal
IBD	inflammatory bowel diseases
IM	intracorporeal magnet
IPM	intracorporeal permanent magnet
MFE	magnetic flexible endoscope
MRI	magnetic resonance imaging
OL	open-loop
PET	positron emission tomography

RCE	robotic capsule endoscope
ROS	Robotic Operating System
TEFA	translational echo-finder algorithm
US	ultrasound

Chapter 1

Introduction

1.1 Motivation and Related Work

The magnetic actuation of medical robots has become a prevalent area of research that has found its way to the clinical setting. The first use of computer guidance using magnetic fields occurred in the late 1980s [8]. Magnetic fields provide a manner for applying forces and torques across a physical barrier, which lends itself well to minimally invasive procedures. Intracorporeal magnetic devices can be both translated and rotated using fields generated by extracorporeal sources. This also allows internal devices to maintain a small form factor as there is less of a need for actuation mechanisms or energy storage. Company-developed magnetic medical robot systems include the Niobe Stereotaxis system [9], the CGCI system from Magnetecs [10], and the Aeon Phocus system [11], each of which targets electrophysiology and cardiac catheter steering, as well as the NaviCam magnetic capsule system for gastric screening from Ankon Technologies [12]. Other applications from the research community include gastroenterology, opthamology, otolaryngology, and cardiology [5, 13, 14, 15, 16]. The use of magnetic resonance imaging scanners has also been investigated for actuating medical robots [17]. Recent advances in actuation systems and control systems make further adoption promising.

The medical application of the work in this dissertation is the screening, diagnostics, and therapeutics in the gastrointestinal (GI) tract, with emphasis on the large bowel. Diseases of the GI tract account for 8 million deaths annually worldwide and include cancer, hemorrhages, diverticulitis disease, GI infections, inflammatory bowel diseases (IBD), Crohns disease, ulcerative colitis, among others [18, 19]. Being the second most common cancer in women, and third in men, colon cancer makes up approximately a tenth of the annual global cancer incidence [20]. Studies have shown that lower endoscopy and stool-based screenings reduce the risk of death, and that the benefits of screening outweigh any risks associated with related procedures [20]. Lower endoscopies,

or colonoscopies, are carried out using a flexible endoscope (FE), Fig. 1.1, that consists of a semi-rigid shaft that is pushed from the rear to advance through the curves of the sigmoid colon, up the descending colon, around the splenic and hepatic flexures, down to the cecum. As the traversal path of the FE is convoluted, a highly flexible actuation device is desired; however, the FE must maintain rigidity to enable the translation of forces from the base to the tip. This typically results in the stretching of colon tissue, which is the main cause for procedural discomfort. Furthermore, instances arise when the tip of the FE does not translate while the endoscopist is advancing the shaft of the FE. This internal motion of the FE often results in colon looping which further stretches tissue and may cause tissue tears [21]. This internal motion is not intuitive to observe for the endoscopist as visualization occurs only at the tip.

Technologies for tracking the shape of the endoscope's body have been developed but are not widely used in the United States. Colonoscopy is generally regarded as a safe procedure-a benign intervention- in healthy patients with approximately 2% lifetime risk of complications from the procedure; however, in cases where patient's have been diagnosed with IBD, this risk rises to 12.7%, a significant increase [22, 23]. To reduce these numbers, a larger number of patients should undergo screening but in many cases choose not to for reasons such as indignity of the procedure, fear of related pain, bowel preparation discomfort, and a potential need for sedation [21]. The concept behind actuating a FE has not changed significantly since it was first introduced in 1957 [24]. In recent years, there has been a push in both academia as well as the industry to make colonoscopy more comfortable by preventing the application of excessive force to tissue, making the procedure easier for patients, and eliminate the need for sedation. Some industry devices for diagnostics of the lower bowel include the pressure-actuated GI-View Aer-O-Scope [25] and the inchworm-like Endotics system [26]. Devices with the capability for intervention include Consis Medical's inflatable semi-disposable endoscope [27] and the Invendoscope [28]. Several robotic approaches for endoscopy have been investigated in the academic community including wheeled actuation, legged crawling, propeller-based swimming, magnetic swimming, pneumatics, inchworm-crawling, and others. [14, 29, 30]. This dissertation is centered around a robotic endoscopy system based on

Figure 1.1: A flexible endoscope

magnetic actuation that was previously developed by the STORM lab [31].

Motion of magnetic devices results from an applied magnetic torque and force. The applied torque is proportional to the misalignment of a magnetic dipole's magnetization vector from an external magnetic field. The applied force is governed by the product of the flux density gradient and the magnetization vector. Field sources can be generated using electromagnets or permanent magnets where electromagnet-actuation relies on current control, potentially with motion control, to achieve desired field properties and permanent magnet-actuation relies on the relative motion of magnets to achieve a desired field and gradient. Electromagnets are typical in the actuation of micro-scale devices [32, 33, 34], and occasionally in meso-scale applications [35, 36, 37]. Systems that use electromagnets for actuation include MRI-scanners [36, 38, 39, 40] as well as custom-built coil systems [41, 33, 42, 43]. Permanent magnets have been primarily used in meso-scale applications (e.g. [44, 1, 45, 46, 3, 47]) and have an advantage of a more compact form factor as compared to an electromagnet of similar strength characteristics. Systems that rely on translating and rotating permanent actuating magnets are the focus of this dissertation. Magnetic actuation of this kind will be referred to as "mobile-dipole" actuation throughout this dissertation; "mobile" refers to the actuated motion of the actuating magnet, and "dipole" refers to the magnetic modelling

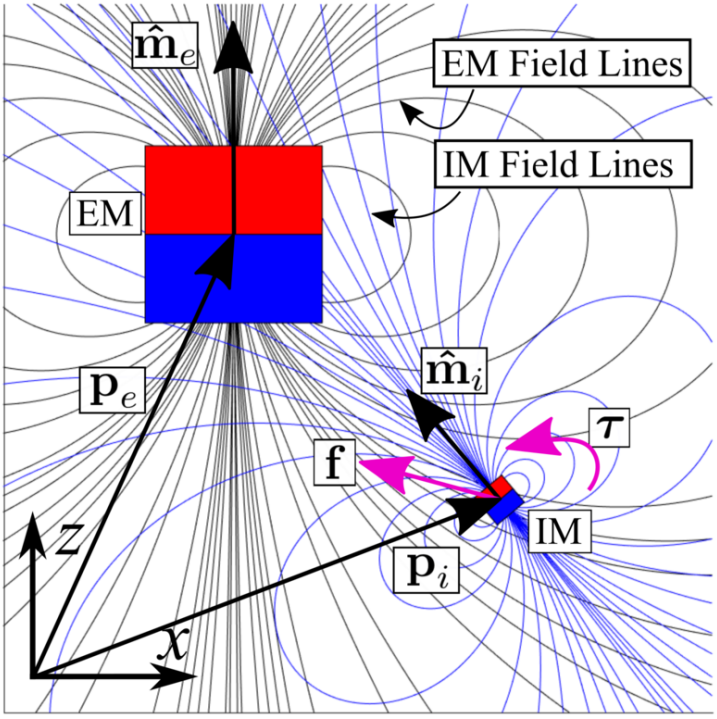

Figure 1.2: Nomenclature of magnets and visual representation of the dipole fields of an IM and EM, without superposition, as well as the force and torque that are imparted on the IM by the EM.

technique.

Systems that use extracorporeal permanent magnets for magnetic dragging and orientating include [48, 49, 50, 51, 44, 2, 3] while similar systems that rely on magnet rotation to achieve rotating fields include [52, 45, 47]. A visualization of the magnetic interaction between an extracorporeal magnet (EM) and and intracorporeal magnet (IM) is shown in Fig. 1.2. The clinical system Stereotaxis relies on external permanent magnets only for orienting devices [9]. While permanent magnets are beneficial owing to their smaller footprint, lack of dependence on a power supply for operation and their relatively low cost when compared to electromagnets, electromagnetic systems offer more field control as their field magnitude can be varied. Magnetic fields have been used for actuation of untethered [33, 44, 52] and tethered devices [53, 54], as well as catheters and continuum robots [46, 9, 55].

The accuracy and precision of navigation using magnetic guidance relies on the estimation of a mapping between applied fields and applied magnetic wrench (force and torque in Fig. 1.2), which

in turn results in a dynamic response. Attempts have been made to operate magnetic devices for colonoscopy without such mapping, or rather an assumption of an ideal mapping (1-to-1) motion where the internal device follows the external actuating magnet perfectly, but this has seldom been successful, especially in environments where disturbances exist. Although diagnostic accuracy using an "open-loop" magnetic colonoscopy system has been shown to be nearly on-par with a traditional FE, the time of procedure drastically increased when using the magnetic system—almost 3-fold [56]. A mapping between input fields and output motion has been studied using both pose estimation of the actuated magnet [44, 47, 1, 2, 3, 53] as well as using Kalman estimation techniques to directly map video feedback from the actuated device to actuating signals [57]. Both of these methods facilitate a closed-loop (CL) control of the IM where losses of magnetic coupling can be mitigated.

This work described in this dissertation is focused on advancing the state-of-the-art in mobile-dipole magnetic actuation. The estimated pose feedback of the actuated device is used to implement and utilize CL magnetic control. This closed-loop effect allows for controlled maneuvers, similar to the use of joint-sensors in rigid-link robots. This functionality open the possibility for the use of autonomy in magnetic endoscopic procedures. Two chapters of this dissertation pertain to the use of autonomy in two clinical applications; specifically, for an endoscopic maneuver and for microultrasound imaging of GI tissue. The advent of robotic surgery and new technologies such as flexible robots and machine learning has spurred considerations into the feasibility of the use of autonomy for medical robotic procedures [58, 59, 60, 61]. The intent of the works in this dissertation is to evaluate the feasibility of autonomous functionalities in the clinical workflow. All methods presented here utilize Level 2, or task, autonomy where an operator makes all clinical decisions and is always "in-the-loop" [59]. This dissertation contains demonstrations of the first works in autonomy for magnetic robotic lower endoscopy.

1.2 Overview of Dissertation and Contributions

This dissertation is motivated by both a clinical shortcoming of existing technology and gaps in literature pertaining to robotic actuation via mobile magnets. Overcoming knowledge gaps in mobile-dipole actuation may enable clinical adoption of the technology to improve endoscopic screening and therapeutics. Existing knowledge gaps include a lack of: (1) CL control of clinically viable magnetic endoscopes, (2) compensation for mechanical effects of tethers in magnetic robots, (3) possibility for endoscopic autonomy for magnetic robots, (4) consideration and analysis of the effects of localization noise on magnetic CL control, (5) possibility for *in situ* diagnostics.

A clinical need exists for an endoscope that: (1) is actuated from the front as to eliminate the need for a semi-rigid body and thus mitigates tissue stress that results from pushing such body and may potentially eliminate the need for patient sedation, (2) has a tip with all functionality of a standard FE, (3) can be steered and oriented precisely, and (4) can be retroflexed anywhere in the lower bowel. To satisfy this need, the magnetic flexible endoscope (MFE) was developed and is displayed in Fig. 1.3. The MFE system, a mobile-dipole system, is introduced here as it is referenced in several chapters of this dissertation, specific technical details are provided later where they are relevant. This system consists of a single extracorporeal permanent magnet (EPM) that applies forces and torques on an intracorporeal permanent magnet (IPM) that is housed in the tip of the MFE. The EM is mounted at a serial manipulator's end-effector. Methods in this dissertation include the kinematic control of both a 6 degree-of-freedom (DoF) (RV6SDL, Mitsubishi Inc., Japan) and 7 DoF (LBR Med, KUKA Deutschland GmbH) serial manipulator, shown in Fig. 1.4. The MFE contains a tether to allow for the passing of standard endoscopic tools. Thhis tether is composed of Pebax (Arkema) and the tip contains a cast urethane sleeve that serves as a mechanical connection between the tether and rigid tip as well as a point of easier bending as the sleeve is flexible enough to fold, which facilitates retroflexion. The device is highly flexible as shown in Fig. 1.5. The majority of validation in this dissertation utilizes the MFE; however, the bulk of the work applies to magnetically actuated endoscopes where the IPM is housed at the tip of the endoscope.

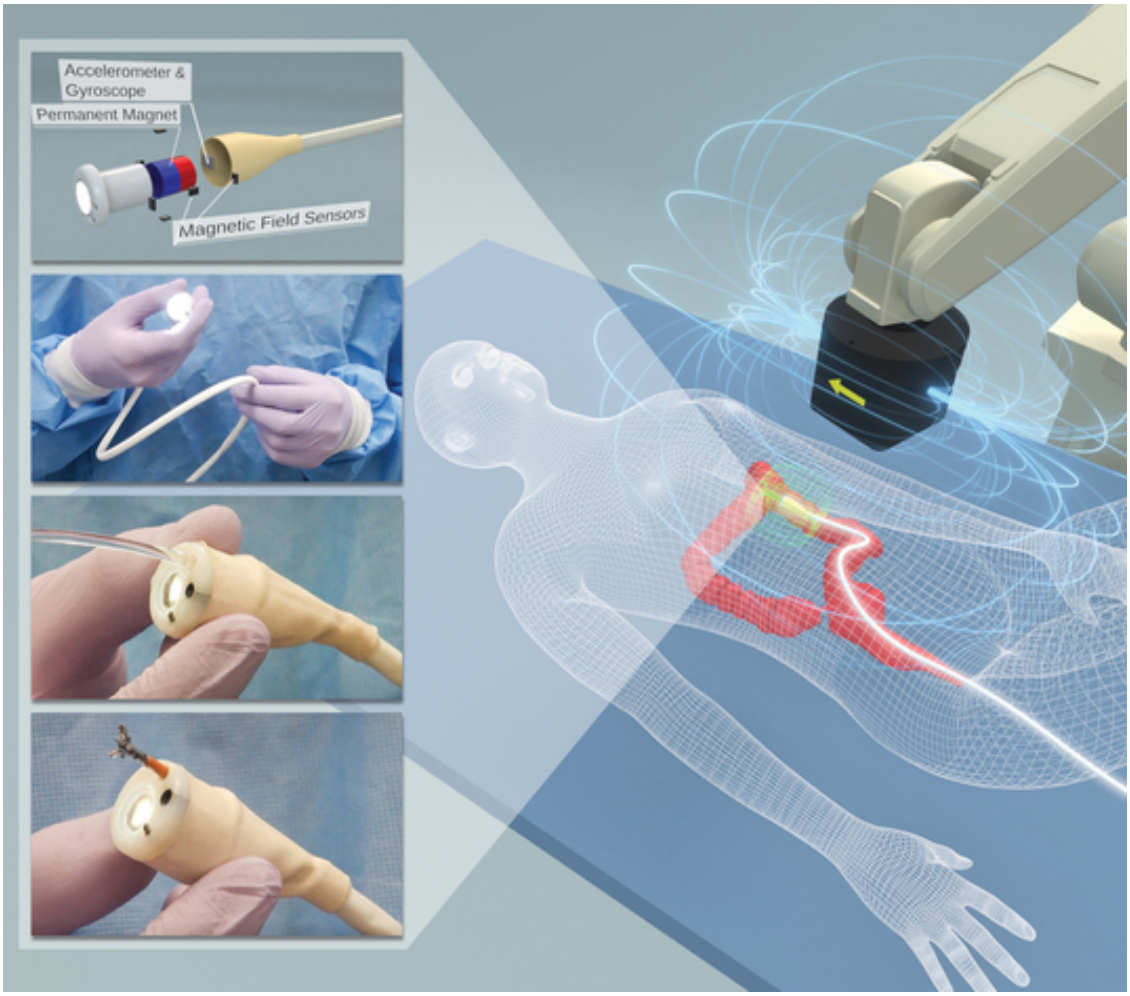

Figure 1.3: Magnetic flexible endoscope system. The animated image is a courtesy of Dr. Addisu Taddese.

This dissertation begins with a summary of magnetic actuation principles as well as magnetic singularities that may arise when using a single-actuating-magnet that moves to translate a single-actuated-magnet in Chapter 2. The use of magnetic CL control is discussed in Chapter 3 where a case study for autonomous control using magnetic CL control is presented. Another clinical application is presented next in Chapter 4 where magnetic control is integrated with microultrasound control to develop a controller for an endoscopic robot to enable robust imaging of the submucosa. These works are the first demonstrations of task autonomy in robotic magnetic lower endoscopy [59]. The final chapters of this dissertation are focused on analyzing magnetic control methodology in terms of force uncertainty and tether mechanics estimation. Chapter 5 is dedicated

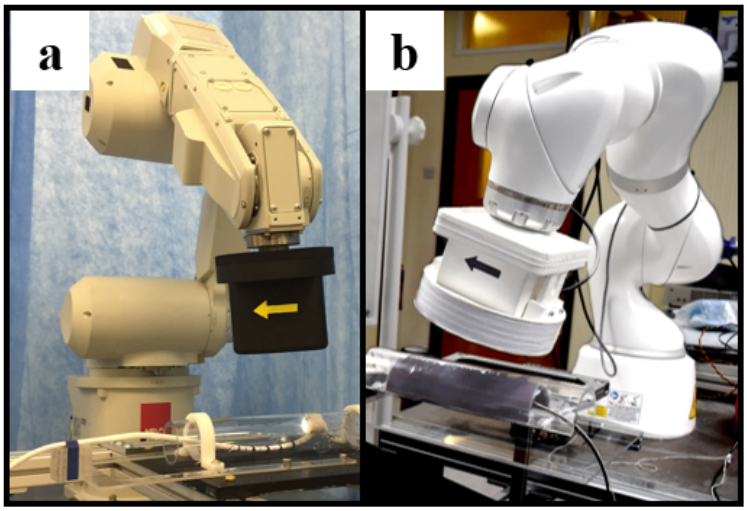

Figure 1.4: (a) Mitsubishi 6 DoF serial arm (RV-6SDL), (b) Kuka Medical 7 DoF serial arm

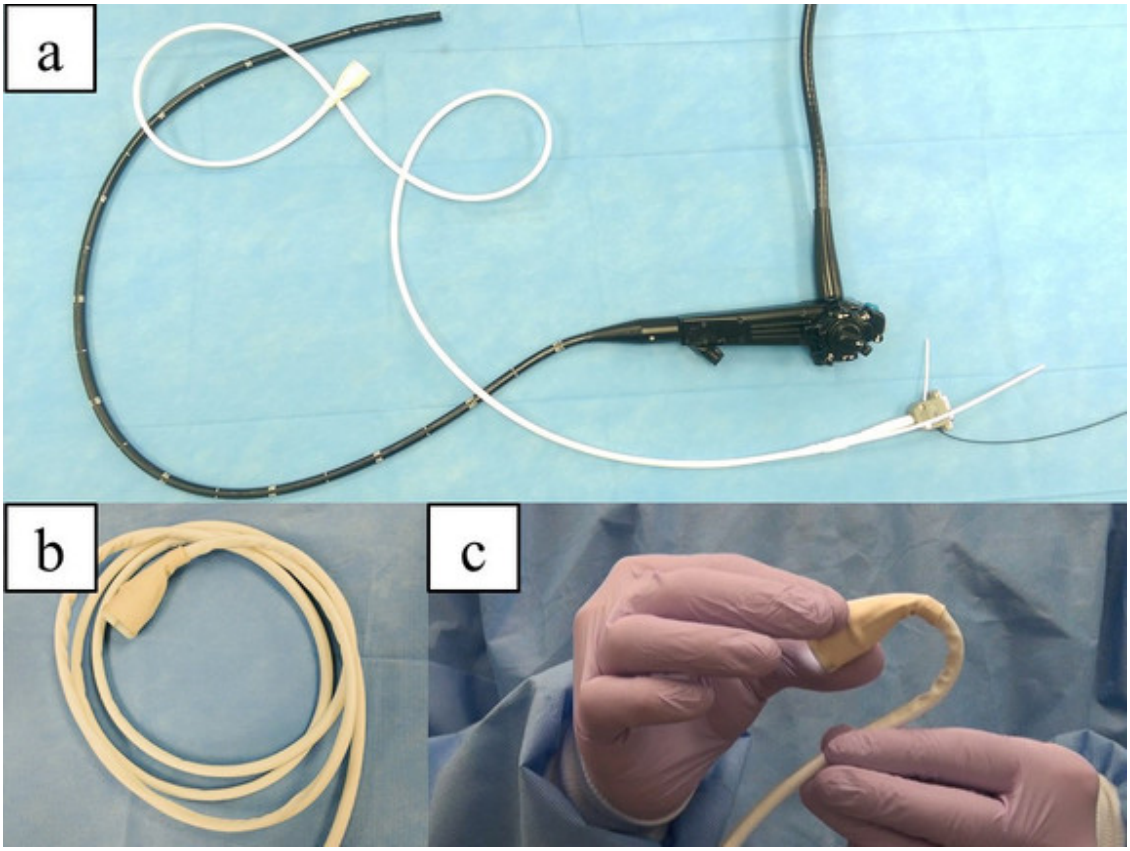

Figure 1.5: The MFE is significantly more flexible than a FE to facilitate safe and painless procedures [5]. (a) The MFE next to a FE (b) the MFE holds a bend configuration (c) demonstration of bending the MFE near its tip.

to discussions of the propagation of force uncertainty in the presence of localization noise. Chapter 6 is dedicated to the investigation, and estimation, of the disturbance wrench that is applied by a tether of a tip-actuated endoscope. The proposed method may enable computed-torque control of an endoscope without the use of sensors for measuring the shape of a tether. The distribution of chapters in this dissertation corresponds to contributions it presents to the field of medical robotics. The contributions of each chapter are below. Please note that contributions of collaborators are stated in the Acknowledgement section of this dissertation.

- Chapter 2: the characterization of magnetic wrench singularities in mobile-dipole actuation in cases of misalignment between the actuating field and the actuated magnet's dipole; previous singularity analysis has applied only to systems where field alignment was assumed, but does not apply to cases where mechanical constraints may exist.

- Chapter 3: (1) co-development of a magnetic CL control system and (2) development and evaluation of an autonomous retroflexion strategy for the MFE.

- Chapter 4: (1) the first demonstration of the servoing of a US probe using US feedback using a robot with no rigid connection to extracorporeal hardware for actuation, i.e. magnetic fields, (2) the first demonstration of robotic μUS-based servoing in the GI tract, and (3) the development and *in vivo* evaluation of the first RCE capable of targeted μUS imaging of the GI tract.

- Chapter 5: proposition of a methodology for analyzing force uncertainty in the presence of localization noise as well as an algorithm that uses a redundancy resolution method for minimizing magnetic force uncertainty.

- Chapter 6: proposition for a novel methodology for estimating the disturbance wrench that a tether imparts on a tip-actuated endoscope to facilitate computed-torque control of a device such as the MFE. This work includes a demonstration of sensorless shape estimation of the distal shape of a tip-actuated endoscope as well as a preliminary demonstration of magnetic control using an estimated parameter.

Chapter 2

Mobile-Dipole Magnetic Actuation

This chapter provides an overview of magnetic modelling and a discussion on singularities in magnetic actuation. Work related to this chapter resulted in the following publications: Refs [5, 13, 14, 6]. Material is reprinted with permission from Ref. [6] (©ASME 2017).

2.1 Principles and Modeling

This dissertation concerns the use of EPMs that are moved through space to drag and orient an actuated permanent magnet. The actuated magnet can be mounted inside a medical device that can then be manipulated using fields generated on the outside of the body. A force and torque must be applied on the actuated device to result in motion. To induce a desired translation and rotation of the internal device, properties of field interactions must be known as to result in a desired force and torque that cause the respective motion. As both the actuating and actuated magnets are permanent, the material medium is assumed to be homogeneous, isotropic, and linear, and magneto-static conditions are assumed [62]. This results in a curl-free and divergence-free field as governed by $\nabla \times \mathbf{h} = 0$ and $\nabla \cdot \mathbf{b} = 0$ of Maxwell's Equations where h indicates magnetic field intensity, $\mathbf{b}$ indicates the magnetic flux density, and ∇ is the gradient operator [62]. Magnetic force and torque can be computed from equations Eq. (2.1) and Eq. (2.2). The force is a function of field gradient, while the torque is a function of misalignment of the actuated magnet's magnetization vector from the actuated field. Here, $\mathbf{b}_e$ is used to indicate the magnetic flux density of the of the EM at the center of mass of the actuated magnet. The magnetization vectors for the IM, $\mathbf{m}_i$, and EM, $\mathbf{m}_e$, are constant as the material is hard-magnetic and defined by the residual magnetization $\mathbf{b}_r$, or remanence, the material's volume V, and the permeability of a vacuum μ_0, shown in Eq. (2.3).

$$\mathbf{f} = (\mathbf{m}_i \cdot \nabla)\mathbf{b}_e \tag{2.1}$$

$$\tau = \mathbf{m_i} \times \mathbf{b}_e \tag{2.2}$$

$$\mathbf{m} = \frac{1}{\mu_0}\mathbf{b}_r V \tag{2.3}$$

To compute magnetic force and torque, an expression for the magnetic field of the EM is needed. Many methods have been applied for modelling permanent magnets that include integration of the Biot-Savart law, use of the Current model, use of the Charge model, series multipole expansions of fields based on scalar potentials, and finite element analysis [62, 63]. The simplest expression is that of a point-dipole, the first term of the multipole expansion, that has a simple analytic form as shown in Eq. (2.4) [64]. The point-dipole model can perfectly model a spherical magnet and its modelling accuracy for other magnet geometries increases with distance. The magnets used in this dissertation are all axially magnetized cylindrical permanent magnets with an equal diameter and length. Based on the size, typical operating distance, and length-to-diameter ratio of the EM used in this dissertation, Petruska and Abbott showed that the dipole model error is approximately 1% [63]. Another convenience of using the point-dipole expression is the ease of analytic differentiation. The force and torque equations can be rewritten using the point-dipole field definition, as shown in Eq. (2.5) and Eq. (2.6). In the case that several magnetic sources are used for generating an actuating field, their field contribution can be linearly summed as magnetic fields are vector fields. This is referred to as the superposition of fields.

$$\mathbf{b}_e(\mathbf{p}) = \frac{\mu_0}{4\pi \left\|\mathbf{p}\right\|^3}(3\hat{\mathbf{p}}\hat{\mathbf{p}}^{\mathrm{T}}\mathbf{m}_e - \mathbf{m}_e) \tag{2.4}$$

$$\mathbf{f} = \frac{3\mu_0 \left\|\mathbf{m}_e\right\| \left\|\mathbf{m}_i\right\|}{4\pi \left\|\mathbf{p}\right\|^4}(\hat{\mathbf{m}}_e\hat{\mathbf{m}}_i^{\mathrm{T}} + \hat{\mathbf{m}}_i\mathbf{m}_e^{\mathrm{T}} + (\hat{\mathbf{m}}_i^{\mathrm{T}}(\mathbf{I} - 5\hat{\mathbf{p}}\hat{\mathbf{p}}^{\mathrm{T}})\hat{\mathbf{m}}_e)\mathbf{I})\hat{\mathbf{p}} \tag{2.5}$$

$$\tau = \frac{\mu_0 \left\|\mathbf{m}_e\right\| \left\|\mathbf{m}_i\right\|}{4\pi \left\|\mathbf{p}\right\|^3}\hat{\mathbf{m}}_i \times (3\hat{\mathbf{p}}\hat{\mathbf{p}}^{\mathrm{T}} - \mathbf{I})\hat{\mathbf{m}}_\mathbf{e} \tag{2.6}$$

Magnetic actuation can be applied by either magnetic pulling via field gradients while controlling heading, or by applying rotating fields to helical designs to generate a threading effect. Both methods have been investigated at the nano, micro, and meso scales. Magnetic pulling, or

dragging, results in direct force-to-motion mapping, while the use of rotating fields relies on the mechanics of threading, thus requiring circumferential contact with the mucosa. As magnetic torque magnitude decays in distance slower than force, rotational methods have a workspace benefit as the spacing between the EM and IM can be greater [65, 66, 67]. Both methods have been shown feasible for CL control in the meso-scale [47, 53]. Motion of the MFE relies on magnetic dragging and orienting. To command a desired motion, a desired wrench must be decided that will result in a dynamic response equal to the desired motion. The input to the dynamic system is a magnetic wrench, while the output is motion of the IM. The precise relationship between wrench and motion is not modelled, but rather, care is taken in choosing a wrench in the direction of desired motion and feedback control is used to compensate for magnitude errors. This method is chosen as the bowel is a tumultuous environment with many constraints. Previous work shows that this assumption is valid [44, 53]. Once a desired change in motion is chosen, a change in magnetic wrench can be applied that will result in that motion.

To compute the inverse problem of finding magnet motions that result in a desired wrench, magnetic wrench equations can be differentiated with respect to magnet motion. The mathematics for the following linearization is detailed in the dissertation of Dr. Addisu Z. Taddese [68]. Certain relations are repeated here for clarity as they are referenced in following chapters. This method is an extension of Mahoney and Abbott's [44] work where they developed an analytic expression of this linearization for force and headings, as shown in Eq. (2.7).

$$\begin{bmatrix} \delta\mathbf{f} \\ \delta\tau \end{bmatrix} = \begin{bmatrix} \frac{\partial \mathbf{f}}{\partial \mathbf{p}} & \frac{\partial \mathbf{f}}{\partial \hat{\mathbf{m}}_e} & \frac{\partial \mathbf{f}}{\partial \hat{\mathbf{m}}_i} \\ \frac{\partial \tau}{\partial \mathbf{p}} & \frac{\partial \tau}{\partial \hat{\mathbf{m}}_e} & \frac{\partial \tau}{\partial \hat{\mathbf{m}}_i} \end{bmatrix} \begin{bmatrix} \delta\mathbf{p} \\ \delta\hat{\mathbf{m}}_e \\ \delta\hat{\mathbf{m}}_i \end{bmatrix} \tag{2.7}$$

This work extends Abbott's to include a consideration for magnetic torque which is relevant in cases where the IM's heading is not aligned with the EM's field. It should be noted that the Jacobian expression can be separated such that one Jacobian, $\mathbf{J}_e$, represents the partial derivative of wrench with respect to EM motions, and another Jacobian, $\mathbf{J}_i$, similarly concerns motions of the IM, as

shown in Eq. (2.8). A dependence between these Jacobians exists as the position vector between the magnets is related by $\mathbf{p} = \mathbf{p}_i - \mathbf{p}_e$. This relation will also cause one of the corresponding Jacobians to have a negative value. It should be noted that such trivial of a relationship does not exist between the magnetic moment vectors, or headings, as any rotation in a magnetization vector about an axis orthogonal to its heading will result in both a rotation and translation of its field at a distance.

$$
\begin{aligned}
\delta\mathbf{w} &= \delta\mathbf{w}_e + \delta\mathbf{w}_i = \frac{\partial w}{\partial \mathbf{x}_e}\delta\mathbf{x}_e + \frac{\partial w}{\partial \mathbf{x}_i}\delta\mathbf{x}_i \\
\begin{bmatrix} \delta\mathbf{f} \\ \delta\tau \end{bmatrix} &= \begin{bmatrix} \frac{\partial \mathbf{f}}{\partial \mathbf{p}_e} & \frac{\partial \mathbf{f}}{\partial \hat{\mathbf{m}}_e} \\ \frac{\partial \tau}{\partial \mathbf{p}_e} & \frac{\partial \tau}{\partial \hat{\mathbf{m}}_e} \end{bmatrix} \begin{bmatrix} \delta\mathbf{p}_e \\ \delta\hat{\mathbf{m}}_e \end{bmatrix} + \begin{bmatrix} \frac{\partial \mathbf{f}}{\partial \mathbf{p}_i} & \frac{\partial \mathbf{f}}{\partial \hat{\mathbf{m}}_i} \\ \frac{\partial \tau}{\partial \mathbf{p}_i} & \frac{\partial \tau}{\partial \hat{\mathbf{m}}_i} \end{bmatrix} \begin{bmatrix} \delta\mathbf{p}_i \\ \delta\hat{\mathbf{m}}_i \end{bmatrix} \\
&= \begin{bmatrix} \mathbf{J}_{e_{fp}} & \mathbf{J}_{e_{fm}} \\ \mathbf{J}_{e_{\tau p}} & \mathbf{J}_{e_{\tau m}} \end{bmatrix} \begin{bmatrix} \delta\mathbf{p}_e \\ \delta\hat{\mathbf{m}}_e \end{bmatrix} + \begin{bmatrix} \mathbf{J}_{i_{fp}} & \mathbf{J}_{i_{fm}} \\ \mathbf{J}_{i_{\tau p}} & \mathbf{J}_{i_{\tau m}} \end{bmatrix} \begin{bmatrix} \delta\mathbf{p}_i \\ \delta\hat{\mathbf{m}}_i \end{bmatrix} \\
&= \mathbf{J}_e \begin{bmatrix} \delta\mathbf{p}_e \\ \delta\hat{\mathbf{m}}_e \end{bmatrix} + \mathbf{J}_i \begin{bmatrix} \delta\mathbf{p}_i \\ \delta\hat{\mathbf{m}}_i \end{bmatrix}
\end{aligned}
\tag{2.8}
$$

which can also be written with respect to the orientation of magnets as follows:

$$
\begin{aligned}
\delta\mathbf{w} &= \begin{bmatrix} \frac{\partial \mathbf{f}}{\partial \mathbf{p}_e} & \frac{\partial \mathbf{f}}{\partial \hat{\mathbf{m}}_e} \\ \frac{\partial \tau}{\partial \mathbf{p}_e} & \frac{\partial \tau}{\partial \hat{\mathbf{m}}_e} \end{bmatrix} \begin{bmatrix} \mathbf{I} & \mathbf{0} \\ \mathbf{0} & \mathbf{S}(\hat{\mathbf{m}}_e)^{\mathrm{T}} \end{bmatrix} \begin{bmatrix} \delta\mathbf{p}_e \\ \omega_e \end{bmatrix} + \begin{bmatrix} \frac{\partial \mathbf{f}}{\partial \mathbf{p}_i} & \frac{\partial \mathbf{f}}{\partial \hat{\mathbf{m}}_i} \\ \frac{\partial \tau}{\partial \mathbf{p}_i} & \frac{\partial \tau}{\partial \hat{\mathbf{m}}_i} \end{bmatrix} \begin{bmatrix} \mathbf{I} & \mathbf{0} \\ \mathbf{0} & \mathbf{S}(\hat{\mathbf{m}}_i)^{\mathrm{T}} \end{bmatrix} \begin{bmatrix} \delta\mathbf{p}_i \\ \omega_i \end{bmatrix} \\
&= \tilde{\mathbf{J}}_e \begin{bmatrix} \delta\mathbf{p}_e \\ \omega_e \end{bmatrix} + \tilde{\mathbf{J}}_i \begin{bmatrix} \delta\mathbf{p}_i \\ \omega_i \end{bmatrix}
\end{aligned}
\tag{2.9}
$$

where $S(\mathbf{a}) \in \mathfrak{so}(3)$ denotes the skew-symmetric form of the cross-product operation.

The terms $\delta\mathbf{w}_e$ and $\delta\mathbf{w}_i$ in Eq. (2.8) can be interpreted as the changes in wrench that result from respective changes in EM and IM pose. As the IM moves relatively slow in magnetic endoscopy, the $\delta\mathbf{w}_i$ term can typically be ignored. To compute the desired pose, the actuation Jacobian, $\mathbf{J}_e$, must be inverted. It should be noted that $\mathbf{J}_e$ is of rank 5 owing to the inherent system singularity of inability to apply a torque by rotating the EM about its own axis. This is a result of the dipole

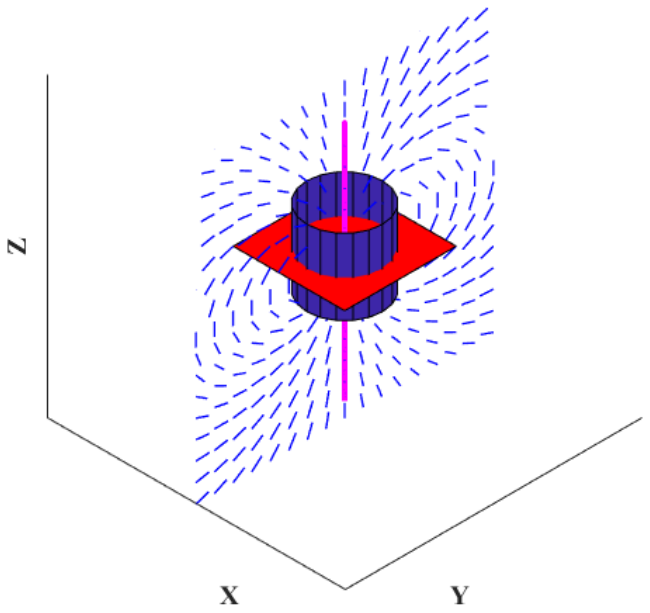

Figure 2.1: The red plane represents the singularity plane, the blue cylinder represents the outer shape of a cylindrical permanent magnet. The pink line represents the axis of singularity, while the blue lines are the magnetic field.

field's symmetry about its magnetization axis, as shown in Fig. 2.1. This degree of redundancy can be utilized for secondary tasks such as reconfiguration of the serial manipulator to which the EM is attached. This results in a wrench-wise internal motion, while the motion of the serial manipulator is not truly internal as its end-effector moves. As $\mathbf{J}_e$ is not full rank, an inversion technique that minimizes the norm of pose changes can be used. A weighted right pseudo-inverse with damping, α, is shown in Eq. (2.10). Without the numerical singularity compensation, i.e. damping, this expression locally minimizes the least-squares constrained objective function shown in Eq. (2.11). Here, $\delta\mathbf{x}_e$ is a stacked vector that includes $\delta\mathbf{p}_e$ and $\hat{\mathbf{m}}_e$. The matrix $\mathbf{W}$ in these expressions is a diagonal weight matrix whose terms can be used to adjust preference for component to minimize. This is relevant in this magnetic actuation control as $\delta\mathbf{x}_e$ contains units of length and heading.

$$\begin{bmatrix} \delta \mathbf{p}_e \\ \delta \hat{\mathbf{m}}_e \end{bmatrix} = \mathbf{W}^{-1}\mathbf{J}_e^{\mathrm{T}}(\mathbf{J}_e\mathbf{W}^{-1}\mathbf{J}_e^{\mathrm{T}} + \alpha\mathbf{I})^{-1} \begin{bmatrix} \delta \mathbf{f}_{desired} \\ \delta \tau_{desired} \end{bmatrix} = \mathbf{J}_e^{\#}\delta \mathbf{w}_{desired} \tag{2.10}$$

$$\begin{aligned} \underset{\delta \mathbf{x}_e}{\text{minimize}} \quad & \left\| \delta \mathbf{x}_e^{\mathrm{T}} \mathbf{W} \delta \mathbf{x}_e \right\| \\ \text{subject to} \quad & \mathbf{J}_F \delta \mathbf{x}_e = \delta \mathbf{w}_{desired} \end{aligned} \tag{2.11}$$

The relation in Eq. (2.10) results in 5 DoFs of control. As Earnshaw's theorem states that stability cannot be achieved solely with magnetic fields, the IM's position cannot be controlled in the attractive direction, thus the system at hand inherently has 4 DoF. The presence of a damping medium and counter-force can be used to stabilize motion as was done in Mahoney and Abbot's work to achieve the third translation DoF [44].

The 4 DoF control of the IM is applicable instantaneously; however, full wrench control is limited by a bound on EM velocity. As wrench control in mobile-dipole actuation relies on magnet pose control, the application of an arbitrary force and torque requires the motion of the EM. If the EM could be translated and rotating without velocity bounds, any desired magnetic wrench could be applied instantaneously (assuming the IM does not change configuration in this time). In practice, the velocity of the EM is bounded, and preferably slow owing to the proximity to the patient. The result is a limitation on the instantaneous magnetic wrench that can be applied on the IM. The magnetic forces and torques applied on the IM must be continuous, which prevents the application of any wrench on the IM. This may result in instances of the EM being positioned a large distance away from a configuration where a desired wrench may be applied on the IM, resulting in a period of necessary EM translation and rotation. During this intermediate EM motion, the IM continuously shifts in response to the changing wrench. This interplay of EM and IM motion may pose control difficulties that may be addressed via path-planning methods. This effect will be hereafter referred to as the *EM velocity-wrench bound*.

Analyzing the Jacobian $\mathbf{J}_e$ can provide insight into the implications of instantaneous motion. Although analysis of differential mapping is common for motion analysis of rigid-link robots via manipulability or sensitivity ellipsoids [69, 70], it has been seldom investigated in magnetic robots.

Although this will be the topic of Chapter 5, the concept is introduced here as most chapters involve some interpretation of "better" ways to move the EM. Knowing that the field relationships can be analyzed similar to those of twists and joint speeds of rigid-link robots, the reader may benefit from a more intuitive interpretation. Sub-Jacobians, such as $\mathbf{J}_{e_{fp}} \in \mathbf{R}^3$ which is a linear mapping between change in EM position and change in magnetic force, are first analyzed. The singular value decomposition, SVD, of this Jacobian is $\mathbf{U}\mathbf{\Sigma}\mathbf{V}^{\mathrm{T}}$ where $\mathbf{U}$ and $\mathbf{V}$ are two orthonormal spaces where the columns of $\mathbf{U}$ are called left-singular vectors and the columns of $\mathbf{V}$ are called right-singular vectors. The diagonal of $\mathbf{\Sigma}$ contains the singular values, s_i, of the Jacobian which are arranged such that $s_1 > s_2 > s_3$. A singular value of zero indicates a loss of rank, and thus gain of degree of nullity.

In terms of magnetic actuation, the left-singular vectors indicate the directions of applied wrench that correspond to singular values i.e. $\hat{\mathbf{u}}_1$ is the direction in which s_1 is relevant. Likewise, the right-singular vectors indicate the respective direction of applied twist. An example of a differential mapping using $\mathbf{J}_e$ is shown in Fig. 2.2. Here, the IM and EM are in a fixed configuration and the mapping visualized is $\mathbf{J}_{e_{\tau p}}$. The magnetic moments, or headings, of the magnets are represented with black lines. An assumption is now made that the EM is translated in a sphere of all possible directions, each of the same magnitude. This set of motions will produce a set of changes in torque imparted on the IM, which is shown in green in Fig. 2.2. The input motions are shown in magenta. Although these input motions are made up of vectors in a uniformly distributed set of directions as to make a sphere given a translation, the magnitudes here are scaled in proportion to the resultant torque magnitude effect. In other words, the longer a magenta vector is, the more impact a motion in that direction had on changing torque magnitude. The directions of EM motion that are most meaningful can thus be visualized. In Chapter 3 this concept is used to an advantage to impart a high-magnitude torque on the IM to retroflex the MFE; or in other words, command the MFE's tip to invert as to obtain a retrograde view of the lumen.

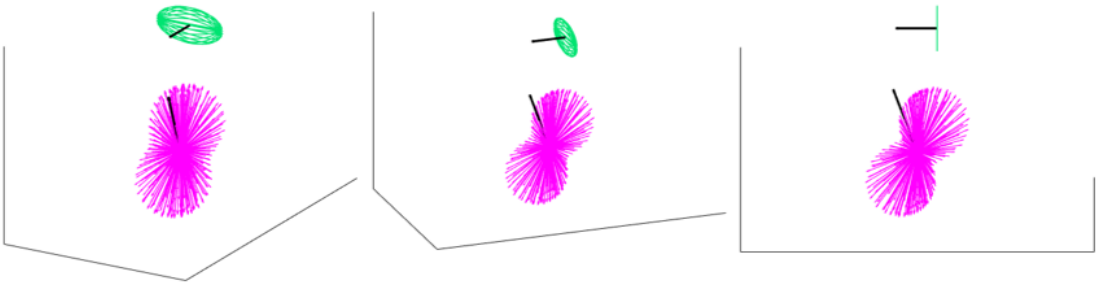

Figure 2.2: Three views of the actuation space of an EM when actuating an IM. The poses of the IM and EM are identical in all views, only perspective changes to convey 3D information. The magenta shape represents translation of the EM, while the green shape represents torque imparted on the IM. The black lines are respective magnetic moment vectors i.e. headings of the dipoles.

2.2 Mobile-Dipole Singularities

Typically, magnetic devices can be controlled in either 4 (as is the case for the MFE) or 5 DoFs: 2 or 3 positional DoFs and 2 orientation DoFs. Recently, Diller et al. developed a method for 6 DoF magnetic actuation although this involves complexity in non-uniform field distribution [71]. The following text includes a consideration that has been taken to address the inherent torque singularity (Section 2.2.1) and a discussion of magnetic kinematic singularities (Section 2.2.2).

2.2.1 Compensation for Field-Symmetry Singularity

The position of the IM inside a device impacts the behavior of this device. In the case of the MFE, the IM is offset from the central axis of the device for purposes of compactness. If the magnet would be in the center of a cylindrical shape, there would be no preferential roll of the device. However, as the dipole is offset from the center, an additional axial torque exists that results from the relation $\tau_a = \mathbf{R}_t^w \mathbf{r}_o \times \mathbf{f}$ where $\mathbf{r}_o$ indicates the dipole offset from center of cylinder, $\mathbf{R}$ is a rotation matrix that maps coordinates from the MFE's local tip frame to the world frame, and

f is the magnetic force. To determine if this axial torque could be modeled via the dipole model and the geometric relation, set of experiments was conducted. The experimental setup is shown in Fig. 2.3 where Fig. 2.3(a) shows the position displacement of the IM as well as a schematic the resultant roll wrench and Fig. 2.3(b) shows the experimental setup that was used to characterize the roll wrench. The EM was programmed to move through a 3 by 3 grid of points. The EM stopped at each point while force data was recorded using a force and torque sensor (Nano 17 SI-25-0.25, ATI Technologies). The experiments were repeated with the capsule rolled at 30° increments. The theoretical and experimental results of this experiment are shown in Fig. 2.4 [6]. The theoretical result was obtained using the point dipole model. The higher torque values shown in the top plot in Fig. 2.4 occur when the EM is directly on the side of the IM i.e. indexes 4, 5, and 6. The torque in other configurations is significantly lower.

The experimental results, shown in the bottom plot of Fig. 2.4, support the theoretical result at indexes 4, 5, and 6; however, deviation occurs at other configurations. This is likely due to the sensitivity of the result to ideal positioning of the IM i.e. an error in IM position may have a significant impact on the result. Furthermore, during a set of 5 trials where the MFE was commanded to follow a straight-line trajectory autonomously, the offset vector $\mathbf{r}_o$ was always within 45° of the vertical, suggesting that this axial torque is sufficient to bias the MFE's roll orientation. This was observed when the magnitude of $\mathbf{r}_o$ was 1.85 mm, which is less than 10% of the devices diameter. While a pure axial torque exists in the MFE as it is cylindrical, other non-symmetric shapes would cause different behaviour. This topic is addressed again in Chapter 4 of this dissertation where sensors are placed on one side of a robotic capsule endoscope and this axial torque is used to encourage sensor-tissue contact.

As a torque can be applied only in 2 DoF, and thus on a plane, it may be of interest to change the orientation of this plane respective to the geometry of the device's tip. In the case that a magnet's moment vector is oriented at, for example, a 45° with respect to the device's central axis, the torque singularity is shifted off of the roll direction. Rotation about axes closer to the central axis of the controlled device become feasible. To avoid the device rotating without control about the new axis

of singularity, a mechanical constraint, e.g. tether pull, can be applied. This method has been observed for controlling the roll of a device; however, it is only applicable in a small roll range. Alternative solutions, such as the implementation of 6 DoF control [71], are more robust.

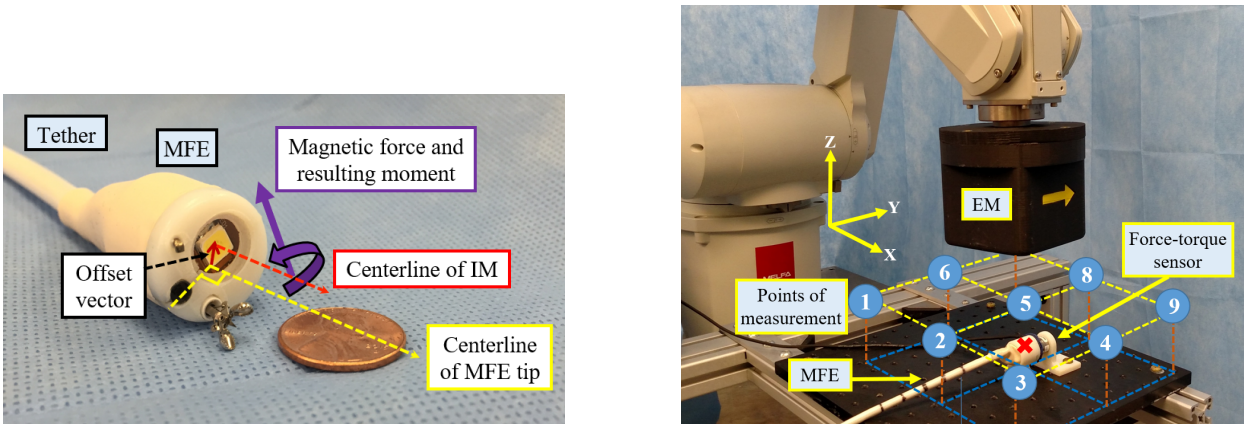

(a) MFE tip schematic

(b) Experimental setup

Figure 2.3: Experimental setup for characterizing roll torque that exists owing to misalignment of the IM with the center-line of the cylindrical MFE tip (a). The actuating permanent magnet, or EM, gathered data at each of the blue locations shown in (b). (©2017 ASME [6])

2.2.2 Mobile-Dipole Kinematic Singularities

The magnetic singularity that arises owing to field symmetry about the magnetization axis is well known. The following section is an investigation into additional singularities that arise from a drop in the rank, Eq. (2.12), of the magnetic Jacobian in systems where a single EPM actuates an IPM.

$$rank(\mathbf{J}_e) < max(rank(\mathbf{J}_e)) \tag{2.12}$$

Prior work has shown that no singularities exist apart from singularities of the manipulator on which the EM is mounted; however, the authors made an assumption that the IM aligned with the external field owing to the IM being suspended in liquid [44]. In the case that the IM is not tetherless and suspended in an environment with little disturbance, this assumption may not hold. Singularities in actuation via a single stationary electromagnet were discussed in Ref. [64] where the authors defined a force singularity that exists when the tool's, or IM's, dipole moment

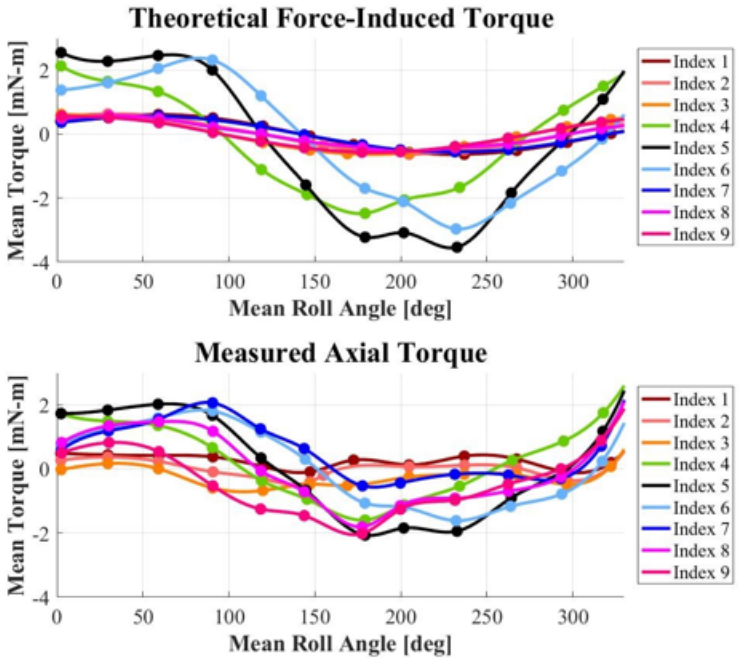

Figure 2.4: The force-induced torque was recorded at all indexes (EM configurations). The theoretical estimate was calculated using the point dipole model (top). The measured values most closely support the theoretical estimate at indexes 4, 5, and 6 (bottom). (©2017 ASME [6])

is orthogonal to the position vector between the EM and IM, and force can only be applied on the plane spanned by the tool's dipole moment and the position vector. However, when using a mobile EM, this singularity condition does not apply as the EM can be translated to apply force in any direction, apart from specialized cases that will be further discussed and do not necessarily satisfy the aforementioned position vector constraint. Similar analyses have been done on systems with several electromagnets: Petruska and Nelson demonstrated that eight static electromagnets are necessary for 5 DoF control of a magnetic device without orientation-dependent singularities that have been encountered by groups in the past [72]. The aim of this section is to characterize any singularities that may exist by studying the Jacobian mapping between EM motion and the wrench imparted on the IM. This characterization is relevant to the design of magnetic actuation systems, especially when the IM may be subject to mechanical constraints.

The characterization here will concern the Jacobian $\tilde{\mathbf{J}}_e$ and its component Jacobians, i.e. $\tilde{\mathbf{J}}_{e_{fp}}$ as defined in Eqs. (2.8) and (2.9). To study the impact of the Jacobian irrespective of the exist-

ing magnetic force or torque or distance between magnets, each Jacobian is normalized as done in [44]; this can be seen below in Eq. (2.13). A scalar singularity compensation value α_s is used to compensate for cases of the force or torque magnitude being null. It should be noted that these multiplication operations do not affect the rank of the matrix. Additionally, pre-multiplying a diagonal scales the row of the Jacobian by respective diagonal elements, while post-multiplying scales the columns.

$$\begin{aligned}\begin{bmatrix}\delta\mathbf{f}\\ \delta\tau\end{bmatrix} &= \begin{bmatrix}\frac{1}{\|\mathbf{f}\|+\alpha_s}\mathbf{I} & \mathbf{0}\\ \mathbf{0} & \frac{1}{\|\tau\|+\alpha_s}\mathbf{I}\end{bmatrix}\tilde{\mathbf{J}}_e\begin{bmatrix}\delta\mathbf{p}_e\\ \omega_e\end{bmatrix}\\ &= \bar{\mathbf{J}}_e\begin{bmatrix}\delta\mathbf{p}_e\\ \omega_e\end{bmatrix}\end{aligned} \tag{2.13}$$

To determine singular configurations, "particular" configurations are selected that are reasonably expected to represent all possible configurations; these are shown in Fig. 2.5. An analysis was conducted of all Jacobians of $\bar{\mathbf{J}}_e$ with results shown in Table. 2.1. The results of the analysis is listed by pose number and correspond to the poses shown in Fig. 2.5. A typical result is listed at the top of the table and is computed at a configuration of magnets where the magnetic moment vectors are not aligned or orthogonal, and the position vector is not aligned with a singularity axis or orthogonal to moment vectors. Results that are out-of-ordinary are in bold and shown in red. It should be noted that not all poses shown in Fig. 2.5 are unique, and thus redundant information may be present in Table. 2.1.

A force Jacobian singularity occurs in pose 9, which is identical to poses 12 and 15. A force of zero is observed in pose 13. Null torques can be observed when the magnetic moment vectors of the IM and EM are aligned. The ranks of the sub-Jacobian, e.g. $\bar{\mathbf{J}}_{e_{fp}} \in \mathbf{R}^3$, are shows as cases may exist where an actuating EM may not have all DoFs owing to system design or a singularity in the actuating manipulator. Although a singularity is defined by loss of DoF, or reduction in Jacobian rank, poorly conditioned Jacobians are of just as much interest. Rigid-link manipulators suffer concrete losses of DoF in the vicinity of singular configurations in the sense that, although

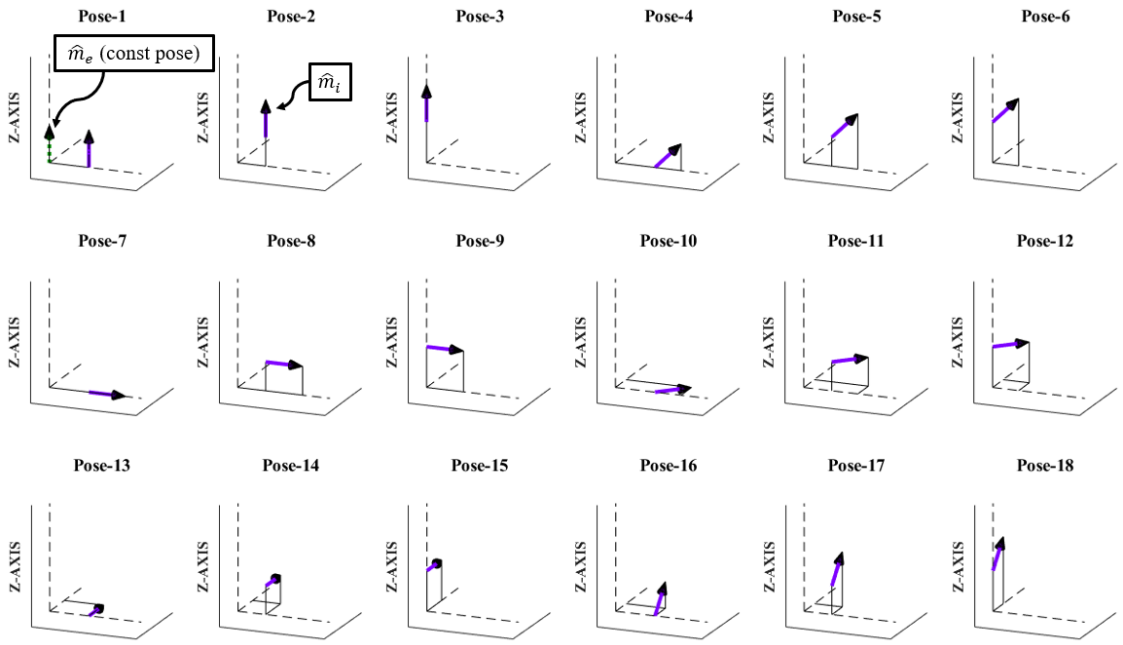

Figure 2.5: Relative poses of interest of the IM and EM where "pose" is defined by relative position and heading. Although not every configuration shown is singular, visualization of all poses is helpful in understanding the cause of singularities. Here, $\hat{\mathbf{m}}_i$ shows in various configurations while $\hat{\mathbf{m}}_e$ is shown only once, for clarity, at the origin.

manipulability may be low, motion in an ill-conditioned direction still occurs. Alternatively, in magnetic actuation, owing to the "link" being magnetic rather than rigid, an inability to apply sufficient wrench, albeit some may be applied, may not result in device motion owing either to static friction, inertial effects, an environmental constraint, or device mechanics e.g. stiffness of magnetically steered needle. Thus, the region around singularities are just as important as strict singularities in magnetic actuation.

Table 2.1: Ranks of mobile-dipole Jacobians in various poses as shown in Fig. 2.5. Here, "rk" denotes "rank" and "nz" denotes "non-zero".

Pose no.	$rk(\bar{\mathbf{J}}_f)$	$rk(\bar{\mathbf{J}}_t)$	$rk(\frac{\partial \mathbf{f}}{\partial \mathbf{p}_e})$	$rk(\frac{\partial \mathbf{f}}{\omega_e})$	$rk(\frac{\partial \tau}{\partial \mathbf{p}_e})$	$rk(\frac{\partial \tau}{\omega_e})$	$\|\mathbf{f}\|$	$\|\tau\|$
Typical	3	2	3	2	2	2	nz	nz
1	3	2	3	**1**	**1**	2	nz	**0**
2	3	2	3	2	2	2	nz	nz
3	3	2	3	2	2	2	nz	**0**
4	3	2	3	2	**1**	2	nz	nz
5	3	2	3	2	2	2	nz	nz
6	3	2	3	2	2	2	nz	nz
7	3	2	**2**	2	**1**	**1**	nz	nz
8	3	2	3	2	2	2	nz	nz
9	**2**	2	**2**	**1**	2	**1**	nz	nz
10	3	2	**2**	2	2	**1**	nz	nz
11	3	2	3	2	2	2	nz	nz
12	**2**	2	**2**	**1**	2	**1**	nz	nz
13	3	2	**2**	2	2	**1**	**0**	nz
14	3	2	**2**	2	2	**1**	nz	nz
15	**2**	2	**2**	**1**	2	**1**	nz	nz
16	3	2	3	2	2	2	nz	nz
17	3	2	3	2	2	2	nz	nz
18	3	2	3	2	2	2	nz	nz

Chapter 3

Control of Magnetic Devices

This chapter contains an overview of magnetic CL control that was co-developed under leadership of Dr. Addisu Z. Taddese [68] and used in the following work in this dissertation. This overview is followed by a case-study of magnetic CL control that is extended to procedural autonomy. This section begins with a detailed outline of the platform originally introduced in Chapter 1.2. Work related to this chapter resulted in the following publications: Refs [1, 2, 53, 3, 73].

3.1 Magnetic Flexible Endoscope

The MFE platform is used in experiments throughout this chapter. Although the earlier control works used a previous version of the magnetic device, magnetic properties are identical and mechanics are not included in control, so all results apply equivalently. The system, shown during an animal trial in Fig. 3.1, consists of an IM mounted inside the MFE, along with an EM mounted at the end-effector of an industrial serial manipulator (RV6SDL, Mitsubishi, Inc., Japan). The IM is a Neodymium Iron Boron (NdFeB) N52 grade permanent magnet with a diameter and length of 11.11 mm (D77-N52, K&J Magnetics, USA). Similarly, the EM is an NdFeB N52 grade permanent magnet with a diameter and length of 101.6 mm (ND_N-10195, Magnetworld AG, Germany). Both magnets have a residual magnetization of approximately 1.48 T. System control is implemented using Robotic Operating System (ROS) middleware [74]. The majority of software is written in Python owing primarily to the ease of use of the NumPy library for linear algebra. Simulations for all experiments were conducted using Gazebo [75], an environment that is compatible with ROS and contains a physics engine. Dr. Addisu Z. Taddese developed a magnetic interaction plugin for Gazebo that was used throughout this work.

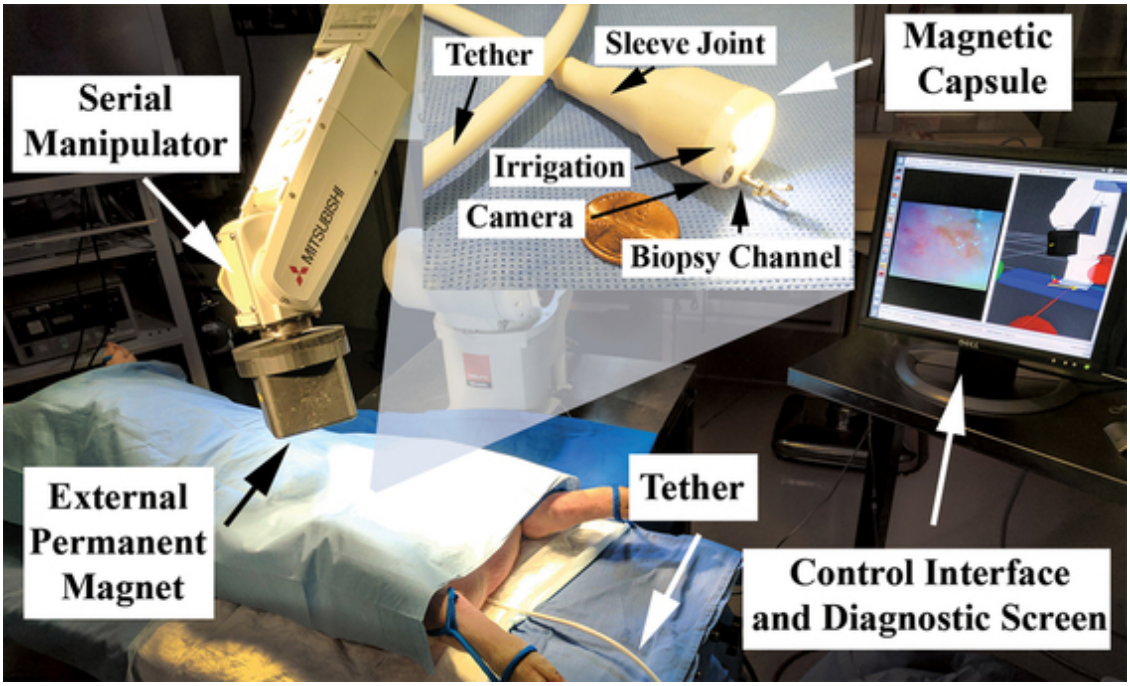

Figure 3.1: The MFE system has all functionality of a traditional FE. Here, the system is shown during an animal trial [5].

3.2 Trajectory-Based Control

Magnetic CL control serves the purposes of (1) reducing tracking error and (2) reducing cognitive burden from an operator. The long-term goal of the project is to allow an operator to specify motions via joystick and for the system to move the MFE towards the desired goal. On the contrary, when using open-loop (OL) control, an operator would watch the output screen of the MFE, navigate the EM, and hope that the MFE followed owing to strong magnetic coupling. If coupling is lost, the operator would have to return the EM to the original pose and try again. Closed loop control was implemented in this work for tracking trajectories with both commanded positions and velocities.

Closed loop magnetic control is implemented here using formulations similar to Eqs. (2.8) and (2.11) where the desired infinitesimal change in wrench is chosen as to result in some desired motion. In a work that focused on position control, a proportional-integral-derivative (referred to hereafter via function $pid()$) controller that acted on error in position and orientation was used,

shown in Eq. (3.1) where $\mathbf{e}_p = \mathbf{p}_{i_{desired}} - \mathbf{p}_i$ indicates position error and $\mathbf{e}_o = \hat{\mathbf{m}}_i \times \hat{\mathbf{h}}_{desired}$ where $\hat{\mathbf{h}}_{desired}$ is the desired IM heading. Here, a trajectory was defined by a set of points on both a line and a sine curve while the heading of the IM was commanded to be tangent to the curve.

In a work that focused on velocity control, a similar method was applied with the controller acting on errors in velocity and orientation, shown in Eq. (3.2). Here, a trajectory was generated using a cubic spline that was defined by a set of points. While a velocity controller was used for forward motion control, a position controller was implemented to keep the IM on its path. Here, $\hat{\mathbf{t}}$ indicates the tangent direction to the path, $\hat{\mathbf{n}}$ indicates the normal direction to the path, and $\mathbf{e}_v = \dot{\mathbf{p}}_{i_{desired}} - \dot{\mathbf{p}}_i$ is error in velocity. This strategy was motivated by quad-copter trajectory execution techniques. In the velocity controller, The applied magnetic force was removed from the control terms in order to reduce the amount of inherent integration in the system as the controller output is change-in-force, rather than force itself.

$$\begin{bmatrix} \delta\mathbf{f}_{desired} \\ \delta\tau_{desired} \end{bmatrix} = \begin{bmatrix} pid(\mathbf{e}_p) \\ pid(\mathbf{e}_o) \end{bmatrix} \tag{3.1}$$

$$\begin{bmatrix} \delta\mathbf{f}_{desired} \\ \delta\tau_{desired} \end{bmatrix} = \begin{bmatrix} pid(\mathbf{e}_v)\hat{\mathbf{t}} + pid(\mathbf{e}_p)\hat{\mathbf{n}} - \mathbf{f} \\ pid(\mathbf{e}_o) \end{bmatrix} \tag{3.2}$$

Here, $\mathbf{f}$ indicates the current applied magnetic force. A similar controller to Eq. (3.2) was used in a disturbance rejection trial where the MFE's body was physically perturbed and the MFE returned to its original trajectory in Ref. [53, 68]. These control works were successful during bench-top trajectory following trials and, in general, served as a confirmation that the presented methods are feasible for magnetic CL control.

3.3 Towards Autonomy in Robotic Endoscopy: Retroflexion

This section concerns the application of magnetic CL control to complete an autonomous maneuver. One maneuver that is expected to be difficult for an operator to complete manually is the

retroflexion of the MFE, or turning the tip of the device 180° such that it can visualize and perform therapy on the back of colonic folds. Typically, retroflexion using an FE is practiced only in the wider proximal and distal ends of the large intestine owing to the stiff nature of the colonoscope. There, the FE uses wall to bank the body to obtain retrograde visualization. This inability to examine the proximal side of the majority of colon folds contributes to today's suboptimal colorectal cancer detection rates. The use of the more flexible MFE facilitates the ability to retroflex anywhere with relative ease; however, is technically challenging as magnetic torque must be applied in a proper manner. The algorithm presented results in the EM undergoing motions that both apply as large of a wrench as possible on the IM, while also reducing the heading error from the desired (retroflexed). The following section details a real-time magnetic wrench optimization algorithm for the retroflexion of the MFE. The methods and results in this section were published in Refs. [3] (*Slawinski, Piotr R and Taddese, Addisu Z and Musto, Kyle B and Obstein, Keith L and Valdastri, Pietro, Autonomous Retroflexion of a Magnetic Flexible Endoscope, IEEE Robotics and Automation Letters, 07/2017*) and [73].

3.3.1 Motivation for Autonomous Retroflexion

Adenoma, or benign tumor, detection rate (ADR) during colonoscopy has been shown to be a predictor of the risk of cancer developed between routine screenings [76]. Although ADRs are over 25% for men and 15% for women, most experts agree that these can be improved. A 1% increase in ADR has also been shown to coincide with a 3% decrease in the risk of cancer [77]. Although the use of the flexible endoscope has been the standard diagnostic tool for over 50 years, adenoma miss rates of 15 to 41% have been reported [78, 77]. These low performance rates are hypothesized to result from polyp positioning on the proximal side of folds and flexures [78]. Retroflexion is a maneuver where the endoscope is rotated backwards inside a lumen for an improved endoscopic view behind folds and, owing to the stiff nature of the traditional endoscope, is typically only practiced in the proximal and distal ends of the colon where the lumen diameter is largest. The maneuver is recommended by the American Society of Gastrointestinal Endoscopy and labeled as

an "essential" element of colonoscopy [79]. Additionally, past studies have shown that retroflexion cannot be replaced by extensive endoscopy manipulation since it is inadequate for viewing behind folds [80].

Retroflexion using a tethered magnetically actuated capsule was demonstrated in previous work using OL teleoperation [81]; however, the lack of position and orientation feedback of the device resulted in a steep learning curve and long procedure duration. Developing an autonomous retroflexion maneuver is crucial to the procedure to reduce adenoma miss rate. To facilitate the ability of the endoscope to respond to environmental disturbances, i.e. contact with tissue or motion of the patient, decisions on the motion of the tip of the endoscope should be made algorithmically in real-time, eliminating any teleoperative input from the user for the specific task of retroflexion. Additionally, an autonomous system reduces the level of experience required to perform the maneuver, thus maintaining the focus on diagnostics during retroflexion training rather than endoscope maneuverability. Crucial to this aim are real-time localization and CL control of the tip of the endoscope, both demonstrated previously by STORM lab [82, 1, 83, 2] and others [84, 85, 44].

In the sections that follow, an algorithm is presented for autonomous retroflexion of the MFE with validation conducted on experimental setups of increasing complexity. Using real-time magnetic localization [82], the tip of the endoscope, starting from a straight alignment with the lower-bowel lumen, is retroflexed by a magnetic wrench applied from an EM that is attached to a 6 DoF industrial manipulator as seen in Fig. 3.2. The algorithm, running at a rate of 65 Hz (real-time), optimizes the magnetic wrench that is applied on the device's tip so as to drive the endoscope toward a target pose, as a function of end-effector motion. The contribution of this work is the optimization of the end-effector motion in task space making it more suitable for applications where task-space constraints (e.g. avoiding collision with the patient's body) exist. Further, in prior STORM lab work [1, 2], the error term for the CL orientation controller was defined by the cross product of the current and desired heading vectors. While this error term describes the shortest angular path between the heading vectors, it is not necessarily the most efficient for magnetic manipulation. This work shows that a more efficient error term can be found, especially in the context of retroflexion.

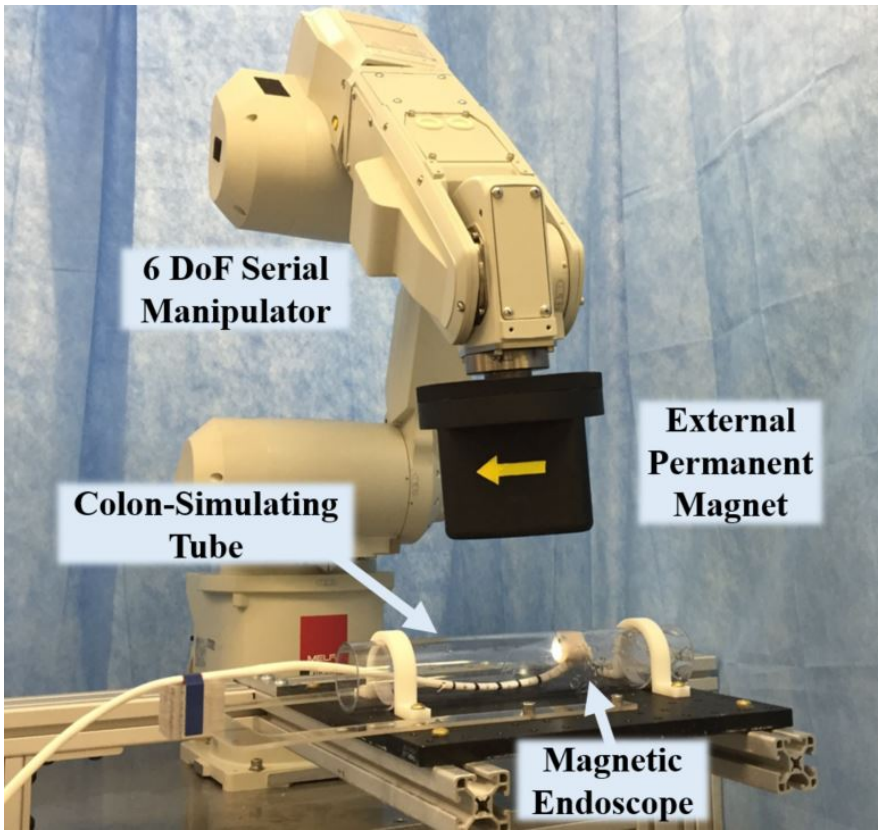

Figure 3.2: Platform used to develop and evaluate the autonomous retroflexion algorithm. Here, the MFE (magnetic endoscope) is in a retroflexed configuration inside a clear acrylic tube. External to the tube is a serial manipulator with an EM mounted at its end-effector. (©2017 IEEE [3])

3.3.2 Algorithm Description

When implementing magnetic heading control, torque application is of interest. To apply the strongest torque possible, a magnetic field should be applied on the IM that is orthogonal to the heading of the IM. This is non-trivial in the case of permanent magnets as the field at the IM cannot be instantaneously changed to any desired one, but rather, must be incrementally achieved. This is an example of a limitation of the *EM velocity-wrench bound* that was outlined in Chapter 2.2. To compensate for this, an algorithm is proposed that applies the largest possible instantaneous torque that also reduces IM heading error. However, it must be noted, that the instantaneous axis of rotation of the IM is typically not the one that results in the shortest angular path towards the retroflexed heading. In other words, the IM is rotated along a longer, indirect, path so that more

torque can be applied during the rotation.

The proposed algorithm consists of an optimization of the twist of the EM such as to impart the largest magnetic wrench possible that results in the retroflexion of the MFE. A Jacobian $\tilde{\mathbf{J}}_e$, defined in Eq. (2.9), is used to map twists of the EM to the infinitesimal wrench imparted on the IM. While the aforementioned control strategies in Chapter 3.2 consisted of the inversion of $\tilde{\mathbf{J}}_e$ to compute the necessary EM motion, here, the system not only computes an EM twist from a desired wrench, but also computes what this wrench should be. This is the main conceptual difference from previous approaches and the method answers the question: "*Which EM motion will result in the best implementation of the MFE's task?*".

This implementation relies on maximizing the change in wrench, at each time step, such that the MFE is reteroflexed towards a desired heading $\hat{\mathbf{m}}_{i_{des}}$. Here, the EM twist is optimized. The benefits of optimizing over end-effector motion are the ability to act on and constrain EM motion directly as well as to weigh optimization contributions to favor linear or angular EM motion. This is because magnetic force and torque are functions of both relative positions and orientations of both magnets, and thus, torque can be increased by either rotating the EM or translating it in the proper direction. The height of the EM is kept constant throughout a retroflexion maneuver.

Given the discrete positions of the IM and EM, the linear and angular velocities of the EM, $\dot{\mathbf{x}}_e \in \mathbf{R}^6$, are optimized such that an infinitesimal wrench step reduces heading error; this heading-error-reducing direction is referenced using the subscript "dir" in the objective function of Eq. (3.3).

$$\begin{aligned} \underset{\dot{\mathbf{x}}_e}{\text{maximize}} \quad & \left\| \begin{bmatrix} \delta \mathbf{f}_{dir} \\ \delta \tau_{dir} \end{bmatrix} \right\|^2 \\ \text{subject to} \quad & \|\mathbf{W}_c \dot{\mathbf{x}}_e\|^2 = \text{a constant} \end{aligned} \tag{3.3}$$

Here, the diagonal weight constraint matrix $\mathbf{W}_c \in \mathbf{R}^{6\times 6}$ is used to specify how much the solution should favor translation or rotation of the EM. The constraint is applied to facilitate the computation of the maximum magnitude wrench that results from a fixed amount of motion of the EM. The

optimized vector has multiple units: m/s for linear EM velocity, and $radians/s$ for angular EM velocity. This unit mismatch has the same impact as the linear and angular components of a Jacobian being in disproportion. The weight matrix $\mathbf{W}_c$ is used to eliminate the effect of unit inequality by scaling up the linear weight. By choosing an optimized $\dot{\mathbf{x}}_e$ in the heading-error-reducing direction, the maximum possible infinitesimal wrench is applied that moves the tip such that heading error is reduced.

A set of projection matrices was utilized in the optimization problem to implement the direction preference in the objective function. To specify the favored directions in force and torque, a projection matrix $\mathbf{P}_{ft} \in \mathbf{R}^{6\times 6}$ is utilized which results in the formulation shown in Eq. (3.4).

$$\begin{aligned}\begin{bmatrix}\delta\mathbf{f}_{des}\\ \delta\tau_{des}\end{bmatrix} &= \delta\mathbf{w}_{des} = \mathbf{W}_{ft}\mathbf{P}_{ft}\tilde{\mathbf{J}}_e\mathbf{W}_{EM}\delta\mathbf{x}_e \\ &= \mathbf{J}_o\delta\mathbf{x}_e\end{aligned} \tag{3.4}$$

Here, $\mathbf{J}_o$ denotes the weighted and projected Jacobian used for the optimization, and $\mathbf{P}_{ft}$ is composed of three projection matrices: $\mathbf{P}_F$, $\mathbf{P}_T$, and $\mathbf{P}_E$, all $\in \mathbf{R}^{3\times 3}$, shown in Eq. (3.5).

$$\mathbf{P}_{ft} = \begin{bmatrix}\mathbf{P}_F\\ \mathbf{P}_E\mathbf{P}_T\end{bmatrix} \tag{3.5}$$

The projection matrix $\mathbf{P}_F$ is used to specify a desired direction of force application. Applying a small force in the direction of the desired heading assists in reducing the heading error. This is likely attributed to the effect of the body of the endoscope anchoring against the wall of the colon after its tip has retroflexed more than 90°. This projection is used only in the final 30° of the maneuver and is otherwise maintained as an identity matrix, thus the desired infinitesimal force is passively determined with proper torque application being favored. This matrix is defined as $\mathbf{P}_F = \hat{\mathbf{m}}_{i_{des}}\hat{\mathbf{m}}_{i_{des}}^{\top}$. The infinitesimal torque direction is optimized under a number of premises as described below. A visualization of the concepts at hand is provided in Fig. 3.3.

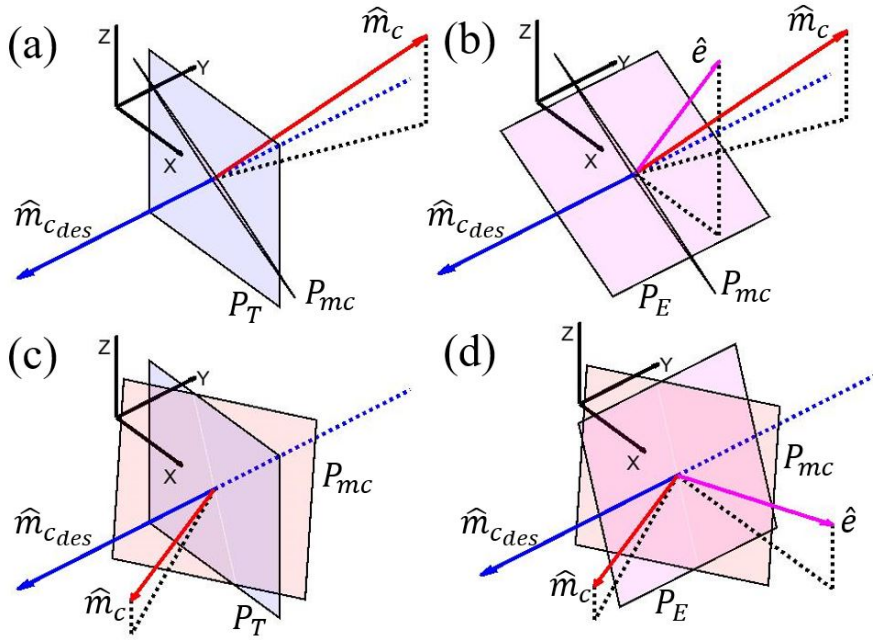

Figure 3.3: Schematic visualization of the DoFs of magnetic torque application by the EM onto the IM. $\mathbf{P}_{mc}$ shows the plane on which the actual applied torque lies and $\mathbf{P}_T$ and $\mathbf{P}_E$ are a visualization of the projection matrices used in the optimization. (a) and (b) show the effect of $\mathbf{P}_T$ and $\mathbf{P}_E$, respectively, along with the applicable torque plane $\mathbf{P}_{mc}$ during the initial stage of retorflexion, while (c) and (d) show these concepts towards the end of retroflexion. Here, the subscript "c" corresponds to "capsule", which, in this work, was the terminology used for the device that houses the IM. (©2017 IEEE [3])

1. Owing to the symmetry of the EM, no torque can be applied in the direction along $\hat{\mathbf{m}}_i$; thus the set of applicable torques must lie on plane $\mathbf{P}_{mc}$ as seen in Fig. 3.3.

2. A torque applied in the direction of $\hat{\mathbf{m}}_{i_{des}}$ does not assist in reducing heading error; thus the plane orthogonal to $\hat{\mathbf{m}}_{i_{des}}$, $\mathbf{P}_T$ in Fig. 3.3 (a, c), is preferred for direction of torque application.

3. The ideal axis that reduces heading error is defined by $\hat{\phi} = \hat{\mathbf{m}}_i \times \hat{\mathbf{m}}_{i_{des}}$. An axis that is chosen to be orthogonal to $\hat{\phi}$ can reduce heading error; however, cannot eliminate heading error completely if this axis is not continuously changed and is thus not preferred. This not-preferred axis is defined as $\hat{\mathbf{e}} = \hat{\mathbf{m}}_{i_{des}} \times \hat{\phi}$. Rotation about $\hat{\mathbf{e}}$ causes rotation away from the desired heading owing to it being orthogonal to $\hat{\mathbf{m}}_{i_{des}}$. The torque axis is desired to be orthogonal to $\hat{\mathbf{e}}$ and thus on plane $\mathbf{P}_E$ as shown in Fig. 3.3(b, d).

Other projection matrices are defined as follows: $\mathbf{P}_T = I - \hat{\mathbf{m}}_{i_{des}} \hat{\mathbf{m}}_{i_{des}}^\top$, $\mathbf{P}_E = I - k_e \hat{\mathbf{e}}\hat{\mathbf{e}}^\top$ where k_e is a scalar that is used to weigh the effect of $\mathbf{P}_E$. This optimization process to find a "strongest" wrench can be thought of as searching the plane of applicable torques, $\mathbf{P}_{mc}$, and choosing $\dot{\mathbf{x}}_e$ that imparts the largest projection of infinitesimal torque onto projection planes $\mathbf{P}_T$ and $\mathbf{P}_E$. Fig. 3.3 (a, b) show these projection planes at the beginning of the retroflexion, while Fig. 3.3 (c, d) show these planes at the end of the retroflexion.

During the beginning of retroflexion $\mathbf{P}_{mc}$ is closely aligned with $\mathbf{P}_T$, therefore the use of $\mathbf{P}_T$ is prioritized by setting k_e to 0, which is maintained until the midpoint (90°) of the retroflexion. From the beginning to this midpoint, $\mathbf{P}_T$ increasingly favors the infinitesimal torque to align with $\hat{\phi}$ owing to the projection plane $\mathbf{P}_T$ becoming orthogonal to $\mathbf{P}_{mc}$. On the contrary, as the tip of the endoscope is rotated from the midpoint to the desired heading, the opposite occurs and $\hat{\phi}$ is favored less and less. When this happens, the algorithm does not punish the the torque axis having a large component along $\hat{\mathbf{e}}$, which has the adverse effect of increasing heading error. To compensate for this effect, the effect of $\mathbf{P}_E$ is scaled up by increasing k_e linearly from 0 at the midpoint of retroflexion to 1 as the endoscope becomes aligned with the desired heading. The symmetry of the EM inherently limits us to 2 DoF in torque, i.e. vectors on $\mathbf{P}_{mc}$ plane in Fig. 3.3, and $\mathbf{P}_T$ and $\mathbf{P}_E$ do not eliminate a full DoFs but rather assist in specifying preferred directions of torque.

It should be noted that, in Eq. (3.3), the infinitesimal changes in wrench are used in the optimization, rather than the absolute wrench. Thus, at each time step, the algorithm does not attempt to achieve the maximum force and torque, but rather their respective change. The reader may notice that the aforementioned projection matrices are used to project the Jacobian that relates changes in wrench to changes in EM twist, while the projection matrices are computed by considering directions of force and torque application. A question may be raised about the disparity between the absolute wrench and the infinitesimal changes in wrench; however, the optimization of the differential wrench facilitates the development of the absolute force and torque directions to be within the constraints defined by $\mathbf{P}_{ft}$. This can be thought of as the algorithm computing the directions for the existing magnetic wrench to "grow".

The diagonal weight matrices $\mathbf{W}_{EM} \in \mathbf{R}^{6\times6}$ and $\mathbf{W}_{ft} \in \mathbf{R}^{6\times6}$, seen in Eq. (3.4), are used for both designating preferred DoFs to act on, or completely constraining the solution. $\mathbf{W}_{EM}$ can be used to punish unwanted EM motion by setting corresponding weights between 0 and 1. Setting a diagonal element of $\mathbf{W}_{EM}$ to 0 results in the respective EM velocity DoF not influencing the resulting infinitesimal wrench, while setting a diagonal element of $\mathbf{W}_{ft}$ to 0 results in the respective infinitesimal wrench being 0. To demonstrate how such weights can be used, in this application the third through sixth diagonal elements of $\mathbf{W}_{EM}$ are functions of the angle between the world vertical axis and the manipulator's last link. This is a simple method to prevent contact of other robot links with the patient. The diagonal matrix $\mathbf{W}_{ft}$ allows for discriminating force and torque effects that dictate which components of the magnetic wrench to optimize. In other words, one can specify whether a higher torque or force application is preferred in a certain direction over another, an example of which is the desired avoidance of lateral force on the colon.

A solution for Eq. (3.4) must be computed. A simple inversion of $\mathbf{J}_o$ is not satisfactory as the desired wrench is unknown. In the interest of real-time computation, Lagrange multipliers are used, with the Lagrange function shown in Eq. (3.6).

$$\begin{aligned}\mathscr{L}(\delta\mathbf{x}_e,\lambda) &= \|\delta\mathbf{w}_{des}\|^2 - \lambda\,\|W_c\delta\mathbf{x}_e\|^2 \\ &= \delta\mathbf{w}_{des}^{\mathrm{T}}\delta\mathbf{w}_{des} - \lambda\,\delta\mathbf{x}_e^{\mathrm{T}}\mathbf{W}_c^{\mathrm{T}}\mathbf{W}_c\delta\mathbf{x}_e \\ &= \delta\mathbf{x}_e^{\mathrm{T}}\mathbf{J}_o^{\mathrm{T}}\mathbf{J}_o\delta\mathbf{x}_e - \lambda\,\delta\mathbf{x}_e^{\mathrm{T}}\mathbf{W}_c^{\mathrm{T}}\mathbf{W}_c\delta\mathbf{x}_e\end{aligned} \tag{3.6}$$

Standard means of setting a scaled gradient equality are used as follows:

$$\begin{aligned}\frac{\partial}{\partial\delta\mathbf{x}_e}\left(\delta\mathbf{x}_e^{\mathrm{T}}\mathbf{J}_o^{\mathrm{T}}\mathbf{J}_o\delta\mathbf{x}_e\right) &= \lambda\frac{\partial}{\partial\delta\mathbf{x}_e}\left(\delta\mathbf{x}_e^{\mathrm{T}}\mathbf{W}_c^{\mathrm{T}}\mathbf{W}_c\delta\mathbf{x}_e\right) \\ (\mathbf{J}_o^{\mathrm{T}}\mathbf{J}_o + (\mathbf{J}_o^{\mathrm{T}}\mathbf{J}_o)^{\mathrm{T}})\delta\mathbf{x}_e &= \lambda(\mathbf{W}_c^{\mathrm{T}}\mathbf{W}_c + (\mathbf{W}_c^{\mathrm{T}}\mathbf{W}_c)^{\mathrm{T}})\mathbf{x}_e\end{aligned} \tag{3.7}$$

Therefore:

$$\mathbf{J}_o^{\mathrm{T}}\mathbf{J}_o\mathbf{x}_e = \lambda\mathbf{W}_c^{\mathrm{T}}\mathbf{W}_c\delta\mathbf{x}_e \tag{3.8}$$

As $\mathbf{W}_c$ is invertible, this expression can be formulated as an eigenvalue problem to solve for $\delta\mathbf{x}_e$,

as shown in Eq. (3.9).

$$(\mathbf{W}_c^{\mathrm{T}}\mathbf{W}_c)^{-1}\mathbf{J}_o^{\mathrm{T}}\mathbf{J}_o\delta\mathbf{x}_e = \mathbf{A}\delta\mathbf{x}_e = \lambda\delta\mathbf{x}_e \tag{3.9}$$

Here, $\mathbf{A}$ is $\in \mathbf{R}^{6\times6}$, the solution vector $\delta\mathbf{x}_e^*$ is denoted as the eigenvector that imparts an EM motion that applies the largest change in force and torque in the desired direction. Using gradient projection methods as introduced by [86], a redundant DoF resulting from the symmetry of cylindrical magnets is utilized for favorable link orientation with respect to the patient's general location. These joint rates acting in the EM's linearized nullspace are referred to as $\delta\mathbf{q}_R$. Finally, the commands are converted into desired joint velocities by using the right pseudo-inverse of the manipulator's Jacobian, denoted by $\mathbf{J}_R^+ = \mathbf{J}_R^{\mathrm{T}}(\mathbf{J}_R\mathbf{J}_R^{\mathrm{T}})^{-1}$. This then produces a minimum joint norm solution which is coupled with the nullspace solution that is integrated and communicated to the low-level robot controller. The joint solution is shown in Eq. (3.10).

$$\delta\mathbf{q} = \mathbf{J}_R^+\delta\mathbf{x}_e^* + \delta\mathbf{q}_R \tag{3.10}$$

3.3.3 Analysis of Optimal Solution

As mentioned above, $\hat{\phi}$ is the ideal axis for reducing heading error and if there was a rigid link between the EM and IM then this axis should always be used to reduce heading error. However, owing to the nature of the dipole field, consideration must be made as to what is the best way to apply a magnetic torque between dipoles. Past works, such as [44, 1, 2], set desired infinitesimal torque directions about $\hat{\phi}$; however, the following discussion demonstrates that this is typically not the most effective axis about which a torque can be applied. The relative poses of the magnets should be considered when determining how a heading error should be minimized. This is the first consideration of torque effectiveness analysis in magnetic robot research.

An ideal torque application axis, $\hat{\xi}$, is defined as the axis about which the greatest torque can be applied on the actuated magnet and is a function of the relative magnet poses. A schematic describing the concept is shown in Fig. 3.4. Consider a simple case where the IM heading is along

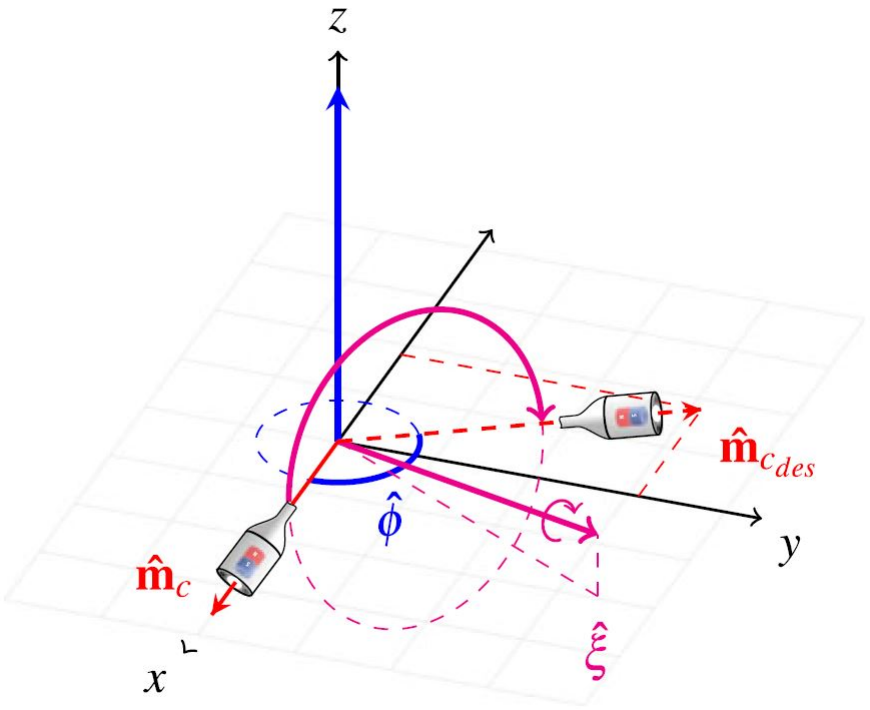

Figure 3.4: The axis $\hat{\phi}$ defines the shortest angular path between current and desired heading. The axis $\hat{\xi}$ denotes the direction of maximum possible application of an infinitesimal change in torque. This schematic demonstrates that the two axes are not necessarily aligned. Here, the subscript "c" corresponds to "capsule", which, in this work, was the terminology used for the device that houses the IM. (©2017 IEEE [3])

the world x axis, $\hat{\mathbf{m}}_i = [1,0,0]^{\mathrm{T}}$, the EM heading is along the world $-x$ axis $\hat{\mathbf{m}}_e = [-1,0,0]^{\mathrm{T}}$, and the IM is located directly under the EM ($\hat{\mathbf{p}} = [0,0,-1]^{\mathrm{T}}$). This is a typical initial configuration during mobile-dipole magnetic actuation where retroflexion would be initiated, and an axis of rotation must be decided. Rotation about the x axis is fruitless owing to axial symmetry of the magnets, the only possible rotations are about y or z, or a combination of the two. It is desired to find the axis of rotation that will result in the largest magnitude of $\delta\tau$, which is defined as follows [1]:

$$\begin{aligned}\delta\tau &= \frac{\mu_0 \|\mathbf{m_e}\| \|\mathbf{m_i}\|}{4\pi \|\mathbf{p}\|^3}\mathbf{S}(\hat{\mathbf{m}}_\mathbf{i})(3\hat{\mathbf{p}}\hat{\mathbf{p}}^{\mathrm{T}} - \mathbf{I})\delta\mathbf{m}_e \\ &= C(3\hat{\mathbf{m}}_\mathbf{i} \times \hat{\mathbf{p}}\hat{\mathbf{p}}^{\mathrm{T}}\delta\mathbf{m}_e) - C(\hat{\mathbf{m}}_\mathbf{i} \times \delta\hat{\mathbf{m}}_\mathbf{e})\end{aligned} \tag{3.11}$$

where C is a constant and the first term considers the projected component of $\delta\hat{\mathbf{m}}_e$ onto the relative

position axis that is normal to the heading of the endoscope, while the second is independent of position.

If $\delta\hat{\mathbf{m}}_\mathbf{e} = [0,0,1]$ then $\delta\tau = [0,-2,0]$, while if $\delta\hat{\mathbf{m}}_\mathbf{e} = [0,1,0]$, then $\delta\tau = [0,0,-1]$ and thus a higher efficiency is observed in the vertical (z) increase in $\hat{\mathbf{m}}_\mathbf{e}$. The two-factor magnitude increase of $\delta\tau$ occurred owing to orthogonality of $\delta\hat{\mathbf{m}}_\mathbf{e}$ and $\hat{\mathbf{p}}$, however, this magnitude will typically scale with the cosine of the angle between them. Seeing that varying the axis of rotation can impact torque magnitude as much as two-fold, it is reasonable to assume that the best axis of rotation is not necessarily the one that defines the shortest path between the current and desired heading. A trade-off will then exist between the magnitude and direction-accuracy of each possible torque axis.

To demonstrate that the proposed wrench optimization algorithm chooses axes other than $\hat{\phi}$, the algorithm's chosen infinitesimal axis of torque application, $\hat{\tau}_{alg}$, was recorded. It should be noted that in previous works this was chosen to be $\hat{\tau}_{alg} = \hat{\phi}$. There exists a visible variance between each trial, shown in Fig. 3.5. This is expected as each retroflexion trial is dependent on the current behavior of the endoscope, thus trials should not be expected to have identical behavior. Data is plotted as a function of the angle between $\hat{\mathbf{m}}_c$ and $\hat{\mathbf{m}}_{c_{des}}$. As the maneuver starts, there is over an 80° difference between $\hat{\phi}$ and $\hat{\tau}_{alg}$. This difference is attributed to $\hat{\phi}$ being nearly vertical (because of $\hat{\mathbf{m}}_c$ being nearly horizontal) while $\hat{\tau}_{alg}$ is nearly horizontal. As the pitch of the tip increases ($\hat{\mathbf{m}}_c$ approaches a vertical heading), the difference between $\hat{\phi}$ and $\hat{\tau}_{alg}$ reduces significantly. When choosing the axis of infinitesimal torque, a compromise must be made between choosing the axis of maximum torque application and an axis that reduces the heading error.

3.3.4 Bench-top Validation

To evaluate the algorithm, a series of bench-top trials were conducted on the platform shown in Fig. 3.2. Of utmost importance in setting experimental parameters was clinical relevance. Plastic tube sizes of 38 mm, 44 mm, 50 mm, and 60 mm were chosen as they fall in the range of adult human colon diameters: 20-120 mm, where a 120 mm diameter can be reached at the apex of the

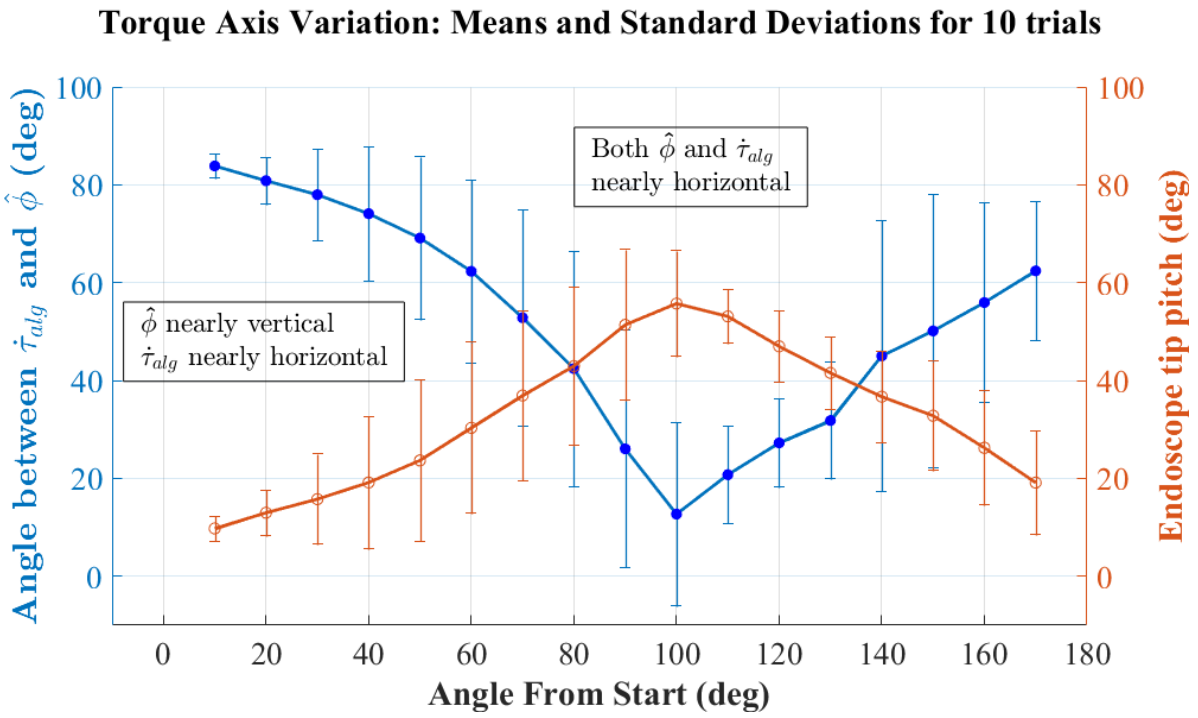

Figure 3.5: A piece-wise linear representation of the means and standard deviations of 10 retroflexion trials showing the difference between the shortest path axis and the chosen optimal rotation axis, where of interest is the general shapes of the curves. The algorithm does not always "choose" a rotation axis that is a certain compromise between being able to apply the most torque that it can and choosing the shortest rotation solution. This suggests that the axis choices are algorithmic and non-random, as the general curve is repeatable with a variance. The high variance between data sets is acceptable and is attributed to the trials being independent of each other, which is expected owing to the system responding to the motion of the endoscope rather than following a pre-planned trajectory. (©2017 IEEE [3])

sigmoid colon [87, 88]. Setting the desired height of the EM necessitates the consideration of both patient location and the decay of field strength with distance. A virtual barrier is defined, referred to hereafter as the "no-cross height", as the vertical distance above the colon wall that cannot be crossed by the EM. Owing to the adult male's mid-saggital abdominal wall thickness being 15-20 mm [89] and an approximate colon tissue thickness of 1 mm [90], the no-cross height was chosen to be 40 mm, 50 mm, and 60 mm for experiments. This allowed for nearly 20 mm of leeway for a layer of fat in a potential patient. An increase in magnet strength can allow for a larger spacing. For each combination of tube diameter and no-cross height, 10 trials were conducted with results shown in Table 3.1. For a trial to be labeled as successful, the endoscope's heading had to reach

within 10° of the desired retroflexed heading. The algorithm completion success rate was 98.8% for EM spacings of 50 mm and below; however, this success rate drastically dropped when the spacing was increased to 60 mm owing to an inability to impart a sufficient magnetic wrench.

To verify the clinical applicability of the method, a set of 10 trials was conducted on a freshly-excised porcine colon, which is anatomically similar to that of a human [91]. The colon was mounted inside a 47 mm inner diameter tube—the mean diameter of the human colon [88]—as shown in Fig. 3.6. The tissue appeared to fully expand into the diameter of the tube, and thus the inner diameter of the colon was approximated to be that of the tube, or 47 mm. As shown in the last row of Table 3.1, a 100% success rate was achieved with a mean maneuver duration of 19.7 s. This is approximately 1.6% of the average duration of adult colonoscopy with no intervention (21.1 ± 10.4 min [92]). During one of the trials inside the 60 mm ID tube at a no-cross height of 50 mm, the endoscope slipped and the external magnet was forced to make motions that were out of the ordinary to eventually achieve a successful retroflexion. This caused a trial time of 47.5 s and thus raised the mean trial time to 17.0 ± 10.8 s. Without this outlier, the mean retroflex time for trials inside the 60 mm ID tube at a no-cross height of 50 mm was 13.6 s. The outlier was not omitted as the algorithm did succeed in overcoming the unexpected difficulty.

It should be noted that trials were a lower no-cross height is used tend to have a shorter time for retorlexion, which can be seen in Table 3.1, owing to a greater applied magnetic wrench. The mean time of retroflexion during the *ex vivo* trial was approximately 5 s slower than that of trials conducted in plastic tubes with similar inner diameters (44 mm and 50 mm) with the same EPM spacing. This longer time of retroflexion inside real tissue is likely attributed to the added resistance of tissue deformation as well as the tissue stretching that is not typically encountered *in vivo* owing to the presence of the mesentery (i.e., tissue that connects organs to the body).

While applying proper forces and torques to achieve retroflexion may be achievable, it is necessary that the resulting reaction on tissue does not induce damage. The applied magnetic force and torque on the IM can be monitored and bounded [93]; however, an additional reaction on tissue—resulting from the bending stiffness of the body of the endoscope applying a moment on

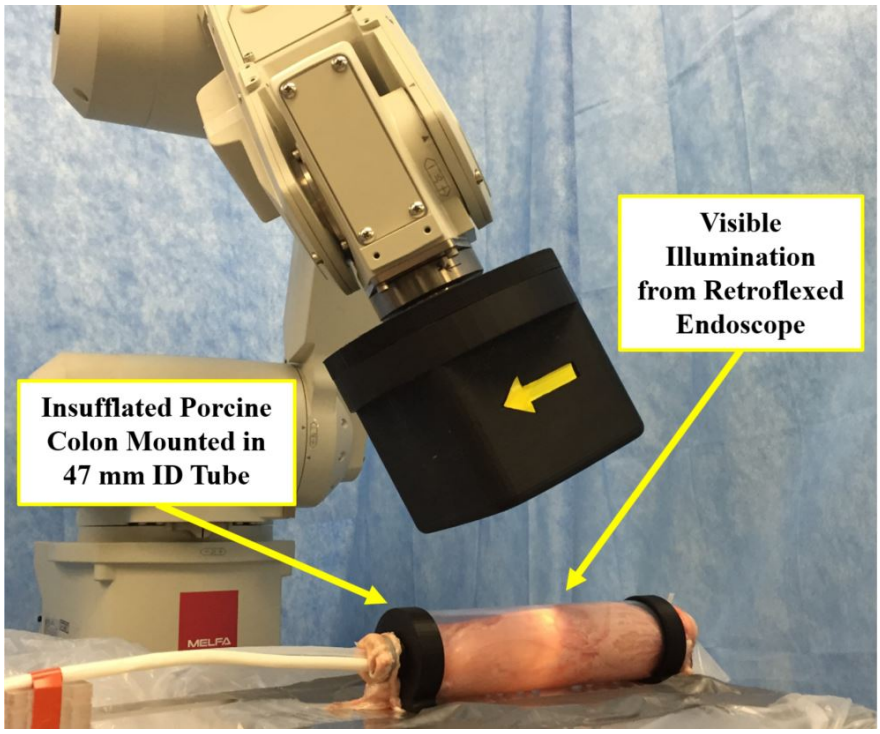

Figure 3.6: Photo of ex vivo trial setup. A set of 10 trials was conducted using porcine colon tissue. (©2017 IEEE [3])

Table 3.1: Experimental results (©2017 IEEE [3])

Tube I.D. (mm)	No-Cross Height (mm)	Mean Time (s)	Std. Dev. (s)	No. Successes out of 10 Trials	Mean Force (N)	Mean Torque (Nm)
60	40	10.5	0.6	10	0.741	0.0111
	50	17.0	10.8	10	0.518	0.0113
	60	15.9	2.8	6	0.403	0.0112
50	40	12.0	0.5	10	0.615	0.0116
	50	14.4	0.9	10	0.465	0.0112
	60	15.9	0.9	2	0.375	0.0107
44	40	11.6	1.4	10	0.663	0.0130
	50	13.3	0.5	9	0.505	0.0129
	60	N/A	N/A	0	N/A	N/A
38	40	14.6	0.5	10	0.591	0.0153
	50	19.3	5.3	10	0.439	0.0151
	60	27.3	5.2	4	0.326	0.0149
ex vivo (47)	50	19.7	2.9	10	0.538	0.0193

the IM—occurs and is present after the tip of the endoscope passes the half-way point of the retroflexion. To experimentally measure the force applied by the endoscope on the colon wall, an experimental setup, seen in Fig. 3.7.a, was designed. A 60 mm ID tube was cut along its length such that the endoscope made contact with one side that was rigidly coupled with a 6-axis force/torque sensor (Nano 17 SI-25-0.25, ATI Technologies Inc., Canada) while the body of the endoscope made contact with the other. As shown in the schematic in Fig. 3.7.b, the body of the endoscope exerts a negligible distributed load on the (what is shown as) bottom tissue wall and is thus ignored. On the other hand, the endoscope applies on the top wall a combination of magnetic force, reaction force from the endoscope body's bending stiffness, and forces from friction and tissue deformation. Although effects of tissue deformation are not considered here, they have been investigated in [94]. The aforementioned negligible distributed load and the reaction force on the endoscope from the endoscope body's bending are similar in magnitude; however, the loads are distributed differently. The measured force is projected onto the normal direction to the tube at the point of contact with the tip of the endoscope, which is known owing to real-time localization. Of importance is resultant tissue stress, rather than force.

To make a worst-case stress approximation, the endoscope is assumed to be oriented such that a minimum surface area is making contact with tissue as to maximize stress, as shown in Fig. 3.7.b. It is assumed that the tip of the endoscope "digs" into the tissue by 1 mm, giving a 1 mm deformation depth. Given a known geometry of the tip of the endoscope, this "critical area" can be computed and is used in any stress computation henceforth. This critical area is outlined in blue in Fig. 3.7.b. Three sets of 10 retroflexion trials at various no-cross heights were conducted inside this sensing tube with best fit curves shown for clarity in Fig. 3.7.c. For each of these sets, the magnetic force that was computed via dipole-dipole model was subtracted to obtain the non-magnetic force profile. This profile, largely dependant on the endoscope body's stiffness as suggested by the increase in non-magnetic force after a 90° angle from start of the maneuver, is represented with best fit curves in Fig. 3.7.c. It is noteworthy that this body stress is significantly lower than the magnetic force, thus monitoring and throttling magnetic force may be sufficient for

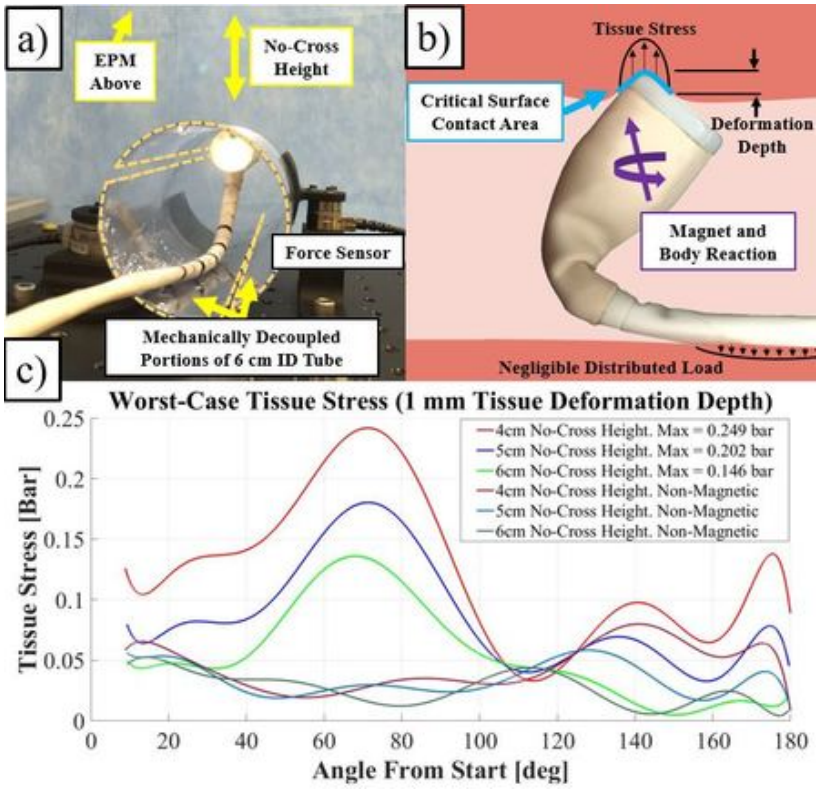

Figure 3.7: a) Setup for force sensing during a retroflex. b) Schematic diagram of the distributed load of the body of the endoscope as well as the stress concentration at the contact point between the tip of the endsocope and colonic tissue. c) Best fit curves of stress computed from force measured through 3 sets of 10 trials and the contact area as computed at the tip of the endoscope, shown in (b). (©2017 IEEE [3])

safe manipulation of the device. As seen in Fig. 3.7.c., the maximum applied tissue stress is 0.249 bar, which is only 8.3% of the 3 bar irrigation pressure that has been shown to not adversely effect tissue [95].

In summary, an algorithm was developed for the autonomous retroflexion of the MFE. Using a real-time force and torque magnitude optimization, the system computes an instantaneous wrench to impart on the IM that results in the most effective motion towards its desired (retroflexed) heading. The algorithm was validated by demonstrating retroflexion of the tip of the endoscope with a 98.8% success rate in plastic tubes of various sizes while the EPM's no-cross height was within 50 mm of the colon. Additionally, retroflexion of the endoscope in an insufflated porcine colon of inner diameter similar to that of the average human colon diameter (47 mm) was demonstrated.

The set of 10 *ex vivo* trials resulted in a 100% success rate in a mean maneuver time of 19.7 ± 2.9 s which suggests feasibility for clinical use.

3.3.5 *In vivo* Validation

To further validate the retroflexion algorithm's performance, an *in vivo* experiment was conducted in a porcine model. Experimental trials were conducted in the large bowel of a 40 Kg female Yorkshire-Landrace cross swine. As the colon that can be feasibly reached is quite short owing to the spiral colon in swine, the experiments were performed approximately 25 cm from the proximal insertion. The swine underwent general anesthesia induction with Telazol (4.4 mg/kg intravenously; Fort Dodge, Ames, Iowa), Xylazine (2.2mg/kg intravenously), and ketamine (2.2 mg/kg intravenously). Following endotracheal intubation and throughout the procedure, the swine was maintained on a semi-closed circuit inhalation of 1% to 3% isoflurane and ventilated. For bowel preparation, the swine was on a clear liquid diet 24-hours prior to the trial and received tap water enemas prior to trial initiation. Tap water enemas were discontinued when the bowel preparation was deemed to be excellent (clear of all stool and debris) by the animal care team and the endoscopist. The animal was sacrificed at the end of the procedure. The colon was then explanted, leak-tested, and examined by an expert gastrointestinal pathologist. The study was approved by the local Institutional Animal Care and Use Committee (IACUC).

The serial robot was then manipulated via a joystick to position the EM, at the robots end-effector, above the swines colon and displaced from the abdomens surface by approximately 5 cm. Insufflation of the colon was implemented via a channel in the flexible endoscope. Each experiment was conducted under full autonomy; the only human input was the pushing of a keyboard button on a personal computer to initiate the algorithm (a functionality that can be easily integrated into the operators handle for the system). The system then proceeded to compute the necessary torque to retroflex the endoscopes tip, and adjusted its behavior in response to the pose of the endoscope. A total of 30 independent autonomous retroflexion maneuvers were performed (15 were conducted with the tether of the MFE fixed at the anus ("constrained trials") and 15 were conducted with the

tether not fixed at the anus ("unconstrained trials"). The purpose of introducing the constraint was to determine if a negative impact would result from allowing an operator to hold the endoscope tether during the autonomous maneuveras the operator holds the shaft of the endoscope in traditional endoscopy. To prepare for the next trial, the MFE was taken out of retroflexion and placed into forward view at 25 cm from the anus. The serial robot was manipulated via a joystick to the MFE tip and localization was confirmed.

Autonomous retroflexion was successful for all 30 trials *in vivo* (n=15 constrained (100%); n=15 unconstrained (100%). The swine survived throughout all trials without any intraoperative or immediate post-procedure/trial adverse events. Upon necropsy, leak testing was successful without evidence of perforation. There was no evidence of gross trauma to the porcine colon and no evidence of microscopic tissue trauma [73]. A timselapse view of a retroflexion is shown in Fig. 3.8. These images were taken using a FE which impeded the MFE's motion. The FE was not present in the lumen during the experimental trials. The mean maneuver time for all trials was 11.3 ± 2.4 seconds. The MFE body constraint did not have a statistically relevant effect on maneuver completion time (10.6 ± 2.2 seconds v. 12.1 ± 2.3 seconds, p=0.074); however, as seen in Fig. 3.9, the trajectory of the MFE during the unconstrained trials appears to be more repeatable.

To demonstrate the autonomy of the system, position information of both the MFE and the EM was collected throughout all trials. In real-time, the EM responds to the endoscopes motions that are perturbed owing to environmental circumstances, such as tissue friction and relative motion of the body. This results in unique trajectories of the EM between trials. The trajectories of the EM and MFE are visibly variable between trials, as shown in the trajectory plot in Fig. 3.9. In Fig. 3.10, the EMs trajectory is discretized during each trial to compare relative EM positions during waypoints from 0% to 100% of the trajectorys completion, in 10% increments. This shows that the velocity of the IM varied throughout the maneuvers. During each time-index through a trajectory, the mean distances between the IM and its start pose (at 0%) were higher for trials where the MFE was not constrained. This effect was expected as the MFE has an additional DoF in the MFE bodys translation.

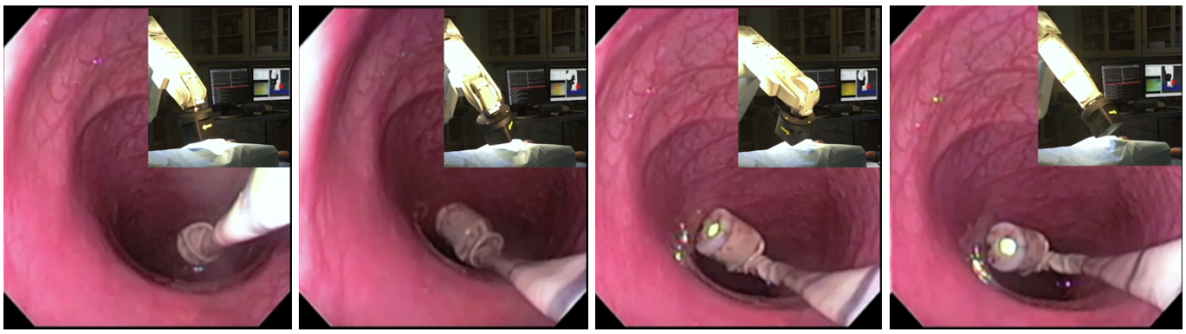

Figure 3.8: A timelapse view of *in vivo* retroflexion.

A plastic colon was used to demonstrate that retroflexion is feasible while a tool is inserted in the MFE (Fig. 3.11). Finally, the ability to use interventional tools *in vivo* was evaluated. The use of biopsy forceps, the placement of a hemostatic clip, and the use of a polypectomy loop are demonstrated in Fig. 3.11. Subjectively, the amount of magnetic wrench was sufficient for an operator to use clinical tools. The magnetic wrench enforced the pose of the MFE such that the operator was able to conduct tissue intervention, suggesting that magnetic fields may be a feasible means for maneuvering a clinical endoscope.

3.4 Conclusions on Control

This chapter has concerned the development of trajectory following strategies using both position and velocity control. CL magnetic control was applied to develop an autonomous retroflexion algorithm. The concept of rotation axis efficiency in magnetic manipulation was introduced, which can be summarized by the statement: "While a magnet can be rotated about an axis that defines the shortest angular path between a current and desired heading, the effectiveness of the rotation about this axis may be weak owing to the inability to apply sufficient torque". This work demonstrated that a controller that simply acts on error alone may not necessarily be the most effective; indirect routes may be superior in terms of the ability to apply magnetic wrench on the IM. This problem is specific to systems where the motion of an actuating magnet is used to change magnetic field and gradient to induce wrench.

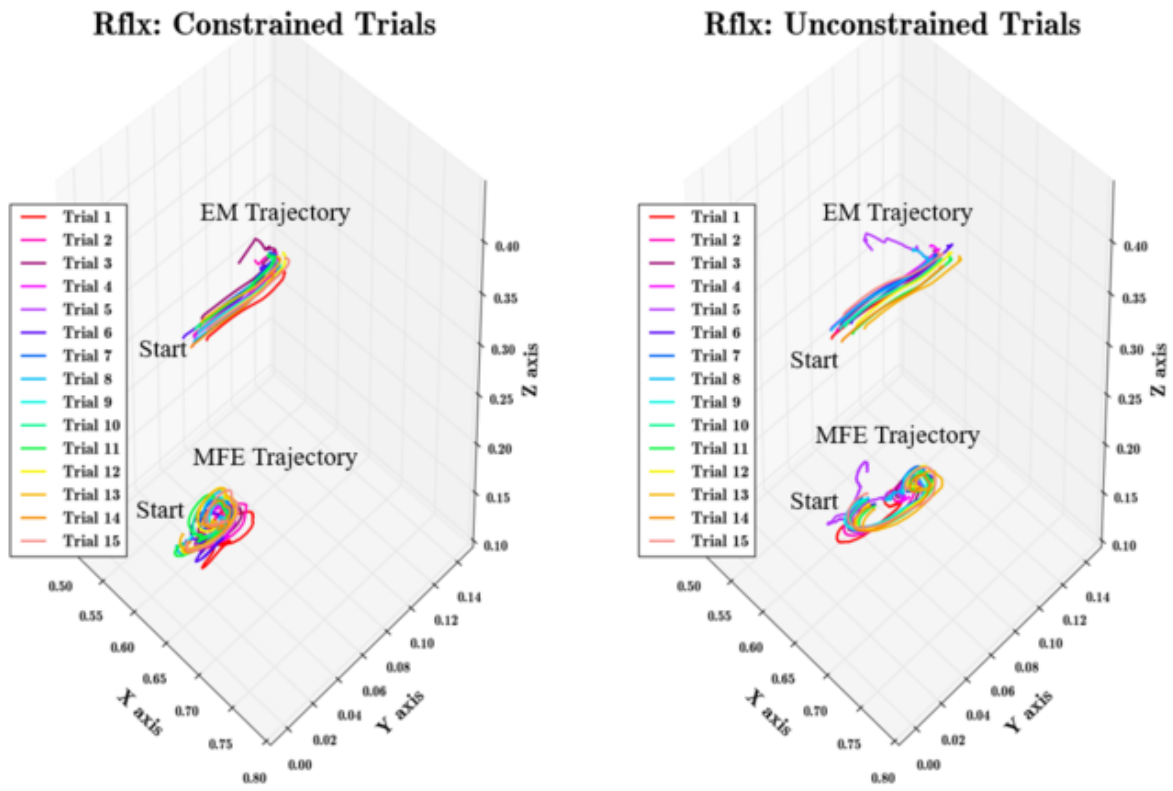

Figure 3.9: The trajectories followed by the tip of the MFE during *in vivo* retroflexion.

An autonomous retroflexion algorithm was validated during benchtop as well as *ex vivo* and *in vivo* experiments [3, 73]. A platform was developed to estimate the worst-case tissue stress that the MFE may apply during retroflexion. The maximum applied tissue stress was determined to be 91.7% below what is necessary to damage tissue. The algorithm retroflexed the MFE with 100% success in 30 trials. A histology technician examined the tissue and found no evidence of gross trauma to the porcine colon and no evidence of microscopic tissue trauma. In summary, the autonomous platform for retroflexing a magnetically actuated endoscope is a robust, fast, and safe technique that may improve the quality of endoscopy.

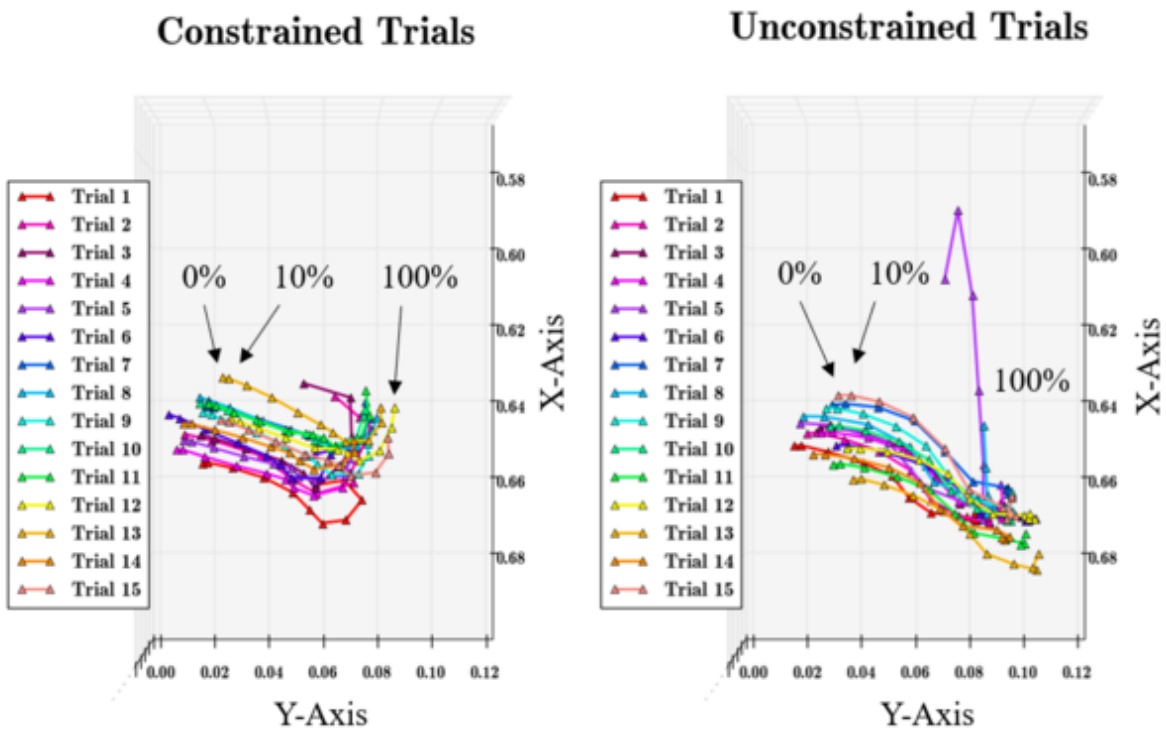

Figure 3.10: Time-based way-points shown on the trajectories of the MFE's tip during *in vivo* retroflexion trials. The MFE's tip did not follow a constant velocity during trials as the way-points are not equidistant, and their spacing varies between trials.

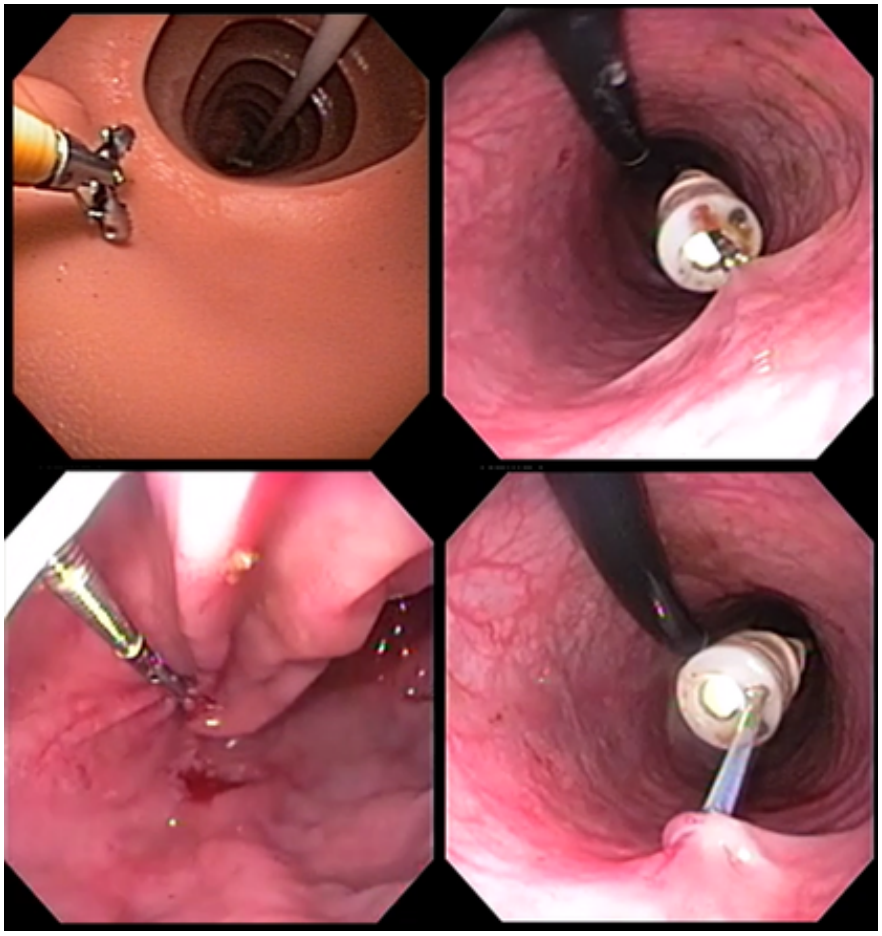

Figure 3.11: The use of a tool while the MFE is retroflexed (top left), the use of biopsy forceps *in vivo* (top right), the use of a hemostatic clip *in vivo* (bottom left), and the use of a polypectomy loop *in vivo* (bottom right).

Chapter 4

Endoscopic Ultrasound Imaging using Magnetically Actuated Transducers

This chapter pertains to the use of the aforementioned magnetic control for actuating a magnetic robotic capsule endoscope (RCE) that has ultrasound (US) imaging capability. This work leverages the aforementioned magnetic control to actuated a micro-US(μUS) probe that is fixed on the body of the RCE. Using real-time RCE pose feedback in conjunction with real-time US feedback with signal processing, the first demonstration of robotic servoing for US imaging is presented. This is also the first demonstration of US servoing without a physical actuator coupling between a controller and US probe. Although robotic US has been thoroughly investigated in the literature, previous existing methods have been limited to robots that are external to the body, or are inserted through a body cavity while remaining physically attached to external systems. The use of higher frequency μUS for mucosal imaging in this work facilitates the viewing of the layers, and thickness, of tissue. This imaging modality is relatively new and was first implemented clinically in 2016 by Exact Imaging (29 MHz, EI, Markham, Ontario, Canada, www.exactimaging.com). This high-resolution modality is necessary for *in-situ* diagnostics. This work contains sections on background and motivation (Chapter 4.1), a description of the system (Chapter 4.2), methods (Chapter 4.3), validation (Chapter 4.4), and a discussion of results (Chapter 4.5). Work related to this chapter resulted in the following publication: Ref. [96]

4.1 Background and Motivation

Today's flexible endoscopy, the gold standard for GI inspection and therapeutics, does not enable *in-situ* diagnostics; rather, a gastroenterologist collects biopsy samples in regions where tissue appears abnormal. Taking multiple biopsy specimens is invasive, can increase procedural cost, can increase procedural risk, and typically multiple days pass before the gastroenterologist obtains a diagnostics report from a pathology laboratory [97, 98, 99, 100]. This chapter pertains to the en-

abling of *in-situ* diagnostics using a robotic endoscopy system that relies on magnetic actuation. The ability to conduct *in-situ* diagnostic pathology during an endoscopy could potentially reduce procedure time, enhance diagnostic yield, and ultimately improve patient care.

Several imaging modalities have been investigated to enhance in-situ capabilities for diagnostics that may expedite, or eliminate, post-procedural pathology. Examples include: narrow-band imaging [101], auto fluorescence imaging [102], Raman spectroscopy [103], x-ray imaging [104], computed tomography (CT) [105], Positron emission tomography (PET) [106], magnetic resonance imaging (MRI) [107], optical coherence tomography [108], and endoscopic ultrasound (EUS) [109]. Of these modalities, EUS is safe, low cost, and has the ability for the generation of images of higher resolution than CT, PET, or MRI; furthermore, it has been demonstrated to provide accurate staging of GI malignancies, including rectal cancer [110].

Recent advancements in EUS technology have enabled high-frequency ($>$ 20 MHz) US, US, that has enabled the study of GI mucosal layers that have a thickness of approximately 1-2 mm [111, 112, 113]. This ability to accurately measure tissue thickness is critical; e.g. the increase of colon wall thickness to 2 mm in the proximal end or 3.5 mm in the distal end is considered pathologic [110]. This US technology has been integrated into ingestible capsules. Capsules with US transducers have been shown to generate mucosal echo images that closely resemble GI tissue histology [114]. Endoscopic technology that facilitates controllable US imaging in the GI tract could enable targeted in-situ diagnostics, reduce procedure time, improve pathology turn-around time, and enhance image guided diagnostic yield. The use of robotics lends itself well to the control of an *in vivo* US probe. The use of robotic US has been thoroughly explored.

The majority of prior works can be grouped into three categories: (C1) robot-assisted probe manipulation where robot motion is OL with respect to US imaging [115, 116, 117, 118, 119, 120, 121, 122], (C2) visual servoing using US image feedback for the steering of a tool [123, 124, 125, 126, 127, 128, 129, 130, 131, 132, 133], and (C3) visual servoing using US image feedback for the steering of the US transducer [134, 135, 136, 137, 138, 139]. The latter two categories involve US image processing of 2D or 3D US images; in other words, a robotic control system operates in CL

with respect to US information. All prior works in this field concern the actuation of extracorporeal robots, or robots that have been partially inserted in a human, e.g. transrectal ultrasound (TRUS) robots [140], thus making them not feasible for navigating an *in vivo* US transducer.

This work is an investigation of the feasibility of the magnetic actuation of a US probe. Magnetic actuation allows for the application of force and torque on a device in the body, has been shown to be used for robot navigation, and does not require a rigid-link connection between an extracorporeal actuation unit, i.e. permanent- or electro- magnet, and an *in vivo* robot. The system developed in this work relies on the continuous acquisition and processing of 1D US signals and the use of these signals for magnetic servoing; i.e. the use of US feedback in magnetic CL control. This work thus falls in categories C2 and C3. This is the first application of: US-based servoing of an *in vivo* device with embedded probes, US-based servoing using 1D US signals, and using magnetic manipulation (i.e. probes actuated with a non-rigid link) to facilitate probe access to remote regions of the GI tract.

This chapter contains a description of a novel robotic capsule endoscope (RCE) that contains μUS probes that was designed and built in the STORM Lab. Transducer outputs obtained from this RCE are processed to obtain a rating of the strength of acoustic signal in each waveform; this rating is referred to as the "echo-signal-rating" or ESR. This ESR is subsequently used for autonomous servoing, via magnetic actuation, of the RCE to facilitate the acquisition of stronger acoustic signals, and thus clearer US images. The main contributions of this work are: (1) the first demonstration of the servoing of a US probe using US feedback using a robot with no rigid connection to extracorporeal hardware for actuation, i.e. magnetic fields, (2) the first demonstration of robotic μUS-based servoing in the GI tract, (3) the first demonstration of using CL magnetic servoing using US signals for measuring spatial distance between acoustic markers, and (4) the development and *in vivo* evaluation of the first RCE capable of targeted μUS imaging of the GI tract.

The autonomous control used in this study facilitates the searching of a transducer configuration (i.e. RCE pose) that results in robust μUS image acquisition, without the need for a user to learn to

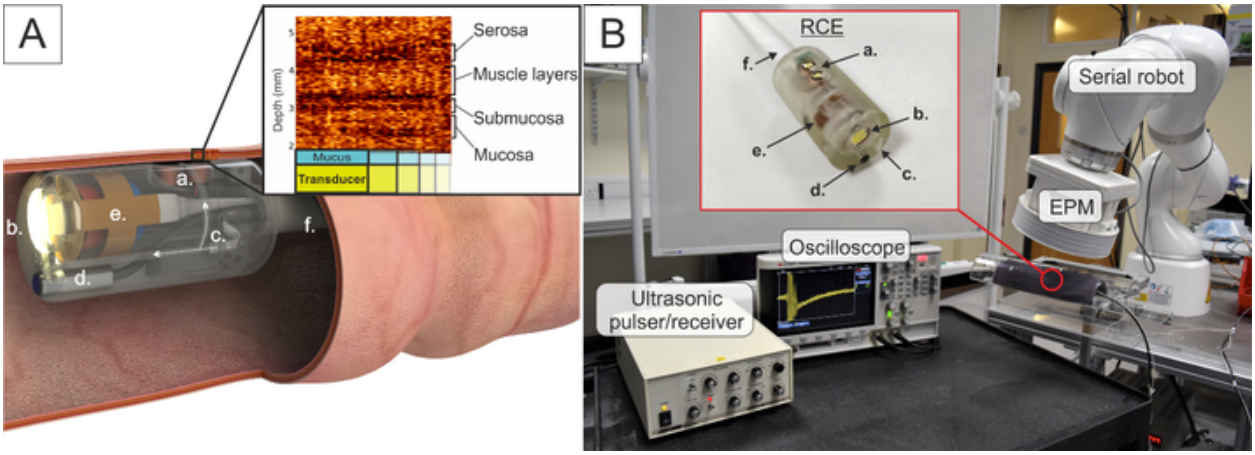

Figure 4.1: (A) Concept image of the RCE in the GI lumen (Image credit: Dr. Joseph C. Norton), the sub-figure shows a B-scan of *in vivo* data where mucosa layers are labeled. (B) A description of system components, where the sub-figure shows the RCE's embedded μUS transducers, LED, irrigation channel, camera, an IPM and circuitry for localization, and the device's tether.

manually navigate the robot. Real-time localization of the RCE allows for tracking the trajectory of the devices as it traverses the lumen thus allowing for determining relative poses between lesions or landmarks, e.g. an abnormality exists at approximately 10 cm from the cecum. The experimental validation in this work includes a characterization of the interplay between RCE control parameters and μUS signal strength, benchtop validation of an autonomous μUS signal strength-improving algorithm when used only in tilting the RCE as well as when using in linear-traversal, and the evaluation of this algorithm *in vivo*.

4.2 System Description

The system used in this chapter consists of the custom-made RCE with two embedded μUS transducers, an IPM for actuation, an extracorporeal serial robot with an EPM mounted at its end-effector, a computer and circuitry that facilitates magnetic actuation, and US driver and processing electronics. This section will describe these components in detail. A conceptual image is shown in Fig. 4.1(A) where the RCE is moving through the GI lumen and generating a 2D US visualization, i.e. B-scan, where layers of the mucosa are visible; this is an actual *in vivo* image captured by the RCE.

4.2.1 Robotic System

The RCE, Fig. 4.1(B), consists of a 3D printed housing (Form 2, Form Labs, Standard Clear resin), contains an IPM (11.11 mm diameter and length cylinder, Neodymium Iron Boron, N52 grade, D77-N52, K&J Magnetics, USA), circuitry for RCE localization [53], two μUS transducers with custom circuitry, a camera (MO-T1003-65-N01, a CMOS transducer, Misumi), an irrigation channel, and a light emitting diode for illumination. Two transducers, Tx1 and Tx2, are embedded in the RCE in close proximity; however, only one is used at a time owing to hardware limitations of the system. Electronics that are internal to the RCE, as well as an irrigation channel and camera wire, are connected with extracorporeal circuitry via a Pebax tether. The IPM is actuated via the same EPM that is used in other chapters of this dissertation. The EPM is kinematically controlled via a medical grade 7 DoF serial robotic manipulator (LBR Med, KUKA AG) (Fig. 4.1(B)). The localization strategy results in a 100 Hz 6 DoF pose of the RCE. The tilt and roll of the RCE are computed from this pose, the convention of which is shown in Fig. 4.2. The roll of the RCE, or γ, is defined as a rotation about the RCE's heading from a nominal. The tilt of the RCE, or α is defined in Eq. (4.1) where $\hat{\mathbf{z}}$ indicates the inertial vertical axis.

$$\alpha = cos^{-1}\Big(\frac{\hat{\mathbf{m}}_i^{\mathrm{T}}(\mathbf{I}_3 - \hat{\mathbf{z}}\hat{\mathbf{z}}^{\mathrm{T}})\hat{\mathbf{m}}_i)}{(\mathbf{I}_3 - \hat{\mathbf{z}}\hat{\mathbf{z}}^{\mathrm{T}})\hat{\mathbf{m}}_i}\Big) \tag{4.1}$$

This localization feedback is assumed to be ground truth throughout this chapter. System software is implemented using the Robotic Operating System (ROS) middleware running on an Ubuntu operating system [74].

The expression for the magnetic control used in this work are similar to those outlined in 3. Joint positions of the serial manipulator are integrated using the solution to Eq. (4.2). Here, $\delta\mathbf{w}_{des}$ is a culmination of PID controls on RCE position, velocity, and heading, ζ is a small damping

factor, and $\mathbf{J}_e^{\#}$ is a pseudo-inversion of the magnetic actuation Jacobian.

$$\begin{bmatrix} \mathbf{I} & \mathbf{0} \\ \mathbf{0} & \mathbf{S}(\hat{\mathbf{m}}_e)^{\mathrm{T}} \end{bmatrix} \mathbf{J}_R \delta\mathbf{q} = \mathbf{J}_A \delta\mathbf{q} = \mathbf{J}_e^{\#} \delta\mathbf{w}_{des} \tag{4.2}$$

$$\delta\mathbf{q} = \mathbf{J}_A^{\mathrm{T}} (\mathbf{J}_A \mathbf{J}_A^{\mathrm{T}} + \zeta \mathbf{I}_3)^{-1} \mathbf{J}_e^{\#} \delta\mathbf{w}_{des}$$

4.2.2 Ultrasound System

The RCE system consists of both IPM pose feedback as well as acoustic feedback from transducers, or μUS waveforms. The transducers are 5 mm in diameter, they are composed of polyvinylidene fluoride, have a center frequency of 30 MHz, and a physical focus point at 6 mm from their curved surface. The transducers are wired to a custom printer circuit board in the RCE which is connected to extracorporeal circuitry via micro-coaxial cables (42 AWG core, 9442 WH033, Alpha Wire, Elizabeth, USA) that pass through the tether of the RCE. Transducers were controlled via a commercial pulser/receiver which also amplified signals received from the transducers (DPR300, JSR Ultrasonics, Imaginant Inc, Pittsford, USA). Feedback signals were captured and digitized via an oscilloscope (DSOX2002A, Keysight Technologies). The received digitized signals were used to form 1D logarithmic images, or A-scans via envelope-detection using a Hilbert transform, and via logarithmic compression. The time-based stacking of these A-scans into a 2D image results in a B-scan.

A custom Python program, that was integrated with ROS, was developed to capture waveform information from the oscilloscope at approximately 3 Hz. This program was written using the Universal Serial Bus Test and Measurement Class library and a Keysight Technologies API. The received acoustic signal is subject to a ringdown effect that takes the form of oscillatory signals that result from the "firing" of transducers. A ringdown-compensation filter was implemented to remove its effects. Given a waveform portion in the form of $\mathbf{p}_w$, the ringdown-compensated waveform is computed as shown in Eq. (4.3). Typically, the waveform portion that was ringdown-compensated was the acoustic signal that had a range of approximately 2 mm. A complete system

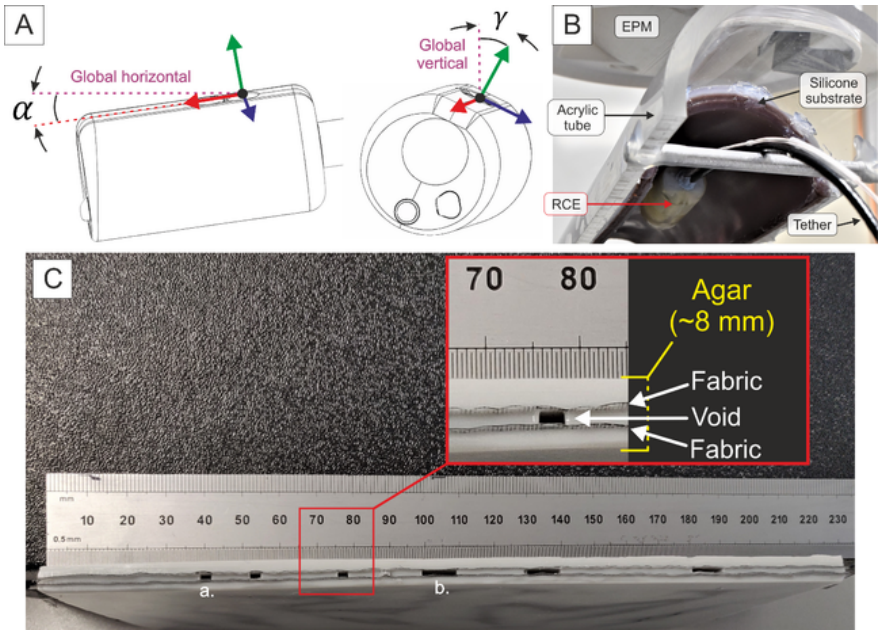

Figure 4.2: (A) Convention for RCE tilt and roll (B) silicone phantom and (C) acoustic phantom that is composed of agar (Image credit: Dr. Joseph C. Norton). The voids have width of 3 and 10 mm, respectively for void a. and b. The spacings between voids, beginning from the left-most, is as follows: 10, 20, 20, 20, 40 mm.

schematic is shown in Fig. 4.3.

$$\mathbf{p}_{w_r} = \mathbf{p}_w - \frac{\sum_{i=1}^{n} \mathbf{p}_w}{n} \tag{4.3}$$

4.2.3 Experimental Platform

benchtop experimentation was conducted using two custom-fabricated acoustic phantoms, shown in Fig. 4.2(B) and Fig. 4.2(C), where the first is a silicone phantom and the latter is an agar-based phantom. The silicone phantom (200 mm in length, 7 mm thick and made from Ecoflex 00-30 silicone, Smooth-on, with 10% Slacker by mass) was used for mechanically-oriented experiments. An agar-based phantom was later manufactured using an existing recipe and protocol [141]. This agar phantom was fabricated via casting embedded pockets of air. Air pocket sizes and positions were known owing to the mold being laser-cut. These air pockets were later used to validate distance-measurements using US signals.

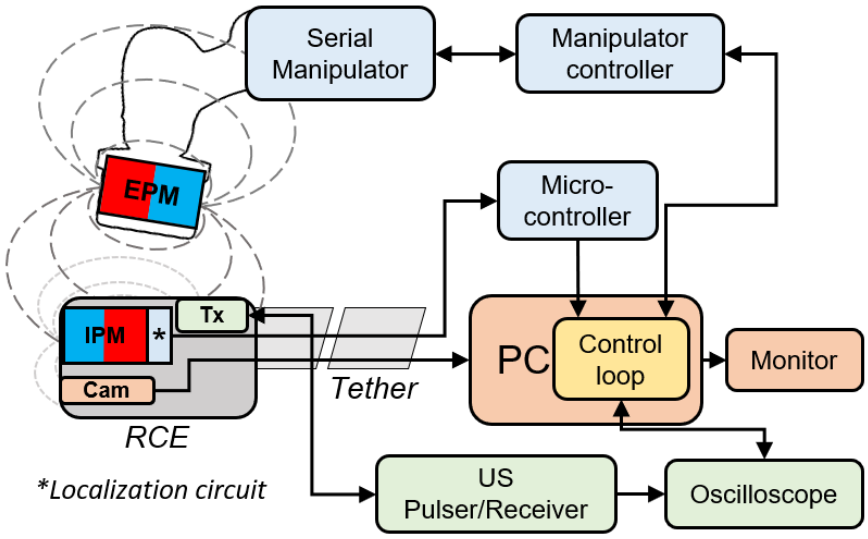

Figure 4.3: System schematic. A diagram that summarizes the data flow between the major components of the RCE system. (Image credit: Dr. Joseph C. Norton)

4.3 Methods

4.3.1 Echo Signal Rating

A US image rating method is necessary in implementing a US servo system. As a universal 1D US image quality metric does not exist, a custom method was used in this work. The echo-signal-rating, or ESR, is an amplitude-based rating metric that is computed by filtering the incoming raw μUS signal and computing a peak-to-peak amplitude. This method of rating an US signal is not unique; however, an amplitude-based method is relevant here as the magnitude of acoustic echoes is of interest.

This waveform processing algorithm, written in Python, does the following: (1) trims the raw waveform an array of Voltages to a desired starting processing depth (2) applies a forward-backward linear filter using SciPy (3) flattens the signal using a low pass filter to make relative echo magnitudes appropriate (4) identifies the maximum peak-to-peak waveform amplitude range in the waveform and (5) filters this peak-to-peak value over time. The ESR has a higher magnitude when echoes are of higher magnitude respective to other values in the individual waveform. A high ESR indicates that acoustic information is present and that this information should be of

interest. This does not necessarily mean that the image is clinically-significant, e.g. tissue layers are visible. The determination of image content is left to an operator. A ringdown-compensation approach, similar to that described above, was employed in the first portion of the waveform to eliminate ringdown effects. ESR feedback provides the RCE system with a real-time measure of μUS image quality. The term "quality" is refers to the overall, amplitude-based, contrast of the image. As mentioned above, this chapter contains references to A-scans (1D) and B-scans (2D). An additional 2D visualization that will be referenced is the "waveform-scan". This visualization is a time-series of the 1D filtered signals that are used for ESR computation.

4.3.2 Autonomous Echo-Finder Servoing Algorithm

With no μUS feedback, an operator, e.g. clinician, would be left to manually perturb a magnetic field in hopes of obtaining a μUS image from which diagnostic information could be obtained. As ESR information is available in real-time, an echo-finder algorithm (EFA) was developed to enable an autonomous search for a strong echo. This task is well-suited for autonomy as (1) μUS transducers are sensitive to the contact mechanics between their surface and tissue and thus misalignment of the surfaces may produce poor images, (2) relative motion of organs in living beings may affect transducer-tissue contact thus introducing further difficulty to obtaining a high-quality image, and (3) the configuration of the environment, i.e. lumen, is unknown to the RCE system making regular pose-servoing impractical.

An overview of the RCE control system is illustrated in Fig. 4.4. The tilt of the RCE is continuously incremented until a signal with high ESR is found. Once a high ESR signal is observed, ESR_{thresh}, the RCE attempts to maintain its pose. The system re-enters the search-routine once the ESR drops below a lower threshold. The RCE's tilt is incremented between an upper and a lower bound.

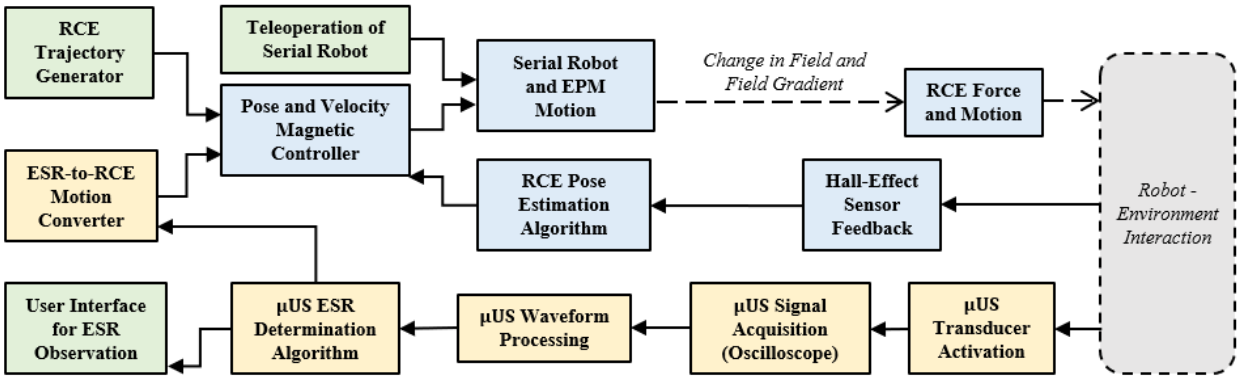

Figure 4.4: Control system for the RCE system. This schematic shows the flow of information between the US system (yellow), magnetic control system (blue), and auxiliary inputs and outputs (green).

4.3.3 Echo-Finder Servoing During Linear Motion

The EFA algorithm was extended to enable autonomous linear translation during which high-quality images are acquired. Such functionality may enable the measurement of lesion size, of relative lesion positions, and potentially autonomous scanning of a lumen region. This translational EFA, or TEFA, consists of the use of the EFA with CL magnetic translations occurring when the ESR is of sufficient magnitude. The system begins by searching for a high ESR image via EFA and enters a translation routine once found. The amount of RCE tilt at which a high ESR was found is recorded and this becomes the desired heading of the RCE during translation. A lower and upper bound for tilt is then updated in case the EFA must be used again. The RCE translates until the ESR drops below a lower threshold.

4.4 Validation

Benchtop and *in vivo* validations for the proposed method were conducted with an intent of demonstrating the feasibility of the use of robotics and autonomy for robust μUS imaging of bowel tissue. Benchtop work was performed with the primary goal of characterizing and refining the system in a known, robust environment and included the characterization of the interplay between RCE motions and μUS signal quality, as well as the preliminary validation of the EFA algorithm.

4.4.1 Benchtop Evaluation

4.4.1.1 Characterization of the Interplay between RCE Control Parameters and μUS imaging

The purpose of this characterization was to evaluate relationships between RCE control parameters and the resultant μUS image quality. Given that the μUS transducers have a single direction, i.e. linear, an improper tilt, roll, or insufficient contact force may result in a loss of acoustic coupling between the transducers and tissue. The tilt and roll of the RCE are known from localization feedback. The magnetic coupling force is estimated using the dipole model. Owing to the orientation of the IPM, the roll of the RCE cannot be controlled; however, it is of interest for future experiments as it may explain the lack of acoustic coupling. As a compensation for an inability to control roll, the RCE was designed with the IPM embedded off-center. This positioning results in a restorative torque applied on the RCE as described in [6]. The RCE thus has a preference of the transducers facing the EPM, and thus vertical as the EPM hovers over a patient. The experimental setup used for these characterizations is shown in Fig. 4.2(B).

The effects of the following parameters were evaluated: (A) US coupling medium, (B) transducer-tissue contact force, (C) probe tilt, and (D) probe roll. Procedures and observations are addressed in sequence: (A) the acoustic signal was observed to degrade when no coupling medium was present. The signal was similar when a medium of water or US gel was used. The RCE contains a water-channel with an output near the transducers to facilitate acoustic coupling. The presence of acoustic coupling medium is not expected to be an issue *in vivo* owing to the natural secretion of mucus in the bowel [142]. (B) Five trials were conducted where contact force vertical magnetic force) was incremented, via operator teleoperation of the EPM, from 0.25 to 2.5 N. A-scans were acquired during all trials. The relationship between contact force and image quality does not appear to be linear or repeatable; however, higher forces tend to indicate stronger signals.

It is likely that a minimum contact force is needed for acoustic coupling to occur, i.e. transducer face is in contact with tissue, and other experimental factors may dictate signal acquisition after this

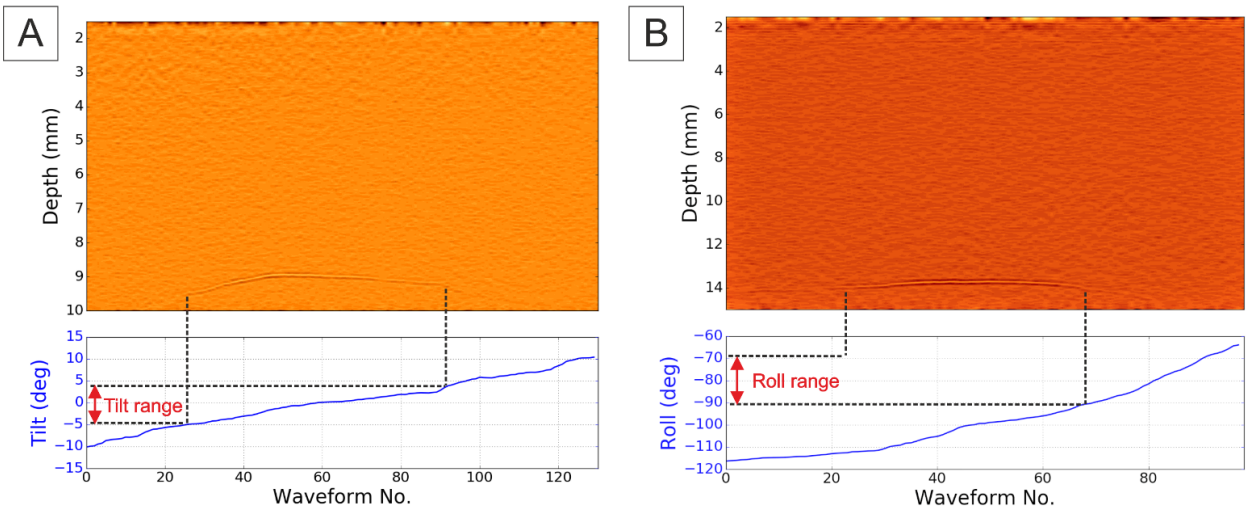

Figure 4.5: (A) Sample tilt-characterization trial (B) sample roll-characterization trial.

threshold. It should be noted that magnetic force should be minimized to avoid mucosa damage. A prior study has shown that no damage was inflicted on a pig mucosa when irrigation pressures of up to 3 bar were applied [95]. The maximum (worst-case) pressure expected from this RCE is 0.75 bar. This was calculated assuming a RCE tilt angle of 45°, tissue indentation of 1 mm and a maximum contact force of 2.5 N. (C) Five trials were conducted by an operator manually teleoperating the EPM to tilt the RCE between -10° and 10°. The strongest acoustic coupling existed in a range of 3°. (D) Five roll trials were conducted where an operator rolled the RCE by hand, as this actuation DoF is not controllable. The range of roll that resulted in acoustic coupling was 10.5°. Same waveform-scans, i.e. time-series scans of filtered waveforms, of tilt and roll trials are shown in Fig. 4.5. The conclusion of these characterization trials are the following: acoustic coupling medium should be used when possible, magnetic coupling force should be kept high enough to obtain physical contact between transducer and tissue, image quality is sensitive to RCE tilt and thus this DoF should be controlled with caution, and the RCE is sensitive to roll (although less than tilt) which motivates a future work of enabling active roll-actuation.

4.4.1.2 RCE Magnetic Servoing (No μUS Feedback)

The characterization results were used to determine which specific parameters should be controlled to acquire μUS signals and their ranges. This was done to determine whether, in the case that the environment configuration is known, it is feasible to simply command a relative pose of the RCE with respect to the environment and obtain μUS echoes robustly.Two target configurations were specified based on characterization data. The two configurations were: (i) -2° tilt and 1 N of contact force, and (ii) 3° tilt trials using these configurations. A 0.6 N contact force was commanded in all trials. In the first, 2 of 5 repetitions acquired μUS signals, while in the second 5 of 5 repetitions did. The 70% success rate of these trials suggests that servoing that is only magnetic (no US feedback) may be feasible if the environment is exactly known; however, this is not the case in practice.

In a similar manner, the ability of the system to translate while acquiring acoustic images was evaluated. Five OL, teleoperated, trials as well as five CL, autonomous, trials were conducted. All teleoperation trials in this work work conducted to develop an intuition for the process of carrying out imaging manually; such trials were not usability studies. A straight-line trajectory was commanded. During teleoperation, the user was asked to manually keep the tilt between 0° and 1°, while during autonomous trials, the tilt was controlled autonomously (set point 0°). During all trials, a contact force of 0.6 N was commanded. The commanded tilt was chosen based on the aforementioned tilt characterization. A-scans were acquired during all trials and at least some acoustic coupling was observed in every repetition. Acoustic coupling was sporadic. As, in practice, the configuration of the environment is unknown, this method of μUS image acquisition is not practical.

4.4.1.3 Probe Servoing: Closed-loop in Magnetics and μUS

The feasibility of closing a control loop using both magnetic fields and μUS feedback, i.e. ESR, was evaluated using a series of experiments. The experiments included teleoperated trials where an operator that was familiar with the system commanded EPM motion to, in turn, tilt the

RCE. The operator observed ESR feedback in these trials and was thus aware of acoustic coupling quality. During all experiments, the orientation of the phantom, i.e. silicone (Fig. 4.2(B)) or agar (Fig. 4.2(C)) tissue phantom, was unknown. As several experiments were conducted, they are labeled and described below.

- **Trial-EFA-1**: The EFA was evaluated on a silicone phantom that was mounted in an acrylic half-pipe. Trials were conducted via teleoperation and autonomy. The phantom was mounted in a horizontal configuration. The success criteria for these experiments was the observation of robust acoustic coupling.
- **Trial-EFA-2**: Identical protocol to Trial-EFA-1. Phantom mounted with an arbitrary tilt.
- **Trial-EFA-3**: The EFA was evaluated on an agar phantom. The phantom was tilted by approximately 2°. The success criteria for these experiments was the observation of robust acoustic coupling.
- **Trial-EFA-4**: Identical protocol to Trial-EFA-1; however, once acoustic coupling was autonomously achieved by the RCE, a user interfered in the experiment by manually perturbing the RCE by either teleoperating the EPM to override the autonomous routine, or by pulling the tether of the RCE.
- **Trial-TEFA-1**: The translation distance for the RCE was 15 cm on the agar phantom. The success criteria for these experiments was the observation of robust acoustic coupling as well as the observation of markers, i.e. air gaps, in the agar phantom. Although both small and large air gaps were designed in the phantom, this experiment targeted the observation of large gaps. The phantom contains three large (10 mm wide) air gaps.
- **Trial-TEFA-2**: Identical protocol to Trial-TEFA-1; however, this experiment targeted the observation of small gaps. The phantom contains three small (3 mm wide) air gaps.

Benchtop servoing results are displayed in Table. 4.1. The EFA algorithm was nearly 100% successful. During Trial-EFA-4, the algorithm failed to acquire images owing to a lack of US

Table 4.1: Benchtop Evaluation of Magnetic-μUS Servoing

Trial	Phantom	n	Mode	Result
EFA-1	Silicone	5	Teleoperated	Robust acoustic coupling in 100% of reps
			Autonomous	Robust acoustic coupling in 100% of reps
EFA-2	Silicone (tilted)	5	Teleoperated	Robust acoustic coupling in 100% of reps
			Autonomous	Robust acoustic coupling in 100% of reps
EFA-3	Agar (tilted)	10	Teleoperated	Robust acoustic coupling in 70% of reps
			Autonomous	Robust acoustic coupling in 100% of reps
EFA-4	Silicone	5	Autonomous	Robust acoustic coupling in 80% of reps
TEFA-1	Agar	10	Autonomous	100% of markers located, accuracy: 1.2$\pm$1.0 mm
TEFA-2	Agar	10	Autonomous	66.7% of markers located, accuracy: 0.8$\pm$0.5 mm

coupling medium, i.e. gel. Sample results of Trial-EFA-3 and Trial-EFA-4 trials are displayed in Fig. 4.6 and Fig. 4.7, respectively. It should be noted that all trials done using the silicone phantom were conducted before any trials with an agar phantom. The silicone phantom was developed first and used owing to favorable mechanical properties. The agar phantom was used in later experiments owing to its favorable acoustic properties.

Linear trajectory trials, TEFA-1 and TEFA-2, were all conducted autonomously and robust μUS images were acquired during all trials. All large markers were detected (TEFA-1) and 66.7% of small markers were detected (TEFA-2). As the widths of markers and spacings between markers are known, the measured values were computed where relevant, i.e. a width or gap spacing could not be computed if one of the markers was not visualized. Spatial measurements can be taken by generating a "spatially-relevant" B-scan. Rather than stacking A-scans together sequentially, as is done in the generation of a B-scan, waveforms can be distance-stamped (rather than time-stamped) and an image with a laterally-accurate distance axis can be generated. The ability to distance-stamp waveform stems from the system's capability for localization. A B-scan, a spatially-relevant B-scan, and their associated waveform-scans are displayed in Fig. 4.8.

The gap measurement error in TEFA-1 trials was 1.2$\pm$1.0 mm (n=20) and the marker width measurement error was 1.3$\pm$1.0 mm (n=30). The gap measurement error in TEFA-2 trials was 0.8$\pm$0.5 mm (n=8) and the marker width measurement error was 0.7$\pm$0.4 mm (n=20). The total accuracy of measurement of all gaps was 1.0$\pm$0.9 mm (n=28) and for measurement of all widths

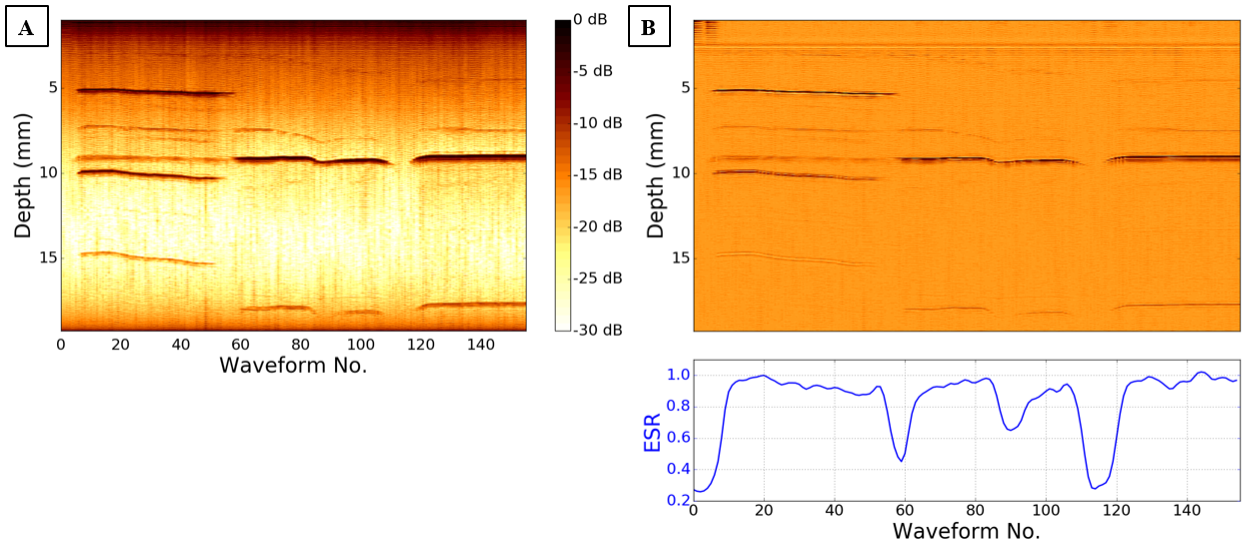

Figure 4.6: Sample results from an EFA-3 trial. A B-scan is shown in (A). A waveform-scan is shown in (B). The waveform-scan consists of sequentially stacked filtered signals that are used for the computation of US signal quality, or ESR.

was 1.1±0.9 mm (n=50). During TEFA-1 trials, a loss of acoustic coupling, i.e. ESR droped below ESR_{thresh}, occurred an average of 0.2±0.4 times per trial. This value was 1.3±1.5 for TEFA-2 trials. Acoustic coupling was recovered after each loss of coupling in all but a single instance. These experiments demonstrated both the feasibility of US servoing, as well as the feasibility of conducting autonomous scanning during translation.

4.4.2 *in vivo* Evaluation

in vivo evaluation was conducted to demonstrate the feasibility of performing μUS imaging on live tissue in the turbulent and convoluted environment of a body. All *in vivo* work was performed at an animal research facility located at the Roslin Institute, University of Edinburgh. The study was conducted under Home Office (UK) License (Procedure Project Licence (PPL): PF5151DAF) in accordance with the Animal (Scientific Procedures) Act 1986. The choice of pig as testing model is based on their human comparable GI anatomy [91]. This includes bowel dimensions, particularly lumen caliber and bowel wall structure. The experiments were conducted in an endoscopy suite where a mobile x-ray machine ("C-arm" - Ziehm Vision FD) was used for visualizing the RCE.

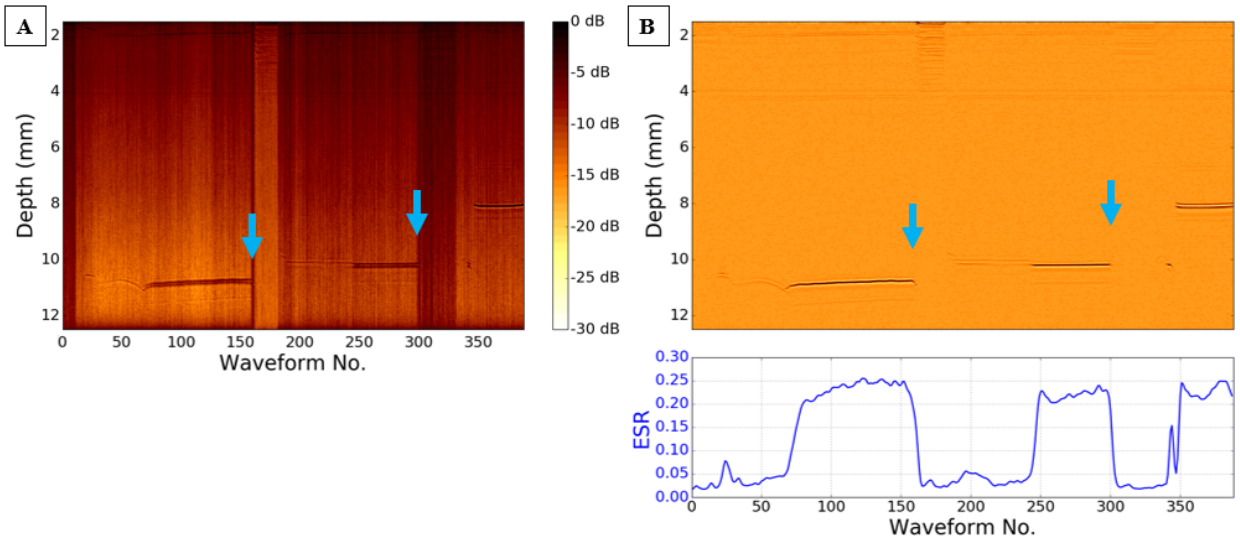

Figure 4.7: Sample results from an EFA-4 trial. Once the RCE autonomously obtained acoustic coupling, an operator perturbed the system until this coupling was lost. The RCE then re-entered an echo-search routine, i.e. the EFA, until an echo was obtained again. The approximate points of disturbance are indicated via arrows. A B-scan is shown in (A). A waveform-scan is shown in (B).

This imaging was in no way used by operators or the algorithms during trials where data was recorded. The lumen was cleaned prior to experiments. Trials were conducted at approximately a 20 cm distance into the lumen.

The value of ESR_{thresh} was set via calibration procedure: a sequence of A-scans was collected before trials began and an ESR value was based subjectively based on a B-scan evaluation. An operator chose the ESR threshold value and hard-coded it in the EFA's code. Teleoperation trials consisted of an operator controlling the pose of the EPM that resulted in pose changes of the IPM. The operator was able to visualize the ESR. The autonomous trials consisted of an operator starting the EFA via push-of-button. Tissue was visually inspected for signs of trauma after experiments; none was observed.

In teleoperation experiments, the operator could not find robust echoes. Faint echoes were seen in 2 of 5 repetitions and it was noted that the task had a high cognitive burden owing to the requirement of rapidly controlling multiple variables in a complex and dynamic environment. In autonomous, EFA, experiments, the system acquired echoes in each repetition of which three (of

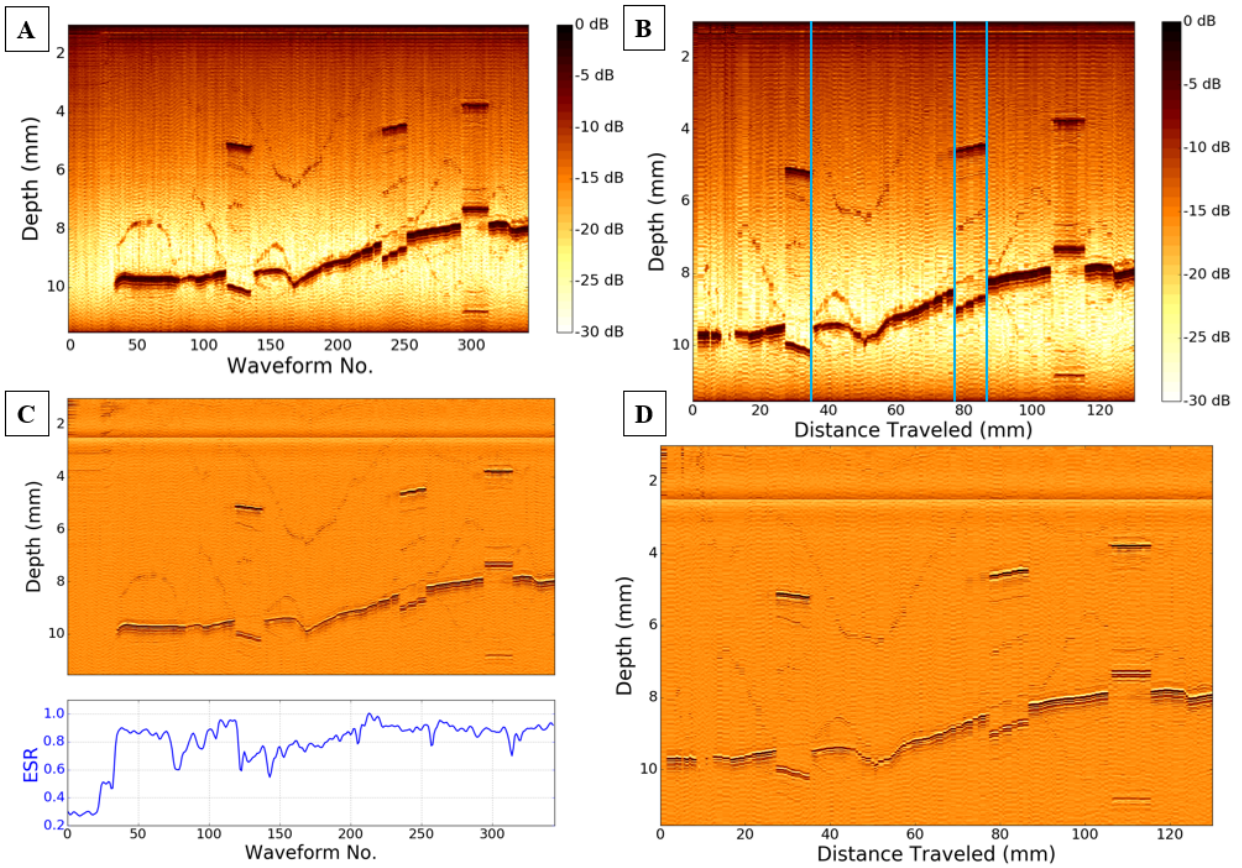

Figure 4.8: Sample result visualizations of TEFA-1 trials. A B-scan is shown in (A) where the horizontal axis refers to the waveforms acquired. A spatially-relevant B-scan is shown in (B) where the horizontal axis has a unit of mm and sample distance markers are displayed. Such markers were used for obtaining distance measurements. The waveform-scan, i.e. stacking of filtered signals used to compute ESR, is shown in (C). A spatially-relevant waveform-scan is shown in (D).

five) were strong. Sample B-scans from EFA trials are shown in Fig. 4.9. The robot was able to react to a change in the ESR and briefly maintain the configuration at which the strong echo was acquired, thus improving imaging robustness. A sample output from the C-arm is shown in Fig. 4.10.

4.5 Discussion and Conclusion

This study demonstrated the feasibility of the servoing of a μUS probe in the large bowel using magnetic fields. The autonomous servoing algorithm, EFA, developed in this work uses

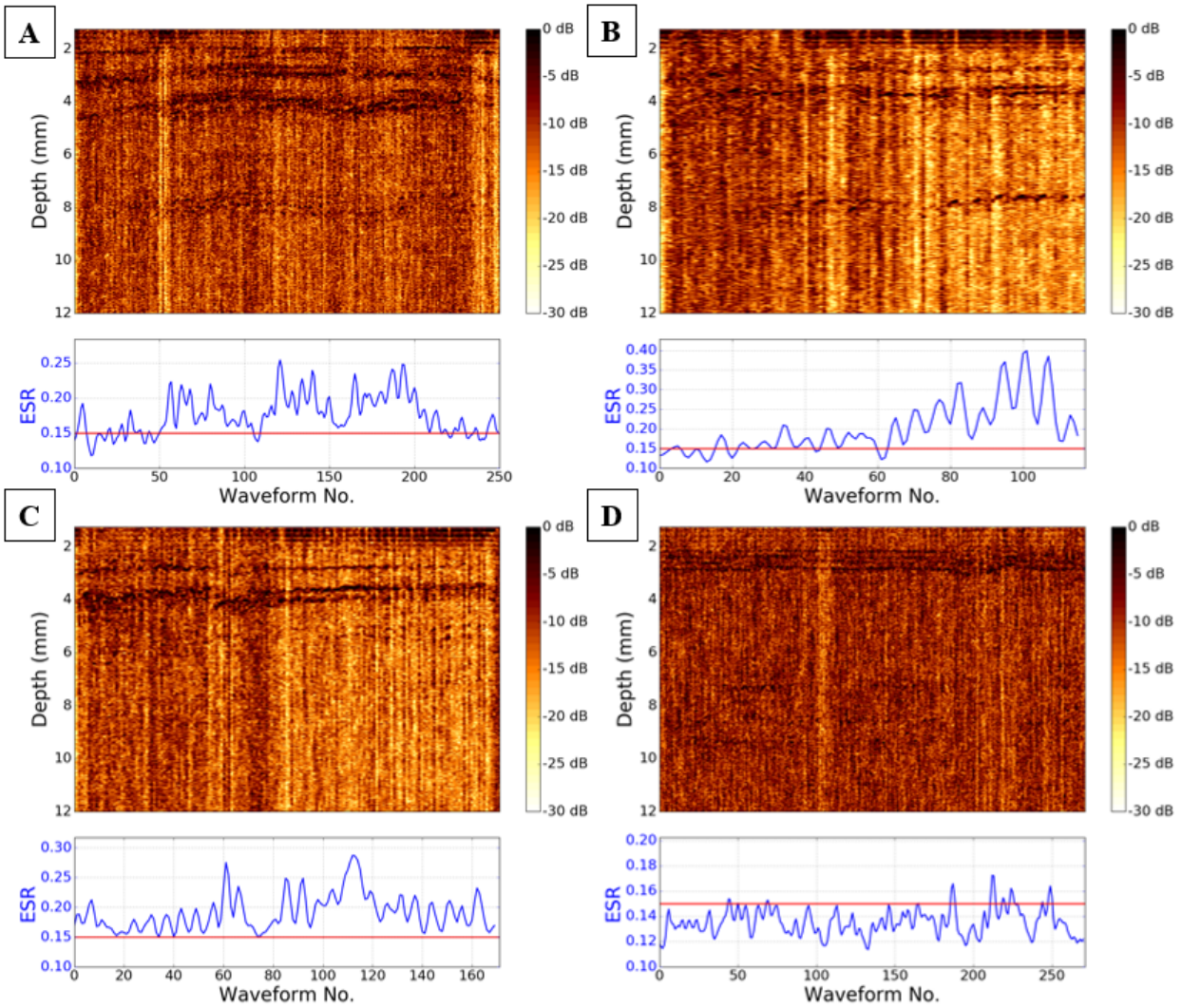

Figure 4.9: B-scans from four of the five *in vivo* autonomous servoing trials. Echoes are visible in each of these images. The ESR is clearly above ESR_{thresh} in (A)-(C). Although the ESR in (D) is below ESR_{thresh} (for most of the trial), echoes are still visible. This suggests that the ESR is not a perfect metric and image quality still needs to be interpreted by an operator; however, the proposed method gives the system an incentive to improve image quality, which facilitates the efficacy of this autonomous servoing.

magnetic forces and torques to search for an acceptable μUS signal strength. This enables an operator to approach a desired location in the lumen via magnetic device guidance and obtain an image by simply activating the EFA via, e.g., pushing a button. This work also involved the validation of the EFA when used in translation (TEFA). The system was capable of detecting all large (10 mm wide) landmarks and 66.7% of smaller (3 mm wide) landmarks. The overall distance

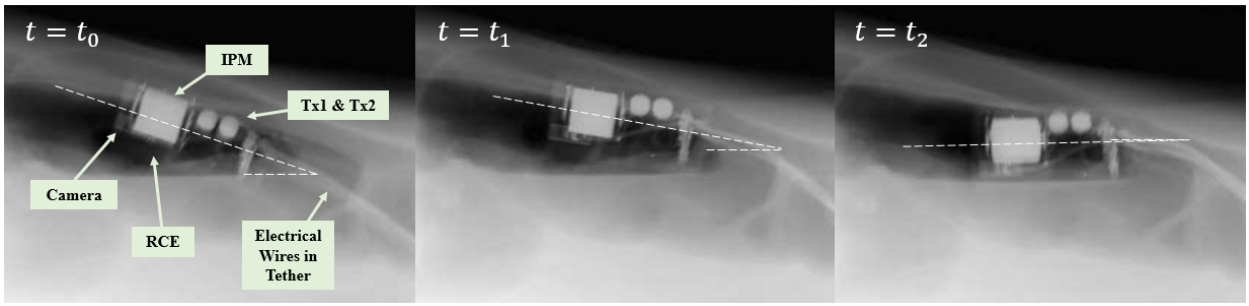

Figure 4.10: Images of the RCE *in vivo* captured using a C-Arm. Here, the RCE is tilted between frames, with tilt angle emphasized with broken lines.

measurement accuracy was 1.0±0.9 mm. These results suggest promise for future autonomous characterization and scanning of tissue using US. This work has been the first demonstration of (1) US servoing using magnetic link, (2) *in vivo* US servoing of a device that is not controlled from the outside of a patient via rigid-link, and (3) obtaining distance measurements of the environment using US imaging with magnetic actuation. This technology could one day be used for targeted, early diagnosis of diseases anywhere in the GI tract.

The custom acoustic coupling metric, the ESR, is effective at indicating a visible presence of echoes as observed in B-scans. The CL operation of the system with respect to US provides an additional sensing metric that informs the RCE of the environment. Without the use of the ESR, or another US-rating metric, US servoing would not be possible. The servoing methods used in this work are well suited for the unknown, unstructured, and dynamic environment of the bowel. This work was subject to a number of limitations, namely: (1) the RCE does not have roll-control capability, (2) a single 1D μUS transducer was used, (3) the data acquisition rate from an oscilloscope was a maximum of 3 Hz. It has been shown that magnetic control can be extended to all axes when manipulating the distribution of dipole elements in an actuated device [71], however, this comes with an increase in system complexity and a potential cost of implementation. In future work, radial arrays will likely be used that surround the RCE such that roll-control may not be critical, and image robustness may improve owing to the acquisition of a 2D scan. The ESR method used in this work can be extended to rate a 2D image. Finally, the data acquisition limitation in this

work was that of hardware. A dedicated field programmable gate array can be used to implement a analog-to-digital converter that operates at a higher frequency. A higher acquisition rate may enable image optimization; i.e. use the gradient of ESR to maximize image quality.

A potential future method for enhancing this work is the use of an ESR metric that incorporates tissue information. The current ESR method is amplitude-based and thus does not discriminate between a clear image of tissue or droplet of ultrasonic gel on the transducer. With the acquisition of more μUS tissue images, machine learning techniques may be used to determine the presence of clinically-relevant information.

Chapter 5

Force Control in the Presence of Magnetic-Robot Pose Uncertainties

The navigation of magnetic medical robots typically relies on localizing an actuated, intracorporeal, ferromagnetic body and back-computing a necessary field and gradient that would result in a desired wrench on the device. Uncertainty in this localization degrades the precision of force transmission. Reducing applied force uncertainty may enhance tasks such as *in-vivo* navigation of miniature robots, actuation of magnetically guided catheters, tissue palpation, as well as simply ensuring a bound on forces applied on sensitive tissue. This work contains an analysis of the effects of localization noise on force uncertainty, which is conducted by using sensitivity ellipsoids of the magnetic force Jacobian. Sensitivity ellipsoids were used to develop an uncertainty-reducing control algorithm. This algorithm was validated in both a simulation study and in a physical experiment. In simulation, the algorithm reduced force uncertainty by factors of up to 2.8 and 3.1 when using one and two actuating magnets, respectively. On a physical platform, the force uncertainty was reduced by a factor of up to 2.5 as measured using an external sensor. Being the first consideration of force uncertainty resulting from noisy localization, this work provides a strategy for investigators to minimize uncertainty in magnetic force transmission. Work related to this chapter resulted in the following publication: Ref. [4] (*Slawinski P.R., Simaan N.S., Taddese A.Z., Obstein K.L., Valdastri P., Sensitivity Ellipsoids for Force Control of Magnetic Robots with Localization Uncertainty, IEEE Transactions on Robotics, 06/2019*).

5.1 Motivation and Background

The control of magnetic devices is implemented by imparting a field misalignment and a gradient on the driven magnet, which induces a wrench. To apply a known wrench and thus to control a device, a knowledge or estimate of the actuated magnet's position and heading is essential. Meth-

ods that have been used and-or studied for obtaining feedback of the position, and-or orientation, of devices include: (1) visual feedback [33] (2) microwave imaging [143] (3) radio-frequency localization [144] (4) ultrasound [145] (5) positron emission tomography [146] and (6) magnetic localization [83, 147, 148, 53].

The work in this chapter is motivated by the lack of prior investigation into the effects of localization uncertainty on magnetic force transmission. Regardless of the localization method used, location uncertainty, or noise, introduces a disturbance in the applied magnetic wrench and thus negatively effects position and force control accuracy and robustness. Similar uncertainty effects have been extensively investigated in mechanical linkage architectures, but little consideration exists in the realm of magnetic actuation [149, 150, 151]. Localization uncertainty, as it pertains to the task of magnetic force transmission, has not been investigated. Furthermore, a framework for considering such uncertainty has not been developed.

A prior study concerning uncertainty in a magnetic actuation was conducted on a system consisting of a single permanent magnet that rotated to generate a rotating magnetic field. To avoid unexpected behavior and loss of control of a rotating robot, the authors characterized the effects of error in the chosen applied field rotation axis, field magnitude, and instantaneous rotational velocity while attributing worst-case bounds [52]. The distinction between rotating and non-rotating is significant as the mechanics of actuation are different: a rotating robot is typically propelled via the mechanics of threading through a medium, while a non-rotating robot is simply subject to applied forces and torques and dynamically reacts to them.

The primary contributions of this work are (1) a method for characterizing the effects of localization noise on uncertainty in the applied magnetic force on an actuated intracorporeal magnet and (2) the application of this characterization to a force control task where one desires to reduce force uncertainty in a chosen direction. Sensitivity ellipsoids [69] are utilized to characterize the mapping between localization noise and the uncertainty in applied force on an actuated magnet. Force sensitivity ellipsoids have been utilized for analysis of rigid-link robots; however, magnetic ellipsoids are unique in that a duality between joint and force manipulability does not exist. In

the case of magnetic robots, the force and "joint" value are inherently coupled as force results in the actuation of magnetic robots. This work demonstrates that actuation redundancy in a magnetic system can be utilized to adjust the shape of force sensitivity ellipsoids that, in turn, results in a force control that has a lower force uncertainty in a direction of choice. This methodology is valid for magnetic actuation systems with one or more external actuation magnets. The approach presented in this chapter can be easily expanded for systems of electromagnets by replacing EM twist relations with current inputs, or combining the two in the case of mobile electromagnet systems [43].

5.2 Modelling of Magnetic Force Uncertainty

5.2.1 Assumptions

Five assumptions are made in this work that relate to the magnetic field, the motion of the actuated IM, and the localization of the actuating EM: (1) magnets can be modelled as ideal dipoles; this is an appropriate approximation as a permanent magnet with identical length and diameter, as used in this system, has been shown to resemble a dipole field with approximately 1% error at one normalized distance from the EM's center (10 cm in this case) [63]. (2) IM moves slowly, which simplifies the mathematical formulations. This assumption has been used in prior chapters. (3) the configuration of the EM is assumed to be known and ideal, i.e. without uncertainty. In this work, the EM is fixed at the end-effector of a serial industrial manipulator and the configuration of the EM is computing using direct kinematics. The assumption of ideal EM configuration knowledge is valid as the kinematics of the rigid-link manipulator are likely to have a significantly higher accuracy than magnetic localization systems. (4) the magnetic Jacobian is a sufficient local representation of nonlinear behaviors. This assumption is discussed in a latter portion of this section; however, it is a safe assumption as the applied controller runs at over 50 Hz. (5) the Jacobian used for magnetic actuation is not affected by localization noise.

Table 5.1: Nomenclature (©2019 IEEE [4])

Symbol	Description
$\mathbf{v}$	Vector (lowercase, bold)
$\mathbf{M}$	Matrix (uppercase)
$\mathbf{I}$	Identity matrix
$\mathbf{J}$	Jacobian matrix
$\tilde{\mathbf{J}}$	Jacobian matrix written in terms of differential rotation
δ	Infinitesimal change
$\hat{\mathbf{v}}$	Unit vector
$\mathbf{p}_{e_k}$	Position of kth EM in inertial frame $\in \mathbf{R}^3$
$\mathbf{p}_i$	Position of IM in inertial frame $\in \mathbf{R}^3$
$\mathbf{p}_k = \mathbf{p}_i - \mathbf{p}_{e_k}$	Relative position vector from kth EM to IM $\in \mathbf{R}^3$
$\hat{\mathbf{m}}_{e_k}$	Magnetic moment vector of kth EM $\in \mathbf{R}^3$
$\hat{\mathbf{m}}_i$	Magnetic moment vector of IM $\in \mathbf{R}^3$
$\mathbf{x}_e = [\mathbf{p}_e; \hat{\mathbf{m}}_e]$	Pose of EM $\in \mathbf{R}^6$
$\mathbf{x}_i = [\mathbf{p}_i; \hat{\mathbf{m}}_i]$	Pose of IM $\in \mathbf{R}^6$
$\mathbf{x}_d = [\mathbf{p}_d; \hat{\mathbf{m}}_d]$	IM pose disturbance from localization uncertainty $\in \mathbf{R}^6$

5.2.2 Error Propagation in Magnetic Coupling

The dipole model describes the field of a particle and can be used to approximate the fields of permanent magnets of various shape [63]. The model is summarized in this section for the purpose of understanding control relations, and present linearizations that are used in sensitivity analysis and control. The expressions in this chapter are extended to allow for the use of multiple EMs hence some relations are nearly repeated from previous chapters.

The discussion, methodology, and experiments in this chapter serve as a case study for the proposed approach to sensitivity analysis and optimization. The methodology is presented for a system of one or more EMs that actuate, via imparted wrenches, a single IM. The gradient and direction of the magnetic field at the IM is controlled by imparting twists on the EM(s). Magnet

references are distinguished by using an “e” or “E” subscript to reference EMs and an“i” or “I” subscript to refer to the IM. In the event that multiple EMs are used, an additional enumeration subscript “k” is applied. The nomenclature used in this document is shown in Table 5.1, with some parameters visualized in Fig. 1.2 where a planar dipole field shape is shown for reference.

The magnetic field of a single EM applied at an IM can be expressed via Eq. (5.1) whereas, owing to magnetic fields being vector fields, the total field at an IM can be expressed via Eq. (5.2) [62].

$$\mathbf{b}_{e_k}(\mathbf{p}_k) = \frac{\mu_0}{4\pi \left\|\mathbf{p}_k\right\|^3}(3\hat{\mathbf{p}}_k\hat{\mathbf{p}}_k^{\mathrm{T}}\mathbf{m}_{e_k} - \mathbf{m}_{e_k}) \tag{5.1}$$

$$\mathbf{b}_e = \sum_{j=1}^{n} \mathbf{b}_{e_j}(\mathbf{p}_j) \tag{5.2}$$

The magnetic wrench induced on the IM by external fields can be expressed via Eq. (5.3) and Eq. (5.4) [44].

$$\begin{aligned}\mathbf{f} = (\mathbf{m}_i \cdot \nabla)\mathbf{b}_e = \sum_{i=j}^{n} \Big(&\frac{3\mu_0 \left\|\mathbf{m}_{e_j}\right\| \left\|\mathbf{m}_i\right\|}{4\pi \left\|\mathbf{p}_j\right\|^4}(\hat{\mathbf{m}}_{e_j}\hat{\mathbf{m}}_i^{\mathrm{T}} \\ &+\hat{\mathbf{m}}_i\mathbf{m}_{e_j}^{\mathrm{T}} + (\hat{\mathbf{m}}_i^{\mathrm{T}}(\mathbf{I} - 5\hat{\mathbf{p}}_j\hat{\mathbf{p}}_j^{\mathrm{T}})\hat{\mathbf{m}}_{e_j})\mathbf{I})\Big)\hat{\mathbf{p}}\end{aligned} \tag{5.3}$$

$$\begin{aligned}\tau &= \mathbf{m_i} \times \mathbf{b}_e \\ &= \sum_{j=1}^{n} \Big(\frac{\mu_0 \left\|\mathbf{m}_{e_j}\right\| \left\|\mathbf{m}_i\right\|}{4\pi \left\|\mathbf{p}_j\right\|^3}\hat{\mathbf{m}}_i \times (3\hat{\mathbf{p}}_j\hat{\mathbf{p}}_j^{\mathrm{T}} - \mathbf{I})\hat{\mathbf{m}}_{e_j}\Big)\end{aligned} \tag{5.4}$$

The linearization that relates infinitesimal EM motion and the change in wrench, $\delta\mathbf{w}$, applied on the IM can be evaluated either numerically or analytically. An analytical formulation of Jacobians that relates the motion of a single EM to changes in magnetic force on the IM and heading of the IM have been developed by Mahoney and Abbott [44] and later expanded by Taddese et al. [1] to include consideration for magnetic torque in cases where alignment of the IM to the external field should not be assumed. This expression is shown in Eq. (5.5). The EM and IM terms are separated in Eq. (5.6), and expand the expression for cases of actuation via multiple EMs in Eq. (5.7). Explicit

definitions of differential terms can be found in [1].

$$\delta \mathbf{w}_k = \begin{bmatrix} \delta \mathbf{f}_k \\ \delta \tau_k \end{bmatrix} = \begin{bmatrix} \frac{\partial \mathbf{f}_k}{\partial \mathbf{p}_k} & \frac{\partial \mathbf{f}_k}{\partial \hat{\mathbf{m}}_{e_k}} & \frac{\partial \mathbf{f}_k}{\partial \hat{\mathbf{m}}_i} \\ \frac{\partial \tau_k}{\partial \mathbf{p}_k} & \frac{\partial \tau_k}{\partial \hat{\mathbf{m}}_{e_k}} & \frac{\partial \tau_k}{\partial \hat{\mathbf{m}}_i} \end{bmatrix} \begin{bmatrix} \delta \mathbf{p}_k \\ \delta \hat{\mathbf{m}}_{e_k} \\ \delta \hat{\mathbf{m}}_i \end{bmatrix} \tag{5.5}$$

$$\begin{aligned} \begin{bmatrix} \delta \mathbf{f}_k \\ \delta \tau_k \end{bmatrix} &= \begin{bmatrix} \frac{\partial \mathbf{f}_k}{\partial \mathbf{p}_{e_k}} & \frac{\partial \mathbf{f}_k}{\partial \hat{\mathbf{m}}_{e_k}} \\ \frac{\partial \tau_k}{\partial \mathbf{p}_{e_k}} & \frac{\partial \tau_k}{\partial \hat{\mathbf{m}}_{e_k}} \end{bmatrix} \begin{bmatrix} \delta \mathbf{p}_{e_k} \\ \delta \hat{\mathbf{m}}_{e_k} \end{bmatrix} + \begin{bmatrix} \frac{\partial \mathbf{f}_k}{\partial \mathbf{p}_i} & \frac{\partial \mathbf{f}_k}{\partial \hat{\mathbf{m}}_i} \\ \frac{\partial \tau_k}{\partial \mathbf{p}_i} & \frac{\partial \tau_k}{\partial \hat{\mathbf{m}}_i} \end{bmatrix} \begin{bmatrix} \delta \mathbf{p}_i \\ \delta \hat{\mathbf{m}}_i \end{bmatrix} \\ &= \mathbf{J}_{e_k} \begin{bmatrix} \delta \mathbf{p}_{e_k} \\ \delta \hat{\mathbf{m}}_{e_k} \end{bmatrix} + \begin{bmatrix} \frac{\partial \mathbf{f}_k}{\partial \mathbf{p}_i} & \frac{\partial \mathbf{f}_k}{\partial \hat{\mathbf{m}}_i} \\ \frac{\partial \tau_k}{\partial \mathbf{p}_i} & \frac{\partial \tau_k}{\partial \hat{\mathbf{m}}_i} \end{bmatrix} \begin{bmatrix} \mathbf{I} & \mathbf{0} \\ \mathbf{0} & \mathbf{S}(\hat{\mathbf{m}}_i)^{\mathrm{T}} \end{bmatrix} \begin{bmatrix} \delta \mathbf{p}_i \\ \omega_i \end{bmatrix} \\ &= \mathbf{J}_{e_k} \begin{bmatrix} \delta \mathbf{p}_{e_k} \\ \delta \hat{\mathbf{m}}_{e_k} \end{bmatrix} + \begin{bmatrix} \mathbf{J}_{Fp_i} & \tilde{\mathbf{J}}_{F\omega_i} \\ \mathbf{J}_{Tp_i} & \tilde{\mathbf{J}}_{T\omega_i} \end{bmatrix} \begin{bmatrix} \delta \mathbf{p}_i \\ \omega_i \end{bmatrix} \\ &= \mathbf{J}_{e_k} \begin{bmatrix} \delta \mathbf{p}_{e_k} \\ \delta \hat{\mathbf{m}}_{e_k} \end{bmatrix} + \tilde{\mathbf{J}}_{i_k} \begin{bmatrix} \delta \mathbf{p}_i \\ \omega_i \end{bmatrix} \end{aligned} \tag{5.6}$$

Here, $S(\mathbf{a}) \in so(3)$ denotes the skew-symmetric form of the cross-product operation. In $\tilde{\mathbf{J}}_i$ of Eq. (5.6), partial derivatives with respect to differential rotation (ω_i) are used, rather than dipole heading, as angular velocity is the mode of localization feedback. In Eq. (5.7), Eq. (5.6) is ex-

panded to account for multiple EMs used for actuation.

$$
\begin{aligned}
\delta\mathbf{w} &= \delta\mathbf{w}_e + \delta\mathbf{w}_i \\
\begin{bmatrix} \delta\mathbf{f} \\ \delta\tau \end{bmatrix} &= \mathbf{J}_e \begin{bmatrix} \delta\mathbf{p}_e \\ \delta\hat{\mathbf{m}}_e \end{bmatrix} + \tilde{\mathbf{J}}_i \begin{bmatrix} \delta\mathbf{p}_i \\ \omega_i \end{bmatrix} \\
\delta\mathbf{w} &= \begin{bmatrix} \mathbf{J}_{Fe} \\ \mathbf{J}_{Te} \end{bmatrix} \delta\mathbf{x}_e + \begin{bmatrix} \tilde{\mathbf{J}}_{Fi} \\ \tilde{\mathbf{J}}_{Ti} \end{bmatrix} \begin{bmatrix} \delta\mathbf{p}_i \\ \omega_i \end{bmatrix} \\
&= \begin{bmatrix} \mathbf{J}_{Fe_1} & \dots & \mathbf{J}_{Fe_k} \\ \mathbf{J}_{Te_1} & \dots & \mathbf{J}_{Te_k} \end{bmatrix} [\delta\mathbf{x}_{e_1}; \dots; \delta\mathbf{x}_{e_k}]^{\mathrm{T}} + \\
&\dots \Big(\sum_{i=1}^{n} \begin{bmatrix} \tilde{\mathbf{J}}_{Fi_k} \\ \tilde{\mathbf{J}}_{Ti_k} \end{bmatrix} \Big) \begin{bmatrix} \delta\mathbf{p}_i \\ \omega_i \end{bmatrix}
\end{aligned}
\tag{5.7}
$$

The full expression for applied wrench, $\delta\mathbf{w}$, is shown in Eq. (5.7). This expression can be interpreted as: the infinitesimal change in wrench applied on the IM by the EM(s) results from the change in pose of the EM(s) and IM. It should be noted that the influences of Jacobians $\mathbf{J}_{Fe_k}$ and $\tilde{\mathbf{J}}_{Fi}$ are nearly identical if a single EM is used. The relative impact of $\tilde{\mathbf{J}}_{Fi}$ decreases as more EMs are used and has approximately 60% of the influence of $\mathbf{J}_{Fe_k}$ when two EMs are used. As $\delta\mathbf{w}_i$ is null owing to an assumption of slow IM motion, it is replaced with an algorithmic wrench disturbance term to account for the effects of localization uncertainty in a force application task. This new term can be interpreted as a numerical uncertainty in wrench that does not exist in the physical world, but is perceived by the controller. With this disturbance wrench, the expression for the change in applied wrench becomes $\delta\mathbf{w} = \delta\mathbf{w}_e + \delta\mathbf{w}_d$. The term $\delta\mathbf{w}_d$ is modelled the same way as $\delta\mathbf{w}_i$ i.e. the Jacobian $\tilde{\mathbf{J}}_i$ is used to compute it via multiplication by the disturbance twist $\delta\mathbf{x}_d$. Hereafter, $\mathbf{J}_e \in \mathbf{R}^{6\times 6k}$ is used for actuation and $\tilde{\mathbf{J}}_i \in \mathbf{R}^{6\times 6}$ is used for analyzing the mapping of localization noise to a disturbance wrench. Whereas ideal knowledge of EM positioning is assumed here, Eq. (5.7) should be augmented in the event that a larger uncertainty exists in the configuration of the EM.

The expression in Eq. (5.7) remains valid as long as the linearity assumption holds; i.e. linear and angular perturbations of IM pose are small enough. To evaluate an approximate linearity range, a numerical simulation was conducted using 90,000 configurations of an IM and EM, where the IM was spanned to be between 14 and 16 cm from the EM, and found the linearity range to be 14.3 mm and 6.1°. The conditions for linearity in magnetic force were as follows: the error magnitude of the linearized force less than or equal to 10%, and the direction error between the linearized force and nonlinear truth is less than or equal to 10°. It should be noted that the aforementioned angular range of 6.1° refers to rotation of the IM, while the angular error of linearized force refers to an angle between resultant force vectors. Furthermore, an assumption is made that $\mathbf{J}_{Fe_k}$ is not affected by localization noise. The implication of this noise is a deviation of commanded magnet motion from the optimal, i.e. the direction that reduces force error. This assumption degrades as the rate of control decreases and the resultant effect is a non-smooth motion of the EM(s).

5.2.3 Analysis of Force Uncertainty Using Sensitivity Ellipsoids

To characterize the effect of localization uncertainty, the Jacobian $\tilde{\mathbf{J}}_i$—a linear mapping between infinitesimal changes in IM pose and uncertainty in applied wrench—is analyzed. An instantaneous visualization of the Jacobian mapping, a sensitivity ellipsoid, has been frequently used in rigid-link robotics for considering losses in degrees-of-freedom (DoFs), kinematic and dynamic manipulability, and sensitivity, but has not before been utilized in magnetic control. Derivations of ellipsoids and their usage is analyzed in texts by Yoshikawa and Nakamura [69, 70] as they will be omitted here for brevity apart from relations that are necessary for understanding the topic at hand. The force uncertainty that results from localization noise is dictated by $\tilde{\mathbf{J}}_{Fi}$ which maps infinitesimal IM twist to a change in force applied on the IM.

The mapping of $\tilde{\mathbf{J}}_{Fi}$ can be visualized by considering a set of unit inputs of $\delta\mathbf{x}_d$ uniformly distributed such as to resemble a unit sphere. The set of mapped force vectors is defined by the hyper-ellipsoid:

$$\delta\mathbf{f}_d^{\mathrm{T}}(\tilde{\mathbf{J}}_{Fi}\tilde{\mathbf{J}}_{Fi}^{\mathrm{T}})^{-1}\delta\mathbf{f}_d = 1 \tag{5.8}$$

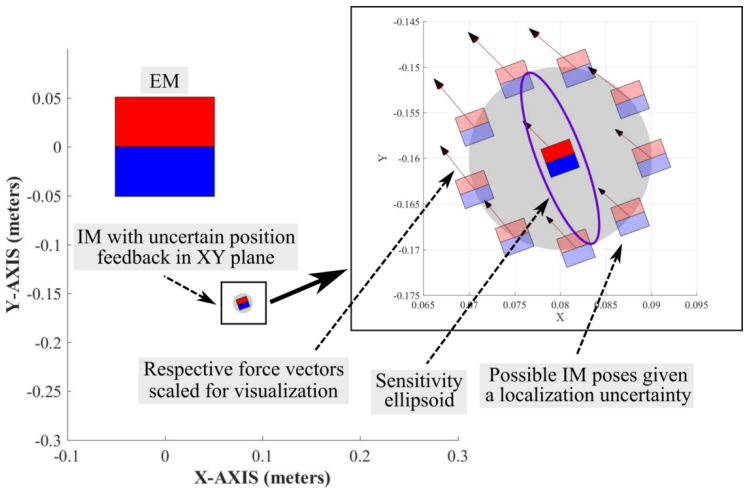

Figure 5.1: Graphical representation of a single EM that actuates an IM, possible uncertain poses of the IM when zoomed in, and the sensitivity ellipsoid that relates position uncertainty with uncertainty in applied force. Both force and motion are considered only in the XY plane for visualization. (©2019 IEEE [4])

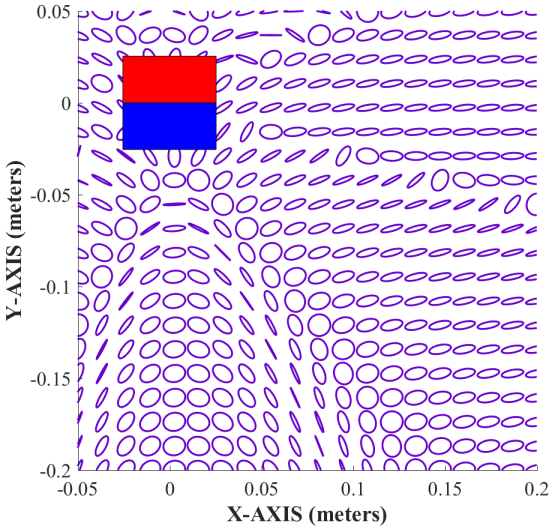

Figure 5.2: A planar representation of shape variation of the $\partial \mathbf{f}/\partial \mathbf{p}_i$ Jacobian sensitivity ellipsoid. The IM orientation is kept constant while it is translated throughout this planar workspace in a set of discrete points where the ellipsoids are shown. All ellipsoids are normalized in scale for visualization. (©2019 IEEE [4])

The major and minor axes of this hyper-ellipsoid constitute the directions of maximum and minimum wrench uncertainty, respectively. The mapping can be explicitly characterized using singular value decomposition. The Jacobian $\tilde{\mathbf{J}}_{Fi}$ can be decomposed into $\mathbf{U}\Sigma\mathbf{V}^{\mathrm{T}}$ where $\mathbf{U}$ and $\mathbf{V}$ are two

orthonormal spaces where the columns of $\mathbf{U}$ are called left-singular vectors and the columns of $\mathbf{V}$ are called right-singular vectors. The diagonal of $\mathbf{\Sigma}$ contains the singular values, s_i, of $\tilde{\mathbf{J}}_{Fi}$ which are arranged such that $s_1 > s_2 > s_3$. Conceptually, the left-singular vectors indicate the principal directions of infinitesimal wrench application whereas the right-singular vectors indicate the corresponding directions of infinitesimal twists that cause the respective wrenches. Thus, the longer that a sensitivity ellipsoid is in a particular direction, the more uncertain the applied wrench is.

In a force control task, this ellipsoid is desired to be as small as possible in the direction that force is to be controlled with the most certainty. A 2D conceptual representation of a sensitivity ellipsoid, developed via the dipole model, is shown in Fig. 5.1. The shape of the ellipsoids may vary significantly throughout an EM's workspace as demonstrated in Fig. 5.2; here, a constant orientation of an IM is chosen and the dipole ellipsoids are plotted at a discrete set of IM positions on a plane. As the accuracy of the dipole model of the EM increases with distance, so does the accuracy of the sensitivity ellipsoids.

The control task is to reduce uncertainty in a force application task, such as applying a contact force, in a direction of interest that will hereafter be refer to as $\hat{\mathbf{c}}$, where "c" denotes "contact". This inherently results in a desired task of reducing the spatial derivative of force in the direction of contact. The size of the mapping of Jacobian $\tilde{\mathbf{J}}_{Fi}$ in the direction of $\hat{\mathbf{c}}$ may be used to interpret force uncertainty. To obtain this size, the volume of the sensitivity ellipsoid of $\tilde{\mathbf{J}}_{Fi}$ is projected in the direction of $\hat{\mathbf{c}}$ via projection matrix $\mathbf{P}_c = \hat{\mathbf{c}}\hat{\mathbf{c}}^{\mathrm{T}}$, and the volume is computed. The ellipsoid length of $\tilde{\mathbf{J}}_{Fi}$ in the direction of $\hat{\mathbf{c}}$ is hereafter referred to via the scalar g. The definition of g is shown in Eq. (5.9) whereas the expression for computing the volume of a hyper-ellipsoid, as defined in [70], is shown in Eq. (5.10) where $\Gamma(\star)$ is the gamma function and m is the length of the hyper-ellipsoid. The *vol() function of Eq. (5.10) computes the product of non-zero singular values; this facilitates not only the computation of volume, but also area, or length, in the case of the Jacobian being rank deficient.* The magnetic force for which the unceratinty is desired to be minimized is referred to as $f_c = \mathbf{f} \cdot \hat{\mathbf{c}}$ where the subscript "c" indicates "contact force". The force f_c is one that is exerted on

the environment by the IM. The parameters of a sensitivity ellipsoid are visualized in Fig. 5.3.

$$g \equiv vol(\mathbf{P}_c \tilde{\mathbf{J}}_{Fi}) \tag{5.9}$$

$$vol(\mathbf{J}) = \frac{\pi^{m/2}}{\Gamma(1+m/2)} \prod_{i=1}^{j} \sigma_i \tag{5.10}$$

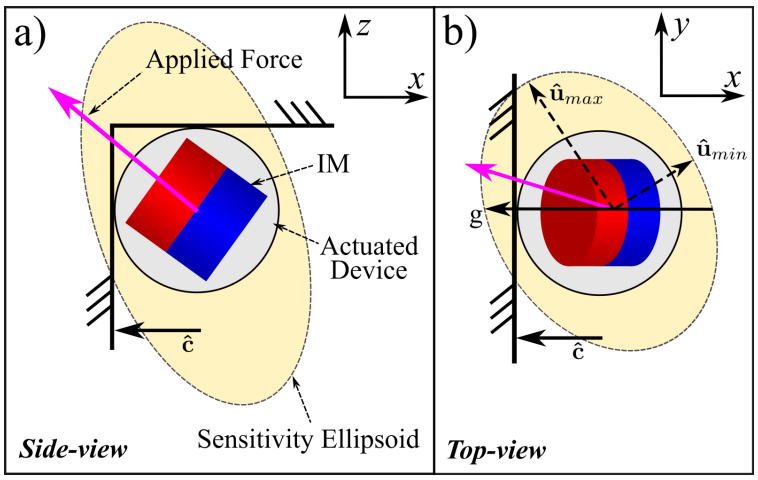

Figure 5.3: Conceptual schematic of a force sensitivity ellipsoid. The ellipsoid view represents a plane-cut through the ellipsoid, which would be achieved by projecting a Jacobian. Sub-figure a) shows a side view of ellipsoid, whereas sub-figure b) shows the top view of ellipsoid. The top view contains the ellipsoidal projection where g takes on a value between the magnitudes of the ellipsoid length in the $\hat{\mathbf{u}}_{min}$ and $\hat{\mathbf{u}}_{max}$ direction. (©2019 IEEE [4])

Localization feedback with noise will result in an uncertain estimated force as mapped by the nonlinear equation Eq. (5.3). This mapped wrench is hereafter referred to as f_{c_a} where the subscript "a" is used to denote that this is the contact force as interpreted by an algorithm. It should be noted that the difference between f_c and f_{c_a} is that f_c is a true force that is exerted on the environment, whereas f_{c_a} is the force as perceived by a control algorithm. The value of f_c can be more precisely controlled when the uncertainty of f_{c_a} is minimized. The force uncertainty is quantified using coefficients of variation CV_a and CV_t which represent the algorithmic contact force uncertainty, Eq. (5.11), and the true contact force uncertainty, Eq. (5.12), respectively. Here, *STD* indicates the

standard deviation.

$$CV_a = 100 \times |\frac{STD(f_{c_a})}{MEAN(f_{c_a})}| \tag{5.11}$$

$$CV_t = 100 \times |\frac{STD(f_c)}{MEAN(f_c)}| \tag{5.12}$$

To visualize the relationship between these values in the presence of localization noise, a set of 5000 numerical simulationsw as conducted where a uniform localization noise of 15 mm and 15° was applied with a single stationary EM and a stationary IM. This linear noise translates to approximately 135% of the size (11.11 mm diameter and length) of the IM used in the experimental work discussed in prior STORM lab publications [3, 53] as well as earlier in this dissertation. In each of the 5000 simulations, the EM's pose was randomly chosen within a distance between magnets of 15 cm with a STD of 1 cm, or in a bound of approximately 7% of the separating distance. The position of the EM around the IM was chosen by a uniform random distribution of relative position vectors $\mathbf{p}$. Similarly, the heading of the EM was chosen randomly as well. For each pose of the EM, 1000 mappings from uncertain localization to f_{c_a} were computed. Noise was assumed to have a Gaussian distribution. A nonlinear force mapping was applied here.

The relationships between g and the STD of $|f_{c_a}|$ were computed, Fig. 5.4, as well as between $mean(g)/mean(|f_{c_a}|)$ and CV_a, Fig. 5.5. It should be noted that $mean(g)/mean(|f_{c_a}|)$ is not equal to $mean(g/|f_{c_a}|)$. The relationship between g and CV_a is not directly plotted as the latter is normalized with the contact force magnitude. The value g and the STD of $|f_{c_a}|$ are related linearly with a coefficient of determination of 0.94, whereas the relation between $g/|f_{c_a}|$ and CV_a has a coefficient of determination of 0.87. As the results in Fig. 5.5 are normalized with force magnitude, a nonlinearity is introduced that results from the relation shown in Eq. (5.3). This analysis suggests that reducing g will result in a reduction in uncertainty.

The uncertainty of f_{c_a}, the contact force as estimated by the system, is directly affected by the value of g and thus, since g can be controlled by the actuating field, the uncertainty of f_{c_a} can also be controlled. The uncertainty in the true force on the environment, f_c, however, is dependent not only on the estimate f_{c_a}, but also on environmental factors, and thus cannot directly be controlled.

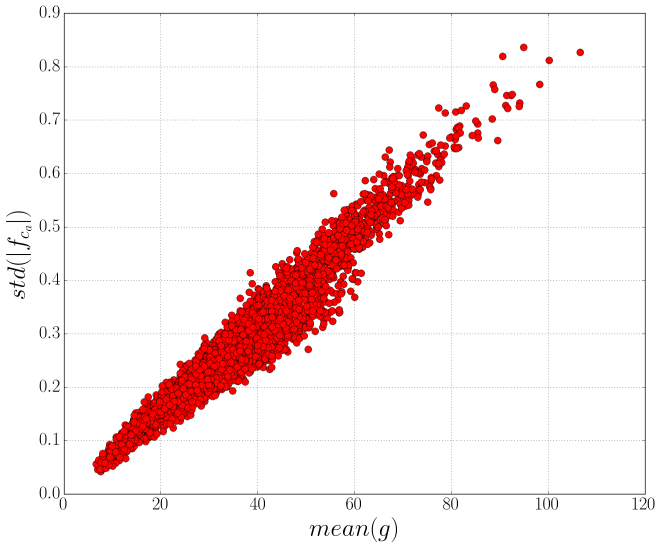

Figure 5.4: Numerical simulation result that shows the relationship between the STD of f_{c_a}, which is the contact force as estimated by the system, and the mean value of g. Here, the mean refers to the mean value of the 1000 data points of each of the 5000 simulation. (©2019 IEEE [4])

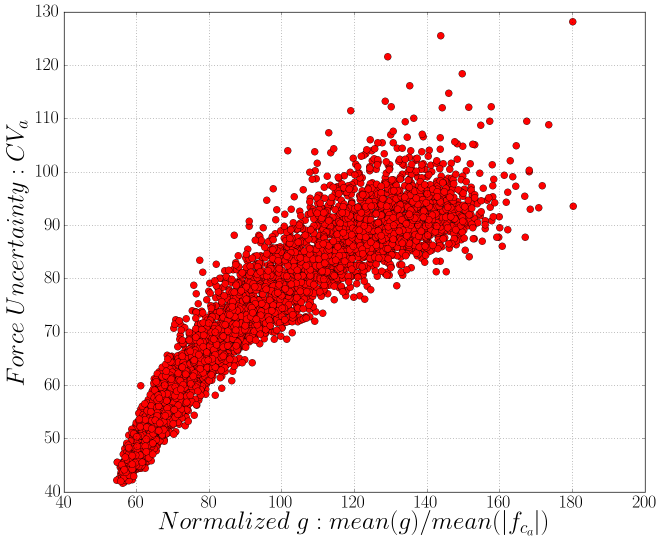

Figure 5.5: Numerical simulation result that shows the relationship between the mean normalized value of g and CV_a. Here, the mean refers to the mean value of the 1000 data points of each of the 5000 simulation. (©2019 IEEE [4])

It is assumed that if the estimated contact force has a lower uncertainty, then the true contact force will likely have a lower uncertainty as well.

5.3 Force Control

To implement magnetic control, the EM motions that will result in desired wrenches on the IM must be computed that, in turn, will act on the IM and result in desired force and-or motion. The motion of an IM is dictated by device mechanics and dynamics, as well as environmental interactions. Rather than precisely modeling environmental effects which may be cumbersome, prior works have successfully implemented CL control without environmental modelling [44, 3, 53] which has been done in this chapter as well. To choose a desired EM motion, a desired infinitesimal change in force must be determined, which is referred to as $\delta\mathbf{f}_{des}$. Given that this is a 3 DoF actuation task, and the actuation system has 5 DoFs, $\mathbf{J}_{Fe}$ contains 2 DoFs of redundancy, which is used here for sensitivity minimization.

The action of the controller is dependent on the method of inversion of the $\mathbf{J}_{Fe}$ Jacobian. One acceptable inversion method is to use a weighted right pseudo-inverse as shown in Eq. (5.13) [152]. This inversion is a constrained linear optimization that minimizes the objective function $\delta\mathbf{x}_e^{\mathrm{T}}\mathbf{W}\delta\mathbf{x}_e$ where $\mathbf{W}$ is a diagonal weight matrix whose diagonal weights can be chosen such that certain values of $\delta\mathbf{x}_e$ are minimized with preference. The weight matrix $\mathbf{W}$ can be used for performance tuning as the vector $\delta\mathbf{x}_e$ contains terms of various units; an example result of weight tuning could be a preference for EM rotation rather than translation. In implementations in this paper, $\mathbf{W}$ was set to an identity matrix.

$$\delta\mathbf{x}_e = \mathbf{W}^{-1}\mathbf{J}_{Fe}^{\mathrm{T}}(\mathbf{J}_{Fe}\mathbf{W}^{-1}\mathbf{J}_{Fe}^{\mathrm{T}})^{-1}\delta\mathbf{f}_{des} = \mathbf{J}_{Fe}^{\#}\delta\mathbf{f}_{des} \tag{5.13}$$

To reduce uncertainty in $\mathbf{f}_c$, the value of g must be reduced. A control method is proposed in this section that reduces the value of g using a gradient projection method [153] in magnetic control. The shape of the sensitivity ellipsoid is algorithmically altered using EM DoFs that are redundant, i.e. are not used for completing the desired task of 3 DoF force control. The control strategy of Eq. (5.13) is thus augmented to Eq. (5.14) where the scalar value β is a user defined constant that, when set to a negative value, projects the gradient onto the null space of $\mathbf{J}_{Fe}$ as

to minimize an objective function. The value of $\delta\mathbf{f}_{des}$ is task dependent and will be specified in reference to experiments later in this manuscript. The gradient of g is computed via Eq. (5.15) where a gradient with respect to a single EM motion is computed. This same method is utilized by stacking gradients if more than one EM is used. The gradient is computed numerically using Python; the computation time for which is between 2 and 4 ms when using a single EM. In this implementation, the gradient is normalized and the impact of the homogeneous solution is capped.

$$\begin{aligned}\delta\mathbf{x}_e &= \delta\mathbf{x}_{e_{particular}} + \delta\mathbf{x}_{e_{homogeneous}} = \delta\mathbf{x}_{e_p} + \delta\mathbf{x}_{e_h} \\ &= \mathbf{J}_{Fe}^{\#}\delta\mathbf{f}_{des} + \beta(\mathbf{I} - \mathbf{J}_{Fe}^{\#}\mathbf{J}_{Fe})\nabla_{\mathbf{x}_e} g(\mathbf{x}_e, \mathbf{x}_i)\end{aligned} \tag{5.14}$$

$$\nabla_{\mathbf{x}_e} g = \begin{bmatrix} \frac{\partial vol(\mathbf{P}_c\mathbf{J}_{Fi})}{\partial \mathbf{p}_e} \\ \frac{\partial vol(\mathbf{P}_c\mathbf{J}_{Fi})}{\partial \hat{\mathbf{m}}_e} \end{bmatrix} \tag{5.15}$$

5.4 Simulation and Platform Experimentation: Validation of Force Uncertainty Reducing Algorithm

5.4.1 Experimental Setup

Experiments were conducted in both a simulation environment and a physical platform, shown in Fig. 5.6 and Fig. 5.7, respectively. The physical platform is that of the MFE system. All system software was written using Python and Robotic Operating System middleware [74]. The simulation was developed in Gazebo, an open-source software that is equipped with a physics engine, and component-wise emulates the physical platform. A custom magnetic dipole plugin that was previously developed by Dr. Taddese was used [1] for integrating magnetic wrenches with Gazebo's dynamics. The IM in the simulation is housed in a spherical shell. The shape is chosen to minimize effects of geometry on algorithm function. The IM's shell contains a tether whose primary purpose is to stabilize dynamics of the IM; however, an additional advantage of the tether is that it acts as a disturbance to IM motion that is likely to be more realistic than a simple untethered sphere.

A force and torque sensor (Nano 17 SI-25-0.25, ATI Technologies) was used in force-control validation experiments. Data from this sensor was acquired using a 12 bit Analog-to-Digital converter that provided accuracy of 0.1 N and 0.5 $m \cdot Nm$. This sensor was mounted on, and manipulated by, a second serial manipulator (RV6SDL, Mitsubishi, Inc., Japan). The two manipulators were registered using a least-squares fitting [154].

The magnetic control solution to Eq. (5.14) is an EM motion, thus joint values of the serial manipulator must be computed to achieve the desired end-effector motion. To compute the necessary robot joint step, $\delta\mathbf{q}$ to achieve $\delta\mathbf{x}_e$, an actuation Jacobian, $\mathbf{J}_A$, is used, as defined in Eq. (5.16), where $\mathbf{J}_R$ is the manipulator's geometric Jacobian. The Jacobian $\mathbf{J}_A$ contains a well known redundancy in that a dipole can rotate about about its magnetization axis without change in applied field owing to its field symmetry about its magnetization axis.

$$\delta\mathbf{x}_e = \begin{bmatrix} \mathbf{I} & \mathbf{0} \\ \mathbf{0} & \mathbf{S}(\hat{\mathbf{m}}_e)^{\mathrm{T}} \end{bmatrix} \mathbf{J}_R \delta\mathbf{q} = \mathbf{J}_A \delta\mathbf{q} \tag{5.16}$$

The robot joint solution is shown in Eq. (5.17) where $\mathbf{J}_A^+$ denotes the *Moore-Penrose Pseudo Inverse* of the actuator Jacobian. Similar to β in Eq. (5.14), β_R is a user defined value that scales the projection of the gradient of an objective function, $h(\mathbf{q})$, onto the null space of $\mathbf{J}_R$. The value of $h(\mathbf{q})$ was chosen as such that represents the value of the manipulator's wrist, thus, after a threshold is reached, the manipulator uses available redundancy to prevent a collision between the casing of the EM and the manipulator's link. The strategy is particular to this application and can be customized per future operator's needs.

$$\delta\mathbf{q} = \mathbf{J}_R^+ \delta\mathbf{x}_e + \beta_R(\mathbf{I} - \mathbf{J}_R^+ \mathbf{J}_R)\nabla_{\mathbf{q}} h(\mathbf{q}) \tag{5.17}$$

The remainder of this section includes an experimental demonstration of the functionality of the proposed method. A simulation study is presented first, followed by experimental validation on the physical system.

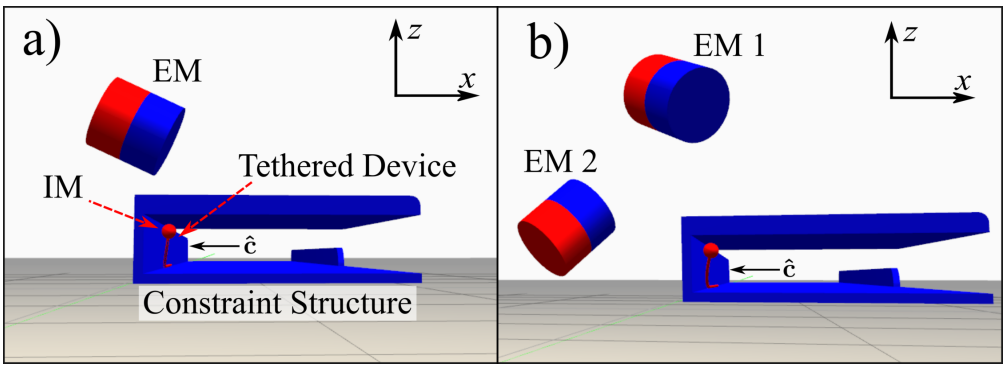

Figure 5.6: The Gazebo simulation environment with a) a single-EM environment and b) a double-EM environment. In all trials, a desired force was set in the -x direction while motion was controlled in the y direction where a desired position was set. (©2019 IEEE [4])

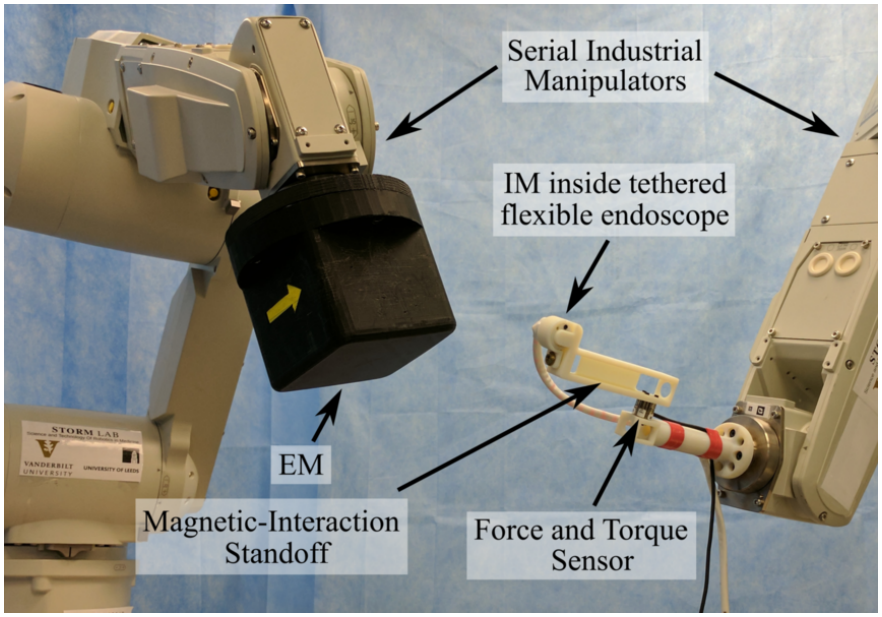

Figure 5.7: The experimental platform. A manipulator maneuvers an EM while another identical manipulator maneuvers an IM. The wrench applied on the IM is measured with a force and torque sensor. (©2019 IEEE [4])

5.4.2 Simulation Study

To evaluate the ability to algorithmically lower the value of g, and thus f_{c_a} and in turn f_c, when manipulating an IM, a series of simulation trials ws conducted. The control was applied as stated in Eq. (5.14). The $\delta\mathbf{f}_{des}$ term was used for both position and force control as shown in Eq. (5.18) where $\mathbf{e}_p$ and $\mathbf{e}_f$ indicate position and force errors, respectively. Position is controlled in a motion

direction that is orthogonal to $\hat{\mathbf{c}}$ and indicated by $\hat{\mathbf{p}}_m$. Both the contact force control and motion control directions are orthogonal to the vertical axis along which gravity is applied. The projection matrix that projects into this direction of motion is defined as $\mathbf{P}_m = \hat{\mathbf{p}}_m \hat{\mathbf{p}}_m^{\mathrm{T}}$. Implementation of proportional-integral-derivative (PID) control is indicated via $pid()$. Simulations were conducted with $\hat{\mathbf{c}}$ directed in the inertial $-x$ and y directions, referred to as $-\hat{\mathbf{x}}$ and $\hat{\mathbf{y}}$, respectively.

$$\delta \mathbf{f}_{des} = (\mathbf{I} - \mathbf{P}_m) pid(\mathbf{e}_f) + \mathbf{P}_m pid(\mathbf{e}_p) \tag{5.18}$$

One set of experiments was conducted using a Gaussian localization uncertainty of 10 mm and 10° and another with 15 mm and 15°; the localization uncertainty was varied to observe whether algorithm performance was affected by noise magnitude. The localization uncertainty is applied in each pose component, i.e. position and orientation along all axes. These localization noise magnitudes were selected as they are near the upper boundary of uncertainty observed in physical systems [155, 82, 143, 156, 83, 53]. Each set of experiments consisted of both "*static*" and "*dynamic*" trials. During the *static* trials, the IM is kept fully constrained while during *dynamic* trials, the IM and its tether are able to move freely and thus be subject to motion control in addition to force control. During *static* trials when $\hat{\mathbf{c}}$ was in the $-\hat{\mathbf{x}}$ direction, the IM's heading was aligned with $\hat{\mathbf{c}}$, while during *static* trials when $\hat{\mathbf{c}}$ was in the $\hat{\mathbf{y}}$ direction, the IM's heading was orthogonal to $\hat{\mathbf{c}}$, though still on the horizontal. This was done to evaluate the influence of various orientations.

The *static* and *dynamic* trials were conducted using both a single EM and two EMs, and two sets of experiments for each combination of experimental parameters were conducted. These combinations can be visualized in the results Table 5.2. Trials of "Set No." 1 were subject to a desired force of 0.27 N in the direction of $\hat{\mathbf{c}}$ and 0.75 N in the vertical; this resulted in a desired force with a magnitude of 0.8 N and an orientation of 70° from $\hat{\mathbf{c}}$. Trials of "Set No." 2 were subject to a desired force of 0.61 N in the direction of $\hat{\mathbf{c}}$ and 0.51 N in the vertical; this resulted in a desired force with a magnitude of 0.8 N and an orientation of 40° from $\hat{\mathbf{c}}$.

The dynamic trials of "Set No." 1 resulted in the IM pressed against the contact-wall, as well

as the upper-barrier, or ceiling, as shown in Fig 5.6. The dynamic trials of "Set No." 2 resulted in the IM pressed against the contact wall, but floating in the vertical direction. Each "trial" consisted of five simulations run without the use of algorithm and five simulations with the algorithm. Each simulation ran for 80.0 s. Only the final 30.0 s of each simulation, the steady-state period, was post-processed as to avoid capturing data from the early, transient, period where magnets move to reduce force error and to reduce g. The homogeneous force solution that minimizes g was limited to a threshold magnitude after 35.0 s. A larger influence of the homogeneous component in the transient period allowed for the EM(s) to maneuver closer to a g minimum before the start of the steady-state period. The magnitude of the particular solution was not varied between trials as modifying it would have an influence on force uncertainty and thus would not allow for a direct evaluation of the algorithm's efficacy.

Results are shown in Table 5.2 (10 mm, 10° noise) and Table 5.3 (15 mm, 15° noise). The results reported in this table are the following: "f_c err": force error in $\hat{\mathbf{c}}$ from the desired, "$g/|f_{c_a}|$": the value of g normalized against force magnitude, CV_a, CV_t, and the ratios of CV_a and CV_t with and without the use of the algorithm. The values of CV_a were computed via dipole model using the noisy force estimate, i.e. what the algorithm "sees", while the values of CV_t were computed via dipole model using the true IM pose. The final ratios explicitly show the factor of improvement in uncertainty when using the algorithm.

The values reported here result from computation of the mean of the means of each simulation, i.e. the value reported as CV_a is the mean value of the CV_a's of each simulation and five simulations are conducted for each data point. A filter was used to smooth both EM commands and the computed gradient of g. The interactions between the two actuating EMs were not considered in this work. In a platform implementation, a component of actuation redundancy should be used to minimize the interaction force between the EMs. The EMs did tend to collide at times and a further work on actuation control would be necessary to physically implement this experiment. Localization feedback was acquired at 100 Hz and was not filtered. The motion control in *dynamic* experiments was used to simply keep the IM in its initial position.

When the algorithm was used, the EMs changed orientation until a local minimum in g was reached. Results suggest that the use of the algorithm robustly reduces uncertainty. The factor of improvement of CV_a was always above 1.0, and the factor of improvement of CV_t was typically at, or near, 1.0. The maximum factor of improvement of CV_t when using a single EM was 2.81 in *static* experiments and 1.69 in *dynamic* experiments. The maximum factor of improvement of CV_t during double-EM experiments was 1.65 in *static* experiments and 3.10 in *dynamic* experiments. The uncertainty-improvement results for single-EM *static* trials were better when the IM's heading was orthogonal to $\hat{\mathbf{c}}$, as compared to when the heading was aligned with $\hat{\mathbf{c}}$; this suggests a varied ability for the EM to find various local minima in g. There was not a discernible effect in uncertainty reduction with varying levels of localization noise.

These results demonstrate that the algorithm robustly improves both the expected uncertainty, CV_a, and the true force uncertainty CV_t. It is noteworthy that the use of this algorithm also tended to reduce the error in f_c. Furthermore, the value of g/f_{c_a} was always reduced, demonstrating the controllability of ellipsoid size. The improvement factor of CV_t was drastically smaller during double-magnet experiments of Set No. 2, and the error in f_c increased. This is a result of the IM's weight being nearly balanced by the applied force. As the magnitude of the homogeneous twist on magnets is limited in software, the IM was subject to variability to forces in the vertical direction owing to the oscillation of the EMs. The IM experienced more oscillation when subject to the algorithm, as without it, one magnet would move farther from the IM and the magnets. This adverse effect would likely be improved by slowing the homogeneous solution and also would likely not be as evident in a physical system owing to the presence of environmental damping. The factor of improvement of CV_a in these cases was greater than 1.0.

One reason for limited controllability over the value of g is that the major axis of $\tilde{\mathbf{J}}_{Fi}$ tends to align with the magnetic force vector. The conclusion is based on a numerical simulation that was conducted where 10,000 random EM poses were generated with a constant IM pose and the angle between the major ellipsoid axis of $\tilde{\mathbf{J}}_{Fi}$ and the magnetic force vector was recorded. The angle difference was found to be $22.9 \pm 16.6^\circ$. This simulation was repeated with a constraint that the $\hat{\mathbf{m}}_i$

Table 5.2: Simulation experiment results. Localization noise: 10 mm, 10° (©2019 IEEE [4])

				No Algorithm				Algorithm				$\frac{CV_{a_{no-alg}}}{CV_{a_{alg}}}$	$\frac{CV_{t_{no-alg}}}{CV_{t_{alg}}}$
Mode	EMs	$\hat{\mathbf{c}}$	Set No.	f_c err (%)	$g/\lvert f_{c_a}\rvert$	CV_a	CV_t	f_c err	$g/\lvert f_{c_a}\rvert$	CV_a	CV_t		
Static	1	$-\hat{\mathbf{x}}$	1	6.2	120.7	81.4	6.4	6.5	105.2	74.9	5.8	1.09	1.10
			2	1.7	57.7	32.7	2.0	2.2	54.7	32.3	2.5	1.01	0.81
		$\hat{\mathbf{y}}$	1	8.8	107.9	78.3	6.0	3.2	69.4	36.0	3.2	2.18	1.89
			2	4.1	59.3	36.3	2.5	2.4	55.3	33.2	2.8	1.10	0.88
	2	$-\hat{\mathbf{x}}$	1	8.9	122.8	80.8	10.4	5.3	52.2	57.7	6.3	1.40	1.65
			2	3.4	56.7	33.2	3.8	2.3	28.6	22.1	2.6	1.50	1.47
		$\hat{\mathbf{y}}$	1	7.6	119.6	72.5	8.8	6.4	18.9	59.7	6.9	1.21	1.28
			2	4.4	61.4	36.6	4.3	2.5	9.5	24.0	2.9	1.52	1.48
Dynamic	1	$-\hat{\mathbf{x}}$	1	18.1	95.7	56.1	3.0	7.0	81.9	49.3	1.8	1.14	1.62
			2	6.9	55.8	29.7	1.2	7.3	53.4	28.0	1.4	1.06	0.89
		$\hat{\mathbf{y}}$	1	20.8	94.3	55.0	2.7	7.4	82.1	49.9	1.6	1.10	1.69
			2	7.8	55.4	29.8	1.3	7.7	52.8	28.3	1.2	1.05	1.07
	2	$-\hat{\mathbf{x}}$	1	16.1	97.0	56.9	3.63	6.6	25.1	24.6	1.2	2.31	3.10
			2	7.6	55.3	30.2	1.8	94.2	34.4	24.9	10.6	1.21	0.17
		$\hat{\mathbf{y}}$	1	17.0	95.4	57.8	3.2	6.3	27.6	26.4	2.1	2.19	1.52
			2	7.3	54.9	29.9	1.8	218.0	44.2	27.6	13.0	1.09	0.14

aligns with the field of the EM where the result was $3.9 \pm 1.4°$. These results suggest that a bias exists in the shape of the ellipsoid of $\tilde{\mathbf{J}}_{Fi}$, which is expected owing to the force being a direct result of field gradient. As a result of this, the algorithm typically had greater impact in experiments of Set. No. 1.

Finally, to demonstrate the algorithm's functionality in the transient during *static* experiments, Fig. 5.8. Here, a similar experiment protocol was followed (Table 5.2); however, the algorithm was activated after 20 s rather than immediately, to ensure that force error had reached a noisy steady state. The reduction in the value of g can be seen after 20 s, when the algorithm was activated. The force uncertainty drops during steady-state operation of the algorithm.

5.4.3 Evaluation on Physical System

Physical platform experiments were conducted to demonstrate the methodology on a real magnetic system. As an ideal dipole, i.e. sphere, is not used for the EM and IM for design purposes, experimentation began with a characterization of the sensitivity ellipsoids of the system in Section 5.4.3.1. As the ability to draw conclusions and make algorithmic decisions based on sensitivity ellipsoid hinges on the validity of the dipole approximation, such characterization is recommended.

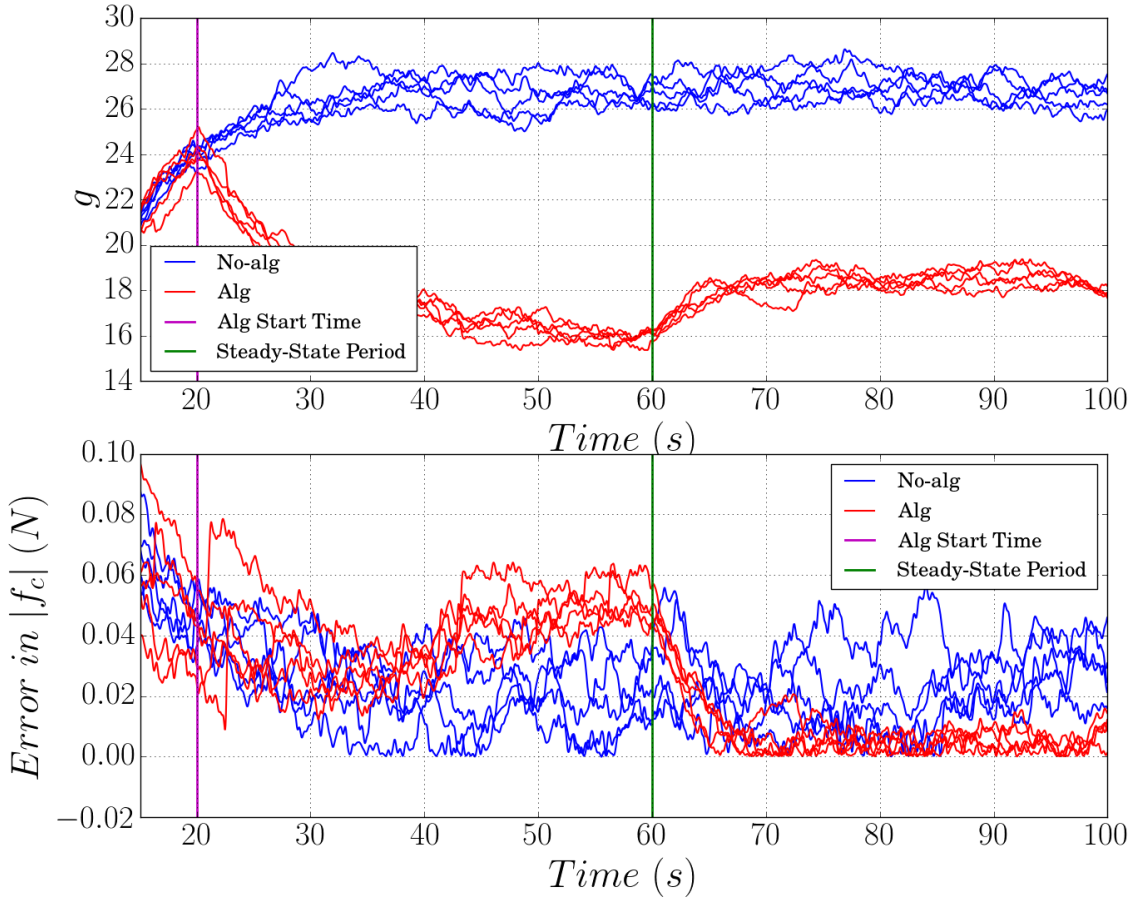

Figure 5.8: The results of 5 static trials with and without the uncertainty-reducing algorithm where a 10 mm and 10° is applied. When using the algorithm, it was activated after 20 s. After 60 s, the homogeneous solution was scaled down, which is referred to as the start of the "steady-state period". The particular solution is not scaled between trials. In the top plot, the algorithm reduces the value of g). In the bottom plot, the uncertainty is visibly lowered when the algorithm is in effect and its homogeneous twist that reduces g is scaled down. All data in these plots were filtered to improve visualization. (©2019 IEEE [4])

A series of experiments was therefore conducted that show that the general behavior of ellipsoids in the physical system aligns with that which is expect from the linearized dipole model. The force-uncertainty-reducing algorithm was then validated and is discussed in Section 5.4.3.2. The experimental setup used for all platform experiments is shown in Fig. 5.7.

Table 5.3: Simulation experiment results. Localization noise: 15 mm, 15° (©2019 IEEE [4])

				No Algorithm				Algorithm				$\frac{CV_{a_{no-alg}}}{CV_{a_{alg}}}$	$\frac{CV_{t_{no-alg}}}{CV_{t_{alg}}}$
Mode	EMs	$\hat{\mathbf{c}}$	Set No.	f_c err (%)	$g/\lvert f_{c_a}\rvert$	CV_a	CV_t	f_c err	$g/\lvert f_{c_a}\rvert$	CV_a	CV_t		
Static	1	$-\hat{\mathbf{x}}$	1	18.2	138.3	143.4	10.2	14.7	114.5	124.8	9.5	1.15	1.07
			2	3.4	59.2	51.7	3.2	3.3	57.1	51.0	3.2	1.01	1.01
		$\hat{\mathbf{y}}$	1	18.6	108.3	126.7	11.0	5.1	73.0	62.1	3.9	2.04	2.81
			2	9.9	59.9	60.7	4.3	8.0	58.0	57.1	4.3	1.06	1.01
	2	$-\hat{\mathbf{x}}$	1	15.3	139.5	147.3	13.0	13.5	86.6	107.5	11.0	1.37	1.18
			2	4.6	59.9	53.1	4.9	4.0	39.1	38.4	4.7	1.38	1.05
		$\hat{\mathbf{y}}$	1	8.8	126.0	119.3	9.8	10.5	39.4	91.7	8.3	1.30	1.18
			2	5.9	65.4	58.1	6.2	6.5	14.2	37.9	3.7	1.53	1.65
Dynamic	1	$-\hat{\mathbf{x}}$	1	30.9	98.9	88.1	2.0	15.3	87.0	81.4	1.5	1.08	1.33
			2	18.8	59.1	47.7	1.7	15.0	55.3	46.6	1.8	1.02	0.95
		$\hat{\mathbf{y}}$	1	33.4	98.1	82.0	2.2	18.5	87.3	79.6	1.7	1.03	1.32
			2	21.2	58.3	48.8	1.9	18.4	55.3	46.0	1.8	1.06	1.03
	2	$-\hat{\mathbf{x}}$	1	27.3	103.6	90.9	3.9	8.2	24.75	41.75	2.4	2.18	1.63
			2	17.8	58.4	48.0	2.1	35.5	30.7	34.6	8.3	1.39	0.25
		$\hat{\mathbf{y}}$	1	28.8	99.8	89.2	3.9	12.5	26.4	44.4	1.7	2.01	2.28
			2	17.1	58.4	48.3	2.2	28.8	29.4	30.0	10.3	1.61	0.21

5.4.3.1 Validation of Sensitivity Ellipsoids

To validate the correspondence of ellipsoid shapes on the non-dipole platform with a dipole prediction, an EM that is moved by a serial manipulator is used as well as a second serial manipulator to perturb the position and orientation of the IM. In general, force and torque can be applied in 3 DoF each, resulting in a 6 DoF task space. Only two torque DoFs are controllable owing to a dipole's symmetry. Four primary Jacobians that were defined in Eq. (5.6) are of concern: $\mathbf{J}_{Fp_i}$, $\tilde{\mathbf{J}}_{F\omega_i}$, $\mathbf{J}_{Tp_i}$, and $\tilde{\mathbf{J}}_{T\omega_i}$, each of which are $\in \mathbf{R}^{3\times3}$. As the purpose of this analysis is to convey the similarity in ellipsoid shape, it is most intuitive to visualize the ellipsoids in 2D. For each Jacobian, nine 2 DoF combinations exist.

Discrete points that form the sensitivity ellipsoids are experimentally recorded by perturbing the pose of the IM in planes e.g. moving the IM in a circle on the XY plane, then XZ plane, then YZ plane, and repeating for angular DoFs. As the IM is mounted on a force and torque sensor, force and torque are recorded at each of these poses. Each circle was discretized to 12 data points. At each of these 12 points, 2000 force and torque readings were collected. As many of the perturbations were within the sensitivity of the force and torque sensor, the large number of data points allowed for a more accurate mean reading. Finally, the resultant ellipsoids of force and

torque perturbations were plotted along with the predicted dipole-dipole Jacobian value as well as the discrete theoretical expected result obtained from dipole force and torque equations.

This theoretical discrete expected result was computed by gathering data at each discrete point as traveled by the IM; however, instead of a measurement, it is the force and torque as estimated via dipole-dipole model. This computed result is shown to visualize potential losses of Jacobian linearity. Given that the dipole force and torque estimates may have slight inaccuracies, of greater interest is the general behavior of a Jacobian; thus, improper scaling of an ellipsoid is accepted as are minor deviations from the expected shape. Multiple sets of experiments were conducted. The results of two experiments, experiment numbers 3 and 4, are shown in Fig. 5.9 and Fig. 5.10, respectively.

The ellipsoids' correctness was evaluated by computing the measured and dipole-predicted major to minor axis length ratio, as well as the angle tilt of the ellipsoid. For the data shown in Fig. 5.9, the ellipsoid major-to-minor axis ratio error was 27.0 $\pm$ 25.7% and the ellipse tilt error was 10.0 $\pm$ 17.8° (36 ellipsoids). The results of the 6 tests were: an ellipse ratio error of 47.7 $\pm$ 79.9% and an ellipse tilt error of 13.5 $\pm$ 20.5°. When processing the result for all 8 trials, including the outliers, the results were 86.1 $\pm$ 204.4% and 13.5 $\pm$ 19.6° for ellipse ratio error and ellipse tilt error, respectively. The high errors are likely attributed to the greater impact of sensor noise and robot registration errors in instances where the magnetic Jacobian is ill-conditioned i.e. the Jacobian's ellipsoids are thinner in certain DoFs. The correctness of sensitivity ellipsoid direction compared to magnitude is more important in this application as this direction is used by this algorithm to dictate EM motions. As the measured behavior of the ellipsoids is, in general, consistent with the linearized dipole model, only one set of results is shown. These results suggest that on this physical system, the dipole model can be used to make inferences regarding sensitivity. Any errors that may exist in the ellipsoid assumption will adversely affect performance.

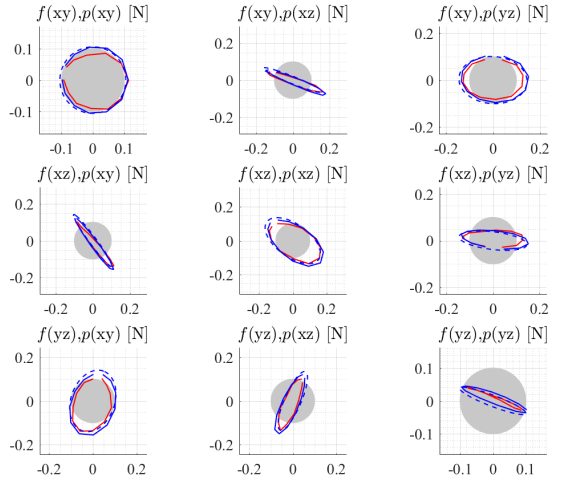

(a) Results for $\mathbf{J}_{Fp_i}$

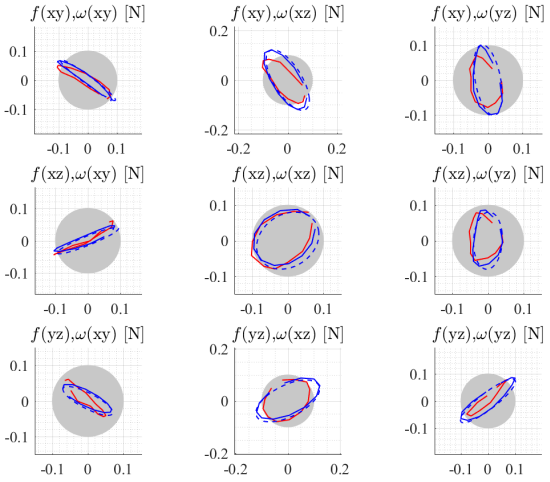

(b) Results for $\tilde{\mathbf{J}}_{F\omega_i}$

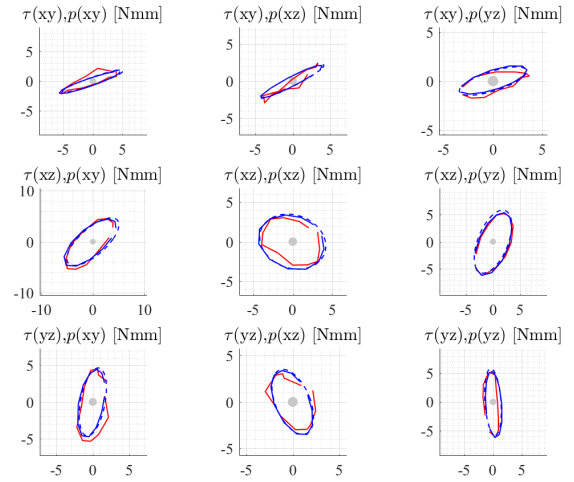

(c) Results for $\mathbf{J}_{Tp_i}$

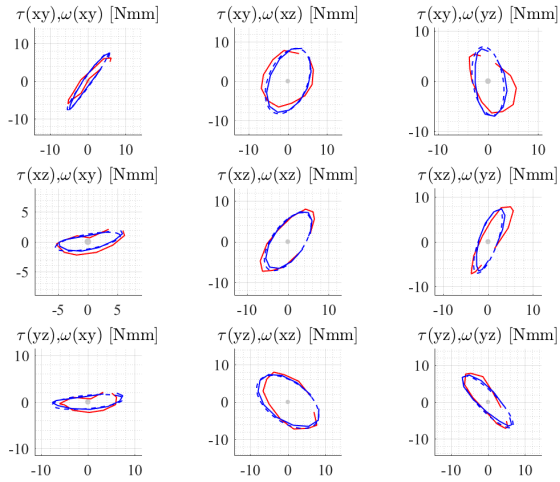

(d) Results for $\tilde{\mathbf{J}}_{T\omega_i}$

Figure 5.9: Results of a pose perturbation experiment showing the consistency between theoretical and observed behavior of the $\tilde{\mathbf{J}}_i$ Jacobian. The configuration of the magnets is arbitrary: $\mathbf{p} = [0.125, -0.069, -0.065]^{\mathrm{T}}$, $\hat{\mathbf{m}}_i = [0.422, -0.887, -0.187]^{\mathrm{T}}$, and $\hat{\mathbf{m}}_e = [-0.909, 0.415, 0.044]^{\mathrm{T}}$. The magnets were separated by 16 cm, with respective nominal dipole force and torque magnitudes of 1.0 N and 37 N-mm. Here, the red line represents the experimental result, the solid blue line represents the discrete theoretical result, and the dashed blue line represents the theoretical Jacobian prediction. The gray circle indicates the sensors sensitivity. (©2019 IEEE [4])

5.4.3.2 Force Control Algorithm Evaluation

The force control algorithm's function was validated on the physical platform by using an external sensor measurement to confirm that force uncertainty was reduced. These experiments

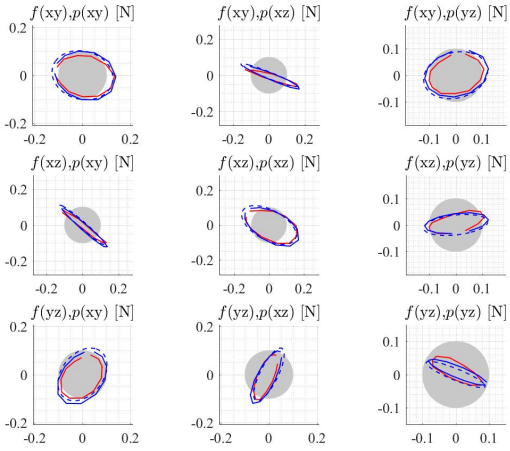

(a) Results for $\mathbf{J}_{Fp_i}$

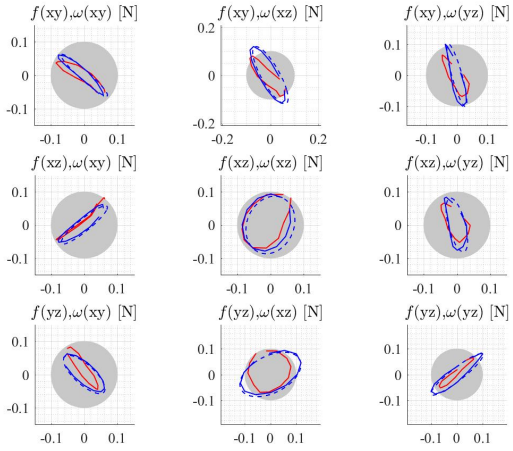

(b) Results for $\tilde{\mathbf{J}}_{F\omega_i}$

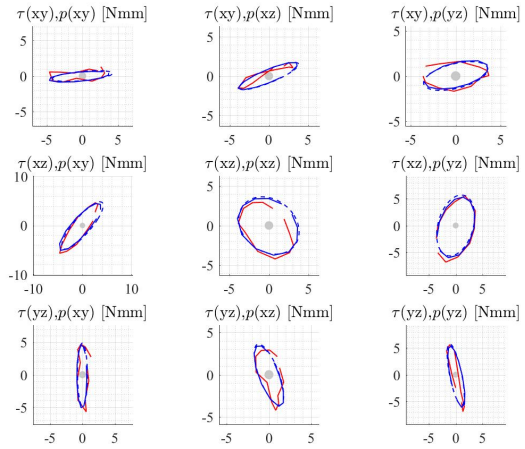

(c) Results for $\mathbf{J}_{Tp_i}$

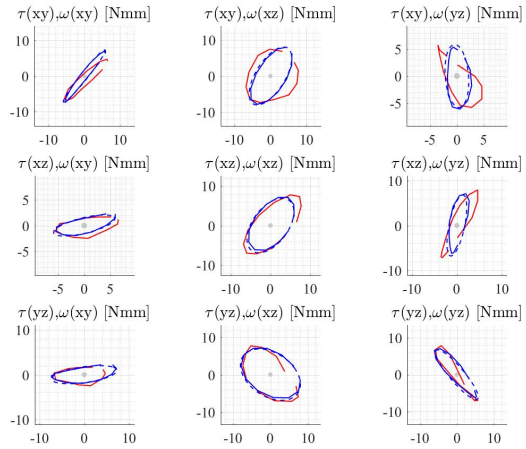

(d) Results for $\tilde{\mathbf{J}}_{T\omega_i}$

Figure 5.10: Results of a pose perturbation experiment showing the consistency between theoretical and observed behavior of the $\tilde{\mathbf{J}}_i$ Jacobian. The configuration of the magnets is arbitrary: $\mathbf{p} = [0.132, -0.069, -0.057]^{\mathrm{T}}$, $\hat{\mathbf{m}}_i = [0.311, -0.920, -0.237]^{\mathrm{T}}$, and $\hat{\mathbf{m}}_e = [-0.958, 0.286, 0.023]^{\mathrm{T}}$. The magnets were separated by 16 cm, with respective nominal dipole force and torque magnitudes of 0.9 N and 33 N-mm. Here, the red line represents the experimental result, the solid blue line represents the discrete theoretical result, and the dashed blue line represents the theoretical Jacobian prediction. The gray circle indicates the sensors sensitivity.

were conducted while keeping the IM in a fixed pose as shown in Fig. 5.7. Owing to the presence of two serial robots in close proximity, the experimental workspace was small. Given an initial condition of magnet positions, the use of this uncertainty-reducing algorithm results in a new EM

pose that is unknown at the start of the experiment; this presents a path-planning problem for collision avoidance. In this work, the development of a path-planning algorithm was avoided, and instead, a brute-force numerical simulation was conducted to evaluate initial experimental parameters and determine if the EM is likely to approach an undesirable configuration. Given a set of acceptable conditions, i.e. that would not result in robot collision, conditions were chosen that were expected to reduce the size of g more significantly, end thus be more likely to reduce CV_t by a larger amount.

It should be noted that such search was not done in any simulation trials. Whereas the aim of this experiment was to demonstrate how much CV_t can be affected by applying this methodology, the system can use the force uncertainty reducing algorithm constantly; the system will take advantage of the null-space reduction of g when possible. In these experiments, a desired force was commanded. Increments in wrench, used to compute desired EM motion, were computed using PID control as shown in Eq. (5.14) and Eq. (5.19).

$$\delta \mathbf{f}_{des} = pid(\mathbf{e}_f) \tag{5.19}$$

Similar to the protocol for simulations, eight experiments were conducted; each of which consisted of five trials without the algorithm, and five trials with the algorithm in use. Data was recorded for 80 s and only the final 30 s was analyzed as to capture steady-state behavior. A trial period of 80 s allowed the system to reach a steady-state point in any attempted experiment configuration. The joint values sent to the manipulator were filtered to avoid shaking of the robot. As in some simulations, during all experiments, a Gaussian localization uncertainty was set to 15 mm and 15°. Localization feedback was acquired at approximately 100 Hz and was not filtered. The true value of f_c was measured using a force and torque sensor mounted on the end-effector of a second serial manipulator (Fig. 5.7).

The experimental results are reported in Table 5.4. The reported values were computed in the same manner as they were in simulation trials; however, the value of CV_t here was computed using

Table 5.4: Platform experiment results (©2019 IEEE [4])

		No Algorithm			Algorithm			$\frac{CV_{a_{no-alg}}}{CV_{a_{alg}}}$	$\frac{CV_{t_{no-alg}}}{CV_{t_{alg}}}$
Trial No.	Des. Force (N)	$g/\lvert f_{c_a}\rvert$	CV_a	CV_t	g/f_{c_a}	CV_a	CV_t		
1	$[-0.05, -0.16, 0.47]$	306.6	346.3	41.0	62.0	123.1	18.6	2.81	2.20
2	$[-0.04, -0.31, 0.39]$	395.4	384.5	35.4	288.1	295.5	32.7	1.30	1.08
3	$[-0.08, -0.27, 0.41]$	212.9	224.1	28.4	63.6	95.9	12.3	2.34	2.31
4	$[-0.07, -0.07, 0.49]$	238.3	287.0	45.5	54.9	86.0	18.2	3.34	2.50
5	$[-0.12, -0.39, 0.29]$	168.6	171.6	17.9	61.7	16.6	9.3	2.24	1.93
6	$[-0.10, -0.11, 0.48]$	154.6	174.2	20.5	63.3	89.2	11.5	1.95	1.79
7	$[-0.11, -0.34, 0.34]$	158.3	153.0	17.7	72.0	67.7	10.1	2.26	1.66
8	$[-0.09, -0.30, 0.39]$	211.1	246.4	27.9	53.7	53.5	11.4	4.61	2.45

the external sensor, rather than a dipole-model estimate. The outcome of this result analysis is the mean value of g that is normalized by dividing by the mean $|f_{c_a}|$, as well as CV_a that was defined in Eq. (5.11), and CV_t that was defined in Eq. (5.12). The true value of contact force, f_c, was obtained from sensor measurements. When the algorithm was in use, CV_a was reduced by a factor of up to 4.6, and CV_t was reduced by a factor of up to 2.5 (trial 4).

5.5 Discussion

In this work, the functionality of the novel force uncertainty reducing algorithm was demonstrated in both simulations and platform experiments. The algorithm reduced force uncertainty in the majority of simulations and all platform experiments. The algorithm was evaluated in the case of using a single EM as well as using two EMs. Functionality was demonstrated in two directions in space, as well as with two levels of applied localization noise. Simulations were conducted in both a static manner, where the IM was fixed in space, as well as in a dynamic manner, where the IM was free to move in response to environmental forces. The algorithm reduced force uncertainty in both static and dynamic experiments. The methodology applied in this work may be improved by differentiating magnet heading in an $\mathbb{S}^2$ manifold, as the magnetic strength of a permanent magnet is constant. Furthermore, we note that a further improvement to the proposed method may include a consideration for the sensitivity of actuation Jacobians, e.g. $\mathbf{J}_{Fe_k}$ (Eq. (5.7)), to localization noise and, in turn, the implications of their ellipsoid shapes.

The focus of this work was on optimizing force control precision, rather than accuracy, i.e. ensuring that the obtained force was precisely what was desired. This was done for two reasons: (1) on this platform, the magnets are not ideal dipoles and thus any measured force error is attributed to both robot registration error as well as imperfect field modeling and (2) the same control methodology cannot be applied for all experiments i.e. control gains must be adjusted based on amount of force and amount of localization noise. To address (1), a future researcher can use spherical magnets or implement more accurate field models such as the current model [62]. Works in robotic capsule endoscopy have implemented such models previously [157]. To address (2), an adaptive controller is likely a proper solution assuming that the field modelling is accurate. Control parameters were intentionally kept constant between trials to minimize the number of variables in the analysis. To compensate for any inaccuracies in force accuracy, the results in this work are normalized with respect to force magnitude.

This work is relevant for groups working with magnetic manipulation of *in-vivo* devices whether they be untethered or partially constrained by a catheter or continuum robot. The methods were developed for permanent magnet systems where the IM is a single dipole, but can be extended to cases where multiple IMs are used or if the controlled device is composed of a sphere of soft-magnetic material such that effects of shape on magnetization are negligible [158, 159]. In such case, the actuation system would gain torque redundancy as the soft-magnetic material would be less likely to align with the external field. These methods can also be extended to electromagnetic actuation systems by adding derivative relations between coil currents. As four coils are needed for a force control task and eight coils are needed for a force-and-torque control task, torque redundancy can be used for implementing this proposed algorithm [72]. This methodology was evaluated on a cm-scale system but can be applied for control of robots in smaller scales where precision of motion is especially necessary. Finally, this work gives insight into the use of manipulability ellipsoids for magnetic actuation, as is commonly done for rigid-link manipulators.

5.6 Conclusion

In this work, a sensitivity ellipsoid analysis of a magnetic actuation Jacobian was applied to improve the uncertainty in applied force in the presence of localization noise. This method relies on defining a direction during a force control task in which the precision of force application is favored. By manipulating the configuration of the EM in the differential force nullspace, the proposed algorithm minimizes the shape of a sensitivity ellipsoid in the direction of desired force precision improvement. This method decreases the uncertainty in applied force both in simulation and physical experiments. In simulation experiments, an IM that was embedded in a tethered shell was commanded to a force control task in cases where the IM was fixed in space, as well as free to rotate. The latter experiments demonstrated that although the IM was rotated owing to the algorithm acting in the force nullspace and thus applying varying torques, the force uncertainty was still decreased. Physical experiments were conducted on the MFE platform. Whereas force control is useful in and of itself, it is the intrinsic method for actuating magnetically controlled robots as no rigid coupling exists between an actuator and an end-effector. This method may be applied in systems with mechanical constraints, such as magnetically guided catheters or continuum robots, where the orientation of a guiding IM is partially constrained. Increasing accuracy of the force applied will affect the motion of magnetic robots to a degree that will vary based on the magnitude of localization uncertainty.

Chapter 6

Towards Inverse-Dynamic Control of Tip-Actuated Endoscopes without Configuration Sensing

The prior chapters in this dissertation concerned the use of magnetic fields for the control of a tip-actuated endoscope (the MFE). These methods relied on an assumption that the endoscope's tip is a quasistatic, tetherless, dipole. In this chapter, this assumption is abandoned and the mechanics of the tether are considered. Owing to the complex nature of the mechanics of the tether and its uncertain interaction with the environment, probabilistic methods are applied to attain a dynamic tether state estimator. The methods in this chapter do not require the use of auxiliary sensors and rely solely on the localization of the tip itself. The following publication is an output of this work: Ref. [7] (*Slawinski P.R., Simaan N.S., Obstein K.L., Valdastri P., Sensorless Estimation of the Planar Distal Shape of a Tip-Actuated Endoscope, IEEE Robotics and Automation Letters, 06/2019*).

6.1 Introduction

Magnetic actuation has been used to control devices with [54] and without [47] a tether, as well as continuum devices that include flexible endoscopes, needles, catheters, and robots [160, 55, 53, 161]. Earlier chapters in this dissertation presented discussion and results of controlling a tethered device, the MFE, with an assumption that the controlled dipole is tetherless and is quasistatic. This assumption implies that the disturbance from the mechanics of the tether of the device were negligible. Although control is feasible with this assumption, it is evident that mechanics play a significant role in the motion of the tip-actuated endoscope. If this disturbance could be known, a computed-torque controller could be applied which may lead to more accurate trajectory control and improved tracking. The objective of this chapter to the use of a sensorless estimation method for recovering information on tether disturbance so that it may be used for the computed-torque

control of a tip-actuated endoscopic robot. This inherently provides a method for estimating the approximate local distal shape of a tip-actuated endoscope. Although magnetics are the means of actuation in this chapter, these methods are valid for other sources of actuation wrench applied at the tip. The term "computed-torque control" in this chapter encompasses control laws that rely on mechanics information, configuration error terms, and trajectory-specific feedforward terms.

The implementation of computed-torque control typically involves the modelling of the robot structure using sensory feedback from joints to obtain the kinematic configuration, and using direct actuation of the configuration parameters, i.e. joints, via a control law that incorporates linearized mechanics information. An example of a computed-torque control law is shown in Eq. (6.1) where $\mathbf{q}$ indicates a vector of joint values, $\dot{\mathbf{q}}$ indicates joint rates, $\ddot{\mathbf{q}}_{des}$ indicates desired joint accelerations, $\mathbf{D}$ indicates the mass inertia matrix, and $\mathbf{h}(\mathbf{q},\dot{\mathbf{q}})$ is a vector that contains Coriolis and centrifugal terms [162].

$$\tau = \mathbf{D}(\mathbf{q})(\ddot{\mathbf{q}}_{des} + pid(\mathbf{q}_{err})) + \mathbf{h}(\mathbf{q},\dot{\mathbf{q}}) \tag{6.1}$$

In the case that the robot's configuration is known, modelling of the continuum device could be approached via existing methods [163, 164, 165, 166, 167, 168, 169, 170, 171]. Similar methods have been applied for continuum devices that rely on magnetic fields for actuation [160, 55, 46]. Such approaches not trivial in the case of tip-actuated tethered devices as: (1) there is no known robot "base" as the entire tether translates via the pulling of its tip, and (2) the shape of the tether is passive and dictated by both the actuation signals as well as the environment.

Common sensing modalities that are used for configuration and pose sensing include fiber Bragg gratings (FBG) [172, 173], electromagnetic tracking [174], and intraoperative imaging (fluoroscopy, ultrasound) [175]; however, these modalities cannot be trivially used in all devices. Shape estimation using FBG is expensive owing to the need of an optical spectrum interrogator with multiple channels [175], and the estimate may degrade owing to propagation losses when bending occurs past a threshold curvature [176] and the estimate may vary with changes in temperature [174]. This is especially true for devices such as the MFE that could otherwise be made single-use, or disposable. Electromagnetic sensing cannot be used with magnetic actuation sys-

tems unless the tracking and actuation systems are compatible. The use of intraoperative imaging contributes to system complexity and cost and can expose patients to radiation. A potential simple approach for recovering shape may be the tracing of the path of the tip of the endoscope; however, this method may be limited by: the uncertainty in the tether's configuration in the lumen (i.e. tether may shift side-to-side), the need for the tether to be in tension (an operator may insert too large of the tether's length such that it loops in the lumen), and the dynamic nature of the colon (i.e. the configuration of the bowel may shift, especially if patient's configuration is changed).

Sensor-based approaches for estimating the shape of continuum devices have been investigated. A common approach for shape sensing for continuum robots is the use of strain sensing along the manipulator's axis [176]. Trivedi and Rahn proposed three sensor-based planar shape estimation techniques intended for their pneumatically actuated 12 DoF manipulator: (1) load cell feedback at robot's base to facilitate internal reaction integration that changes the Cosserat rod problem from a boundary-value-problem to an initial-value-problem [177], (2) feedback from encoder cables that are mounted in each of the three pneumatic robot sections that provide feedback on manipulator bending and extension, and (3) sensing using inclinometers mounted along the body of the robot that provide additional boundary conditions that are used for computing the configuration of the manipulator [176]. Tully et al. implemented a shape sensing technique for a fixed-base cable-driven continuum robot that relies on a single 6 DoF EM sensor at the tip of the robot [174]. Other groups have used external cameras for recovering shape; however, this is not applicable for medical approaches [178].

A knowledge gap exists in the ability to estimate, without auxiliary sensors, the mechanical disturbance and shape of a tether with an unknown configuration. The use of additional sensors is avoided in this work to maintain simple manufacturability of the MFE and minimize potential calibration procedures necessary for clinical use. This chapter contains a description and validation of a proposed probabilistic method, that relies on a simple dynamic model, for the estimation of the 2D shape of the distal portion of a tip-actuated endoscope. The method is then further validated by using information from the estimated model configuration in the magnetic control of the MFE and

evaluating the influence of this information on the orientation errors in trajectory following. This work relies on an extended Kalman filter and a single pose sensor at the tip, similar to what is done in Tully's work [174], however, the methods applied in this dissertation pertain to a continuum device that does not have the stability of a rigid device, does not inherently behave as a follow-the-leader device (the tether shifts passively), and does not have a fixed robot base. This chapter begins with a description of the system, then continues with a description of the methods (i.e. approach to the magnetic control, dynamic model, and estimator). The methods of validation are then described and results are presented. The chapter ends with a conclusion of observations and statements on potential future directions of this work.

6.2 System Overview

The methods applied in this work are validated using the MFE system, described in Chapter 1. The experimental setup used in this work is shown in Fig. 6.1. In addition to the previously described MFE, serial robot, and EPM, this system includes a custom tether shape measurement platform that is based on the video feedback of a single camera ("Creative Live!", Creative Labs, Singapore). The camera is used to detect three color markers on the tether of the MFE. Processing of images was done using OpenCV [179]. The conversion from pixels to positions in the robot's frame was achieved by registering the camera's output using a least-squares fitting [154]. All color markers are assumed to be planar; this is an acceptable assumption as the trajectory followed by the MFE was on the horizontal, while the camera faced the vertical direction. The estimator operates at approximately 28 Hz.

6.3 Methods

6.3.1 Magnetic Control of MFE Tip

The magnetic actuation of the tip of the MFE that is applied here is similar to that described in Chapter 2. The expression for the commanded change in magnetic wrench, $\delta \mathbf{w}_c$, is shown in

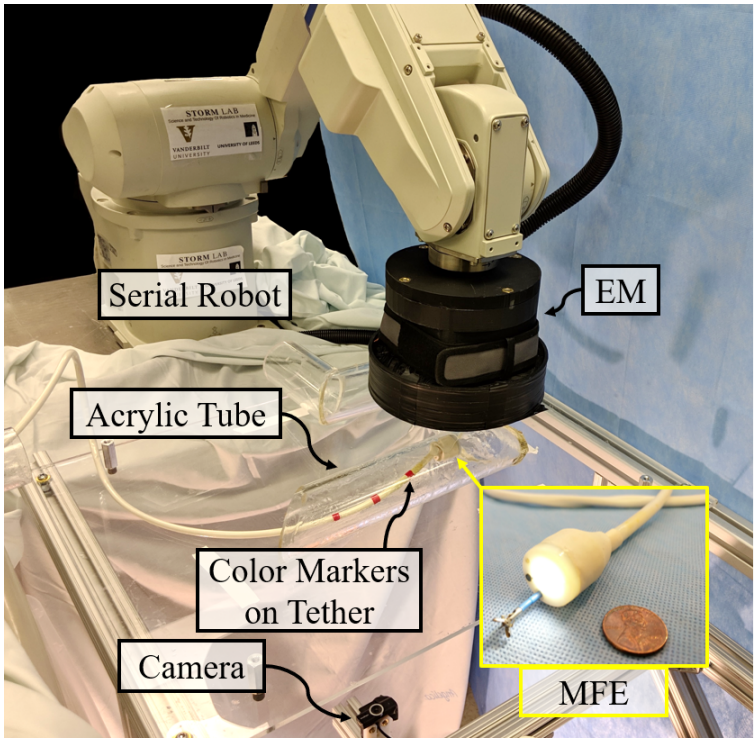

Figure 6.1: The MFE system with a camera used for color-marker detection. (©2019 IEEE [7])

Eq. (6.2).

$$
\begin{aligned}
\delta \mathbf{w}_c = \begin{bmatrix} \delta \mathbf{f}_m \\ \delta \tau_m \end{bmatrix} &= \begin{bmatrix} \frac{\partial \mathbf{f_m}}{\partial \mathbf{p}} & \frac{\partial \mathbf{f_m}}{\partial \hat{\mathbf{m}}_e} & \frac{\partial \mathbf{f_m}}{\partial \hat{\mathbf{m}}_i} \\ \frac{\partial \tau_\mathbf{m}}{\partial \mathbf{p}} & \frac{\partial \tau_\mathbf{m}}{\partial \hat{\mathbf{m}}_e} & \frac{\partial \tau_\mathbf{m}}{\partial \hat{\mathbf{m}}_i} \end{bmatrix} \begin{bmatrix} \delta \mathbf{p} \\ \delta \hat{\mathbf{m}}_e \\ \delta \hat{\mathbf{m}}_i \end{bmatrix} = \mathbf{J}_F \left(\begin{bmatrix} \delta \mathbf{p}_i \\ 0 \\ \delta \hat{\mathbf{m}}_i \end{bmatrix} + \begin{bmatrix} -\mathbf{I}_3 & 0 & 0 \\ 0 & \mathbf{I}_3 & 0 \\ 0 & 0 & 0 \end{bmatrix} \begin{bmatrix} \delta \mathbf{p}_e \\ \delta \hat{\mathbf{m}}_e \\ 0 \end{bmatrix} \right) \\
&= \mathbf{J}_F \begin{bmatrix} \delta \mathbf{p}_i \\ 0 \\ \delta \hat{\mathbf{m}}_i \end{bmatrix} + \mathbf{J}_F \begin{bmatrix} -\mathbf{I}_3 & 0 & 0 \\ 0 & \mathbf{I}_3 & 0 \\ 0 & 0 & 0 \end{bmatrix} \begin{bmatrix} \mathbf{I}_3 & 0 \\ 0 & S(\hat{\mathbf{m}}_e)^{\mathrm{T}} \end{bmatrix} \mathbf{J}_R \delta \mathbf{q} \\
&= \mathbf{J}_F \begin{bmatrix} \delta \mathbf{p}_i \\ 0 \\ \delta \hat{\mathbf{m}}_i \end{bmatrix} + \mathbf{J}_{FA} \delta \mathbf{q}
\end{aligned}
\tag{6.2}
$$

The serial robot's geometric Jacobian is indicated via $\mathbf{J}_R$, $\mathbf{I}_n$ indicates an identity matrix $\in \mathbf{R}^{n \times n}$, $S()$ denotes the skew-symmetric form of the cross-product operation, and $\delta \mathbf{q}$ is the vector of in-

finitesimal changes in joint positions. To actuate a magnetic device, the joint rates of the serial robot must be computed such that the result is a motion of the EM that induces the desired wrench. The commanded wrench is determined by applying a velocity and position controller as defined in Eq. (6.3).

$$\delta \mathbf{w}_c = \begin{bmatrix} (K_{p_{vel}} \mathbf{e}_v)\hat{\mathbf{t}} + K_{pos}\mathbf{e}_p \hat{\mathbf{n}} \\ K_{orient}\mathbf{e}_o \end{bmatrix} \tag{6.3}$$

Here, $\hat{\mathbf{t}}$ and $\hat{\mathbf{n}}$ indicate the tangent and normal directions, on the horizontal, to the desired trajectory, respectively. The velocity error is depicted via $\mathbf{e}_v = \dot{\mathbf{p}}_{i_{desired}} - \dot{\mathbf{p}}_i$, orientation error via $\mathbf{e}_o = \hat{\mathbf{m}}_i \times \hat{\mathbf{t}}$ where $\hat{\mathbf{t}}$ is the tangential direction to the desired path, and position error via $\mathbf{e}_p = \mathbf{p}_i - \mathbf{p}_i$. The commanded trajectory is made via a Bezier curve. This commanded wrench step is not a function of tether mechanics in any way; rather, it is the same relation one would use when commanding an untethered device. Given a desired step in wrench, an optimization relation is defined that favors achieving the commanded wrench, managing joint rates and joint-limit proximity [180], and maintaining a desired height of the EM; this relation is shown in Eq. (6.4). This is not a constrained minimization and relies on the subjective tuning of constants to give preference to the optimization of certain parameters over others.

$$\begin{aligned} \min_{\delta \mathbf{q}} \Big(& \left\| \mathbf{W}_w \left(\delta \mathbf{w}_c - \mathbf{J}_{FA} \delta \mathbf{q} \right) \right\|^2 + \alpha \left\| \mathbf{W}_{\mathbf{q}}^{-1} \delta \mathbf{q} \right\|^2 \ldots \\ & + \beta \left\| \left(\mathbf{z}_d - \mathbf{J}_{RZ} \delta \mathbf{q} \right) \right\|^2 \Big) \end{aligned} \tag{6.4}$$

Here, $\mathbf{W}_w$ is a diagonal weight matrix that allows for tuning the preference of achieving desired magnetic forces or torques, $\mathbf{W}_{\mathbf{q}}$ is a weight matrix that punishes joint motion as joints approach their limits, $\mathbf{z}_d = [0, 0, p_{e_{z-des}}, 0, 0, 0]^{\mathrm{T}}$ where $p_{e_{z-des}}$ is the desired EM height, and $\mathbf{W}_z$ is a matrix of zeros $\in \mathbf{R}^{6\times 6}$ apart from its $(3,3)$ index which is set to 1.0. Finally, $\mathbf{J}_R \in \mathbf{R}^{6\times 6}$ is the geometric Jacobian of the serial manipulator. The resultant joint rate is computed analytically and the command is sent to the robot controller. The resultant solution for commanded joint rates is shown

in Eq. (6.5).

$$\begin{aligned}\delta\mathbf{q} = &\left(\mathbf{J}_{FA}^{\mathrm{T}}\mathbf{W}_{w}\mathbf{J}_{FA} + 2\alpha\mathbf{W}_{\mathbf{q}}^{-1} + \beta\mathbf{J}_{RZ}^{\mathrm{T}}\mathbf{J}_{RZ}\right)^{-1}\ldots \\ &\left(\mathbf{J}_{FA}^{\mathrm{T}}\mathbf{W}_{w}\delta\mathbf{w}_{c} + \beta\mathbf{J}_{RZ}^{\mathrm{T}}\mathbf{z}_{d}\right)\end{aligned} \tag{6.5}$$

6.3.2 Estimation

The method proposed for the 2D local shape estimation of the MFE relies on fusing the following elements: (1) the sensed position and orientation of the MFE's tip, (2) the magnetic wrench that is applied on the MFE's tip, which is estimated using the dipole model, and (3) a dynamic model of the MFE's tip and body in a near vicinity of the tip (approximately 15 cm). A variant of the Kalman filter was chosen as the method of estimation as it is a recursive Bayesian estimator that requires a single integration of dynamics per time step. This particular model appears to be a sufficient representation for this application; however, it is not the only model that can be used, and is not necessarily the ideal one. In the following sections, the dynamic model and estimation method are described.

6.3.2.1 Dynamic Modelling

The proposed dynamic model consists of two disks, each rigidly connected to a link, with the links connected via a torsion spring; shown in Fig. 6.2. The following are descriptions of parameters used for dynamic modelling: m_i indicates the respective mass of disks where the pose of mass 1 corresponds to the pose of the MFE's tip, I_i indicates the moment of inertia of a respective disk, k_s is the torsion spring constant, L_i is the respective length of a link connected to mass m_i, b_i is a linear damping coefficient, and D_i is an angular damping coefficient. The states of the system consist of the MFE tip (m_1) position, linear velocity, orientation, and angular velocity, as well as the orientation and angular velocity of mass 2 (m_2). Feedback is available on the tip's pose and twist, but not on the state of m_2. These states are defined explicitly in Eq. (6.6) and Eq. (6.7).

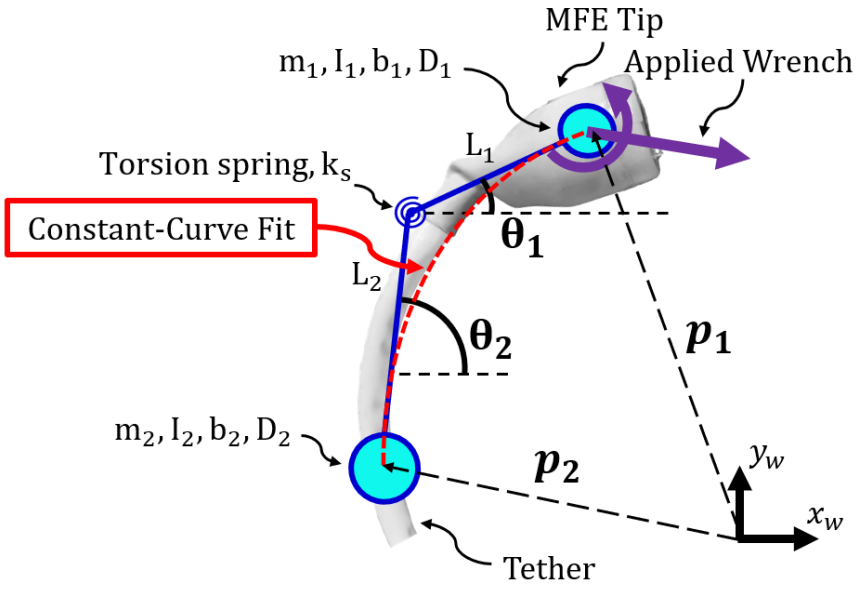

Figure 6.2: Schematic of a dynamic two-link and two-mass model with a best-fit curve with constant curvature. (©2019 IEEE [7])

$$\mathbf{x} = [\mathbf{p}_1, \dot{\mathbf{p}}_1, \theta_1, \dot{\theta}_1, \theta_2, \dot{\theta}_2]^{\mathrm{T}} \in \mathbf{R}^8 \tag{6.6}$$

$$\mathbf{y} = [\mathbf{p}_1, \dot{\mathbf{p}}_1, \theta_1, \dot{\theta}_1]^{\mathrm{T}} \in \mathbf{R}^6 \tag{6.7}$$

The dynamic model was written by deriving the system's Lagrangian that is shown in Eq. (6.8).

$$\begin{aligned} L = K - V = \frac{1}{2}\Big(& m_1 \dot{\mathbf{p}}_1^{\mathrm{T}} \dot{\mathbf{p}}_1 + m_2 \dot{\mathbf{p}}_2^{\mathrm{T}} \dot{\mathbf{p}}_2 \\ & + I_1 \dot{\theta}_1^2 + I_2 \dot{\theta}_2^2 - k_s (\theta_2 - \theta_1)^2 \Big) \end{aligned} \tag{6.8}$$

where

$$\mathbf{p}_2 = \mathbf{p}_1 - L_1 \begin{bmatrix} cos(\theta_1) \\ sin(\theta_1) \end{bmatrix} - L_2 \begin{bmatrix} cos(\theta_2) \\ sin(\theta_2) \end{bmatrix} \tag{6.9}$$

The Lagrangian expression in Eq. (6.8) was derived symbolically using Matlab (Mathworks Inc., USA) via Eq. (6.10) and compiled into a Python library, which was then interfaced-with using a

ROS node.

$$\frac{d}{dt}\frac{\partial L}{\partial \dot{g}_{c_i}} - \frac{\partial L}{\partial g_{c_i}} - n.c. = 0 \tag{6.10}$$

Here, g_{c_i} denotes the i_{th} of the four generalized coordinates (p_{1x}, p_{1y}, θ_1, θ_2, where $\mathbf{p}_1 = [p_{1x}, p_{1y}]^{\mathrm{T}}$), and "n.c." denotes the non-conservative forces applied on the system that include linear and angular viscous friction (each applied on both masses), and externally applied magnetic forces and torques. Eq. (6.10) was then solved for each $\ddot{g}_{c_i}$ to write a nonlinear state-transition expression as shown in Eq. (6.11). Here, $\mathbf{w}_m$ indicates the applied magnetic wrench that is estimated via dipole model; this is possible owing to localization feedback of IM pose and kinematic feedback of the serial manipulator that is used to obtain EM pose. The complete expression for $\ddot{g}_{c_i}$ is omitted here for brevity.

$$\mathbf{x}_k = \mathbf{x}_{k-1} + \dot{\mathbf{x}}_{k-1}\delta t = \mathbf{g}(\mathbf{x}_{k-1}, \mathbf{w}_m) \tag{6.11}$$

Here, $\mathbf{g}(\mathbf{x}_{k-1}, \mathbf{w}_m)$ indicates the nonlinear state-transition matrix. The expression for the measurement model, $\mathbf{h}(\mathbf{x}_{k-1})$, is shown in Eq. (6.7). The measurement, $\mathbf{z}_k$, is identical to the measurement model and is obtained using a magnetic localization method described in Ref. [53] that provides six DoF pose feedback; velocities are obtained via discrete low-pass-filtered differentiation. As the estimate is 2D, 2 DoFs of position feedback and 1 DoF of orientation feedback are utilized. The objective of this estimator is to recover the value of θ_2 and to use it to make a continuum-shape estimate. The functionality of the estimator can be conceptualized with the following question: "*what is the state of the model that would result in the unexpected deflection that was observed?*". The possibility of this estimation is contingent on the observability of the state vector. As this system is nonlinear, the local observability is determined and is done by linearizing the state-transition and measurement models and verifying the rank of the observability matrix $\mathbf{O}$ to be that of the number of system states, as defined in Eq. (6.12) [181], where "n" denotes the number of system states. This model is locally observable and remains observable when the only feedback information is

the location of $\mathbf{p}_1$.

$$\mathbf{O}(\mathbf{x},\mathbf{u}) = \begin{bmatrix} \frac{\partial \mathbf{h}}{\partial \mathbf{x}}(\mathbf{x}) \\ \frac{\partial \mathbf{h}}{\partial \mathbf{x}}(\mathbf{x})\frac{\partial \mathbf{g}}{\partial \mathbf{x}}(\mathbf{x},\mathbf{u}) \\ \vdots \\ \frac{\partial \mathbf{h}}{\partial \mathbf{x}}(\mathbf{x})\frac{\partial \mathbf{g}}{\partial \mathbf{x}}(\mathbf{x},\mathbf{u})^{n-1} \end{bmatrix} \tag{6.12}$$

6.3.2.2 Estimator Implementation

The prediction step of the EKF relies on using the dynamic model to obtain an *a priori* state and state error covariance; these are marked via $\bar{\mathbf{x}}_k$ and $\bar{\mathbf{P}}_k$, respectively. These relations are shown in Eq. (6.13) and Eq. (6.14), where $\mathbf{Q}_k$ is the process noise covariance and $\mathbf{P}_{k-1}$ is the state error covariance.

$$\bar{\mathbf{x}}_k = \mathbf{g}(\mathbf{x}_{k-1}, \mathbf{w}_m) \tag{6.13}$$

$$\bar{\mathbf{P}}_k = \frac{\partial g(\mathbf{x}_{k-1})}{\partial \mathbf{x}} \mathbf{P}_{k-1} \frac{\partial g(\mathbf{x}_{k-1})}{\partial \mathbf{x}}^{\mathrm{T}} + \mathbf{Q}_k \tag{6.14}$$

The correction step of the EKF relies on using *a priori* state as predicted via dynamic model and fusing the prediction with sensory information to obtain an *a posteriori* state update. These relations are shown in Eq. (6.15), Eq. (6.16), and Eq. (6.17), where $\mathbf{R}_k$ is the measurement covariance. The Kalman gain, $\mathbf{K}_k$, acts as a weight of confidence between the dynamic model and state measurement.

$$\mathbf{K}_k = \bar{\mathbf{P}}_k \frac{\partial h(\bar{\mathbf{x}}_k)}{\partial \mathbf{x}}^{\mathrm{T}} \left(\frac{\partial h(\bar{\mathbf{x}}_k)}{\partial \mathbf{x}} \bar{\mathbf{P}}_k \frac{\partial h(\bar{\mathbf{x}}_k)}{\partial \mathbf{x}}^{\mathrm{T}} + \mathbf{R}_k \right)^{-1} \tag{6.15}$$

$$\mathbf{x}_k = \bar{\mathbf{x}}_k + \mathbf{K}_k \Big(\mathbf{z}_k - h(\bar{\mathbf{x}}_k) \Big) \tag{6.16}$$

$$\mathbf{P}_k = \Big(\mathbf{I} - \mathbf{K}_k \frac{\partial h(\bar{\mathbf{x}}_k)}{\partial \mathbf{x}} \Big) \bar{\mathbf{P}}_k \tag{6.17}$$

Finally, a curve with a constant radius is fitted to the masses such that it is tangent to the heading of mass 1, and passes through the position of mass 2. A constant curvature arc was chosen owing to the low number of DoFs that can dictate shape. This results in an assumption of a constant bending along the arc. Although the assumption does not result in optimal shape accuracy; however, it

provides an estimate that may be more valuable than no estimate at all.

6.3.2.3 Model Parameters

The selection of parameter values for the proposed dynamic model presents a unique problem owing to the disconnect in the mechanics of the model and the physical system. Typically continuum robots are modelled with a known base, while the system consists of a known tip onto which an actuating wrench is applied. The model does not accurately depict the phenomenon of a long tether being dragged, but rather can usefully depicts local mechanics. Firstly, a torsional spring constant was chosen. An experimental setup was devised to estimate the torsional spring constant that exists at the tip of the MFE (Fig. 6.3). A set of 10 experiments was conducted where a serial arm with a force sensor at its end-effector was used to deflect the tip of the MFE; this resulted in a torsional spring constant of 0.033 ± 0.005 Nm/rad. This value over-estimates the true constant as the tether would translate when a force would be applied at the tip. This constant was scaled by 0.5 in simulations and by 0.3 in platform experiments; values that were chosen based on observed performance. The rest of dynamic parameters were subjectively chosen based on observing the estimated state: disk-radii $r_1 = 0.02$ and $r_2 = 0.02$, link lengths $L_1 = 0.02$ and $L_2 = 0.08$, masses $m_1 = 0.05kg$ and $m_2 = 0.4kg$, linear damping coefficients $b_1 = 0.005$ and $b_2 = 0.001\ N \cdot s/m$, angular damping coefficients $D_1 = 0.005$ and $D_2 = 0.05\ N \cdot m \cdot s$.

The measurement covariance matrix $\mathbf{R}_k$ was defined based on localization error variance as computed in Ref. [53]; the linear position noise was up to 5 mm while the angular position noise was up to 6.0°. The process noise covariance was set to an diagonal matrix with identical components of a value of 0.2. The estimator may lag when the values are too small (a thousandth of that which was chosen). The performance of the estimator does not appear to be sensitive to this covariance value once a threshold in magnitude is reached. The state covariance was initialized to be a diagonal matrix with small values.

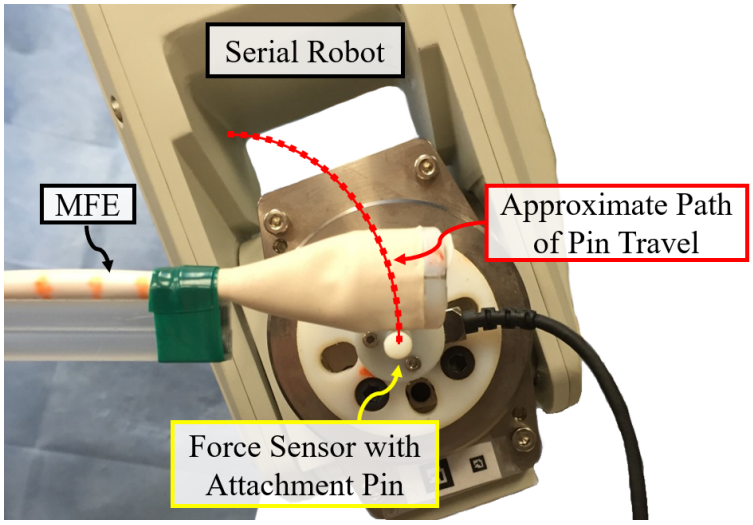

Figure 6.3: Experimental setup for evaluating torsion spring constant of the tip of the MFE. Shown is the approximate trajectory that the end-effector of the serial robot followed.

6.4 Validation

6.4.1 Validating the Estimated Shape

To validate the proposed estimation technique, experiments were conducted in simulation as well as on a physical platform. The position-sensor points in simulation and on the physical platform were placed in approximately the same position on the MFE: at 6 cm, 10 cm, and 14.5 cm along the tether length. As the number of position sensors available to us on the physical platform was limited, an error metric was developed that relies on measuring the distance between each sensor point and the nearest point on the estimated curve. This error metric, e_{est}, is defined in Eq. (6.18).

$$e_{est} = \frac{1}{y}\sum_{i=2}^{y}\frac{\|\mathbf{p}_{s_i} - \mathbf{p}_{m_i}\|}{d_i} \tag{6.18}$$

where $\mathbf{p}_{s_i}$ is the sensor position, $\mathbf{p}_{m_i}$ is the nearest model point to $\mathbf{p}_{s_i}$, y is the number of position sensor points (1 localization sensor at tip, 3 position sensors along tether shape, 4 total); the sensor points start at 2 as the tip of the model is a known sensory feedback, while the rest of the model shape is unknown. The error term contains a normalization that is implemented via a quotient of d_i; as a point closer to the tip has a smaller error (model tip is given via pose sensor), a small error

near the tip may carry the same amount of information as a much larger error farther away from the tip. The value of d_i is the nominal distance of the sensed point along the body of the endoscope. The estimates in this work were discretized to 40 points and thus the point closest to the respective nominal was chosen.

To evaluate performance, the estimate is compared with a "baseline estimate" assumption where the tether is assumed to be straight behind the tip. This baseline comparison is used as the critical parameter to be estimated is the direction on which the tether lies behind the tip. Knowledge of the side of the IM the tether is on gives insight into the direction of wrench disturbance it will induce on motion. The precise knowledge of the exact shape is not critical, nor is the ability to fully recover the exact shape expected. For this baseline estimate the error metric, Eq. (6.18), was also computed and is referred to via $e_{baseline}$. Although e_{est} itself captures the estimation error, a comparison with $e_{baseline}$ demonstrates the validity of the estimation method when the tether is curved.

6.4.1.1 Simulation Study

Two experiments were conducted, 10 trials each, in simulation. In each experiment, the MFE was commanded to autonomously follow a trajectory using velocity control in the tangential direction to the path, and position control in the normal direction to the path. A 6 mm Gaussian noise was applied to localization information via a plugin. The total length of the tether used in simulation was 45 cm and the length of the sensed portion of the tether was 14.6 cm. The trajectory in the first experiment was a double-bend curve (segment lengths: 13, 18, 20 cm) and in the second, it was a sinusoidal (0.4 m length, 0.05 amplitude, single period). These trajectories and the measured, estimated, and baseline shapes are shown in Fig. 6.4. The double-bend-trajectory experiment resulted in $e_{baseline} = 0.95 \pm 0.03$ and $e_{est} = 0.26 \pm 0.02$. The sinusoidal-trajectory experiment resulted in $e_{baseline} = 0.54 \pm 0.01$ and $e_{est} = 0.21 \pm 0.01$. The results are shown in Fig. 6.5 and Fig. 6.6 using box plots. The regions of higher error correspond to regions of tether deflection caused by the MFE passing through a bend. To validate the evaluate the effect of environmental

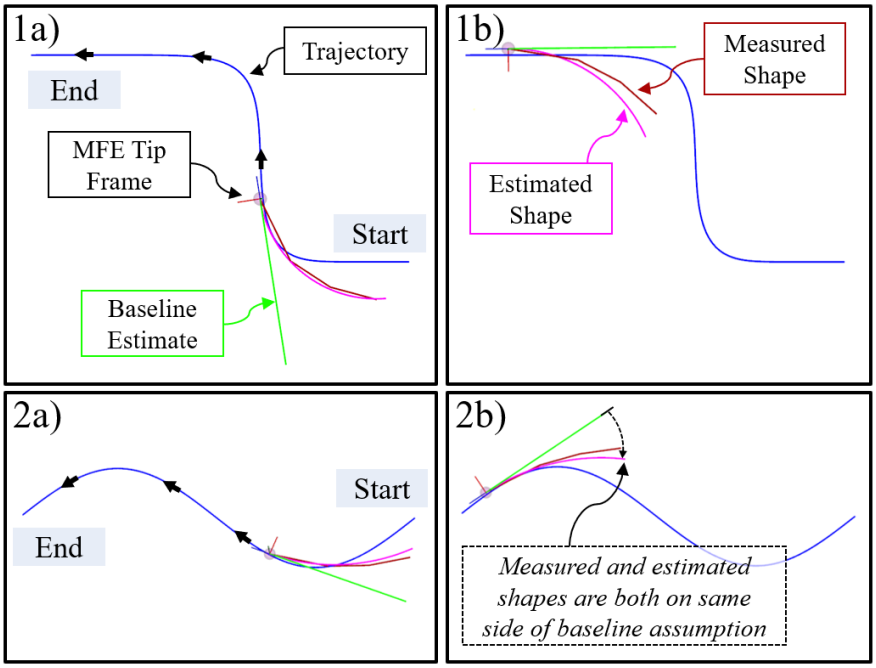

Figure 6.4: Trajectories that the MFE was commanded to follow during simulation experiments. Trajectory 1 (a,b) consists of two-bend path, and trajectory 2 (a,b) consists of a sinusoidal path. (©2019 IEEE [7])

friction on the method, the friction of the simulation model was increased by a factor of 5 (from 0.1 to 0.5) while all other model parameters were unchanged which resulted in the following errors: $e_{baseline} = 1.00 \pm 0.04$ and $e_{est} = 0.37 \pm 0.03$. For reference, Terry et al. reported a coefficient of friction of 0.016 ± 0.002 *in vivo* between tissue and polycarbonate [182].

6.4.1.2 Experiments on a Physical Platform

The physical platform trials were conducted with the MFE being teleoperated along a single-bend trajectory (segments: 11 cm, 10 cm). Teleoperation here refers to a the EM being directly commanded via joystick and it was used rather than autonomous control owing to the high-friction environment of the acrylic tube that resulted in the autonomous controller applying too much vertical force. The use of sufficient lubricant resulted in difficulties with visual detection of color-markers. The operator pushed the proximal portion of the tether to facilitate advancement of the MFE, as the proximal portion of the tether was outside of the experimental tube. The operator made

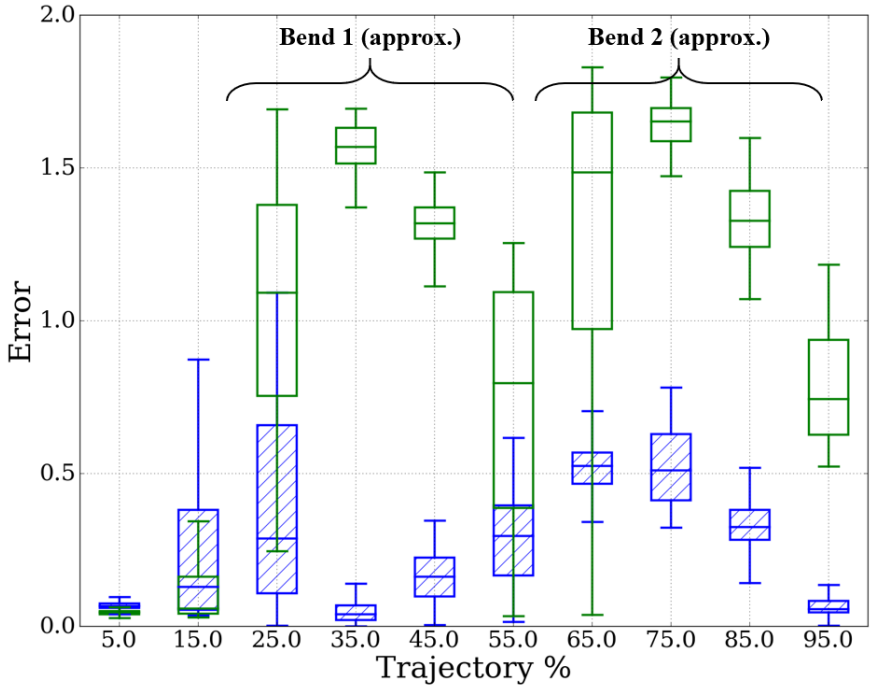

Figure 6.5: Experimental results for the double-bend simulation trajectory. The green indicates $e_{baseline}$ results and the blue indicates e_{est} results. (©2019 IEEE [7])

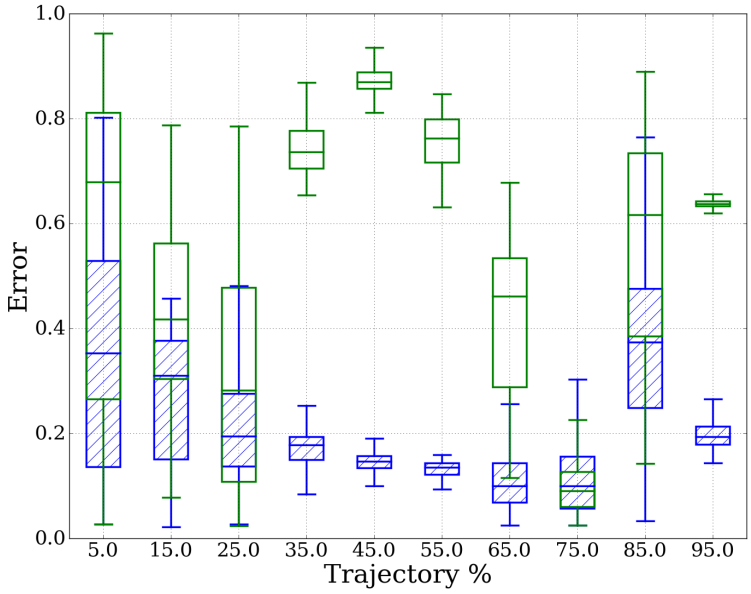

Figure 6.6: Experimental results for the sinusoidal simulation trajectory. The green indicates $e_{baseline}$ results and the blue indicates e_{est} results. (©2019 IEEE [7])

contact with the tether at an approximate distance of 70 to 100 cm from the tip of the tether, thus, this contact had no effect on the steering of the endoscope. Furthermore, during clinical use, an operator is expected to manually insert tether (not to push the MFE, but rather minimize resistance in magnetic pull). The use of teleoperation is not clinically relevant but it allowed for the evaluation of the estimation algorithm. In the case of a color marker being occluded, the measurement node did not send a data update. Model errors were not computed if a measurement was older than 0.2 s.

As the estimation algorithm is a stand-alone program independent of magnetic CL control, shape estimation was carried out in the same manner as during simulation trials. As a human was in-the-loop, the estimated shape of the MFE was not displayed during the recording of data to prevent a bias in attempting to steer the estimate. An example camera-view and trajectory path is shown in Fig. 6.7. The experiment resulted in $e_{baseline} = 1.06 \pm 0.05$ and $e_{est} = 0.87 \pm 0.07$. The results are displayed via a box plot in Fig. 6.8. The error reduction is significantly smaller in platform trials when compared to the simulation trials; however, it is evident that the estimate outperforms the baseline in the bend region. It should be noted that the error reported here is for the entire trajectory and thus a high error outside of the bend region, for both the estimate and baseline, result in a bias on the reported values. The higher overall errors, as compared to simulation, may be caused by the high friction between the material of the tip of the MFE (35D Pebax/Propell) and acrylic which could not be sufficiently lubricated owing to the difficulty of image processing to track tether colors. Although the operator pushed the tether from a significant distance from the tip of the MFE, the effect of pushing may have added additional variability.

6.4.2 Validating the use of Estimated States in Control

The following simulation experiments demonstrate the use of the estimated state in the magnetic control loop. The spring angle was used to pass an additional torque term to the magnetic controller and the influence of this term on heading error was evaluated. The key benefit of this controller is that it applies a torque to compensate for tether disturbance even when the IM heading error is null. The MFE is tasked with traversing the double-bend curve (Section 6.4.1.1, shown in

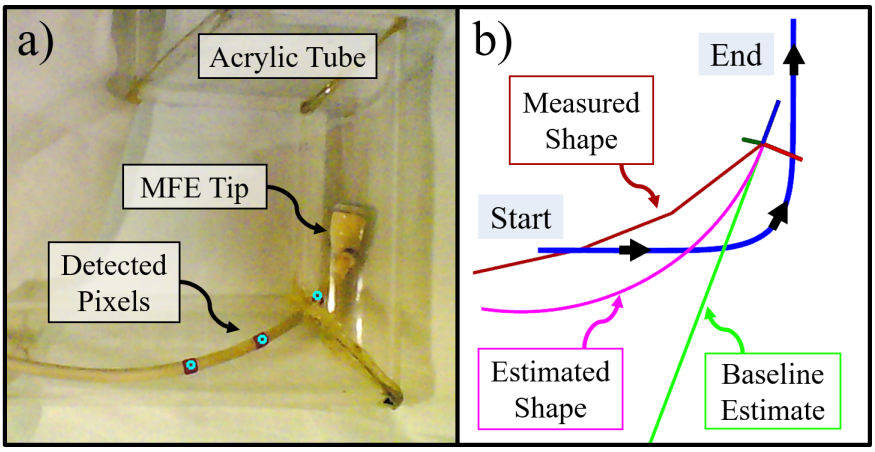

Figure 6.7: (a) A sample view from the camera used for tether shape measurement and (b) the trajectory followed by a teleoperated MFE. (©2019 IEEE [7])

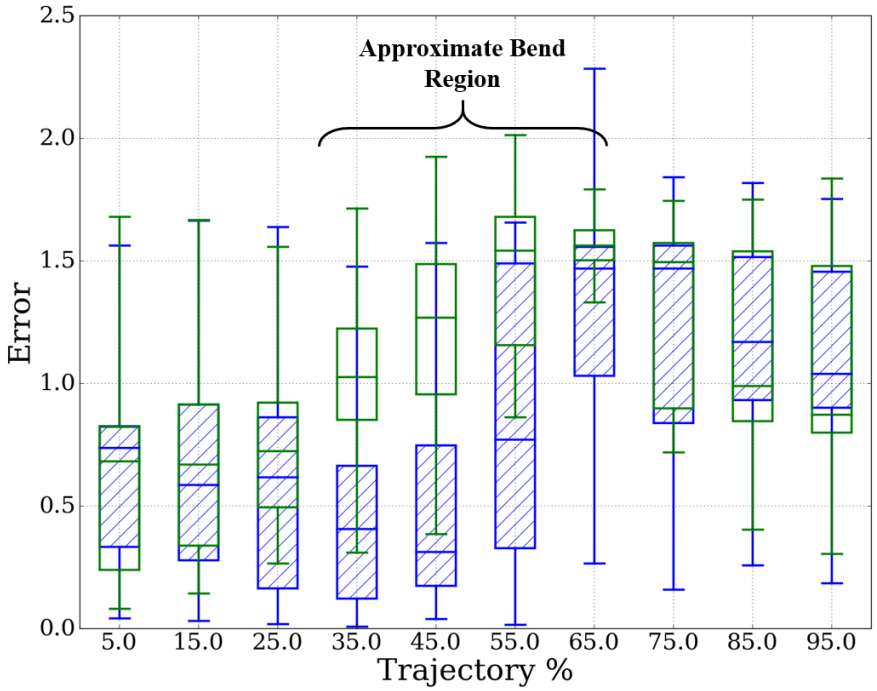

Figure 6.8: Experimental results for the single-bend platform trajectory. The green indicates $e_{baseline}$ results and the blue indicates e_{est} results. (©2019 IEEE [7])

Fig. 6.4(1a,1b)). The magnetic wrench command is augmented from that described in Eq. (6.3) to that shown in Eq. (6.19). Here, the spring angle is given by $\theta_2 - \theta_1$ and K_{p_s} is a user-defined

constant.

$$\begin{aligned}\delta\mathbf{w}_{est} &= \delta\mathbf{w}_c + \delta\mathbf{w}_{spring} \\ &= \begin{bmatrix} (K_{p_{vel}}\mathbf{e}_v)\hat{\mathbf{t}} + K_{pos}\mathbf{e}_p\hat{\mathbf{n}} \\ K_{orient}\mathbf{e}_o \end{bmatrix} + [0,0,0,0,0,-K_{p_s}k_s(\theta_2-\theta_1)]^{\mathrm{T}}\end{aligned} \tag{6.19}$$

The torque compensation term, $\delta\mathbf{w}_{spring}$, was only applied when the spring torque would reduce heading error. This expression is then used in Eq. (6.5) to compute robot joint commands. Instances occurred where the estimator predicted the tether to be on the wrong side of the true measurement. Adding a torque in such a case may result in error divergence. It should be noted that simply increasing heading-control gains may demonstrate similar improvements; however, increasing heading control gains influences the ability to control position as, in terms of control, the position and orientation of the IM are coupled. In other words, constantly applying high orientation control gains will induce a system preference for reducing heading error, at the expense of position control.

Ten simulation experiments were conducted with $\delta\mathbf{w}_{spring}$, and ten without this torque-compensation term. The mean heading errors without and with compensation, respectively, were $11.8\pm1.7^\circ$ and $7.6\pm1.0^\circ$; a 35% improvement. The respective position errors, normal to the path, were $3.8\pm0.5^\circ$ and $4.6\pm0.5^\circ$. The position errors were small in both cases considering the total trajectory length was approximately 0.5 m. The slight increase in position error when using torque-compensation is likely due to the magnetic controller giving preference to applying magnetic torque over force which has a slight adverse effect on translation control. A box plot with trajectory errors displayed may be seen in Fig 6.9. Further work is needed to investigate the possibility of force-compensation.

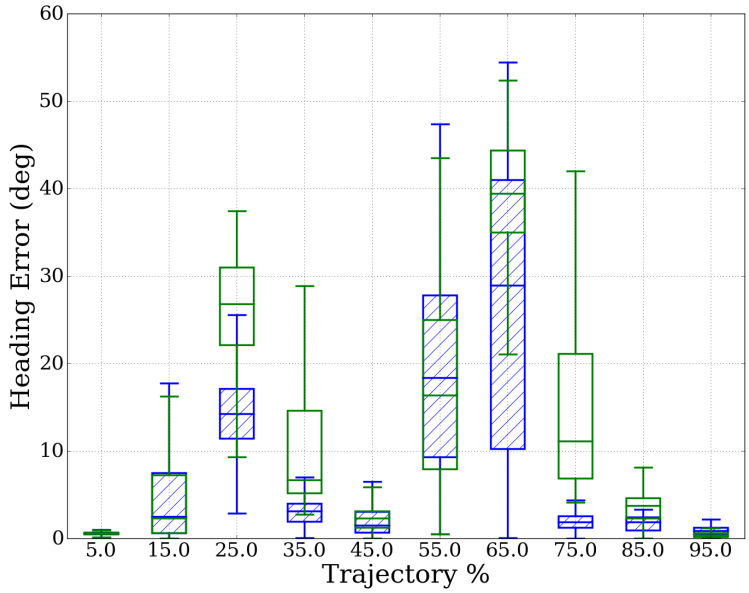

Figure 6.9: Simulation experiment results that demonstrate the effect of spring-torque compensation. The MFE heading error, as projected on the horizontal, is shown in green when normal orientation control is used and in blue when spring-torque compensation is used.

6.5 Conclusions and Future Work

This chapter contains a discussion on the sensorless estimation of the distal shape of a tip-actuated tethered endoscope with the aim of using estimate information for computed torque control. This work enables the observation of the mechanical disturbance wrench that the tether applies on a device. A method for the 2D dynamic modelling of the MFE was presented. As the method does not rely on the use of auxiliary sensors on the endoscope to recover shape information, an extended Kalman estimator is applied to obtain unknown model configuration values. The estimator is validated by comparing its ability to estimate the distal shape of the MFE. In simulation and platform trials, it was shown that the estimator successfully estimates the direction of the tether with respect to the heading of the tip. A further validation demonstrated that the estimated state of the dynamic model can be used in magnetic control; in a simulated experiment, the heading error of the MFE was decreased when using information from the estimator.

This work contains limitations that may be addressed in future work: (1) The estimation method is limited in that its performance is subject to random disturbances. It is possible for the estimator to be wrong if the environment applies a larger disturbance; however, the estimate is expected to correct over time. The implications of potential estimation errors in magnetic control are yet to be evaluated. (2) Owing to the mechanical disparity between the 2D dynamic model and the true tether mechanics, this work lacks a robust methodology for choosing dynamic model parameters. A system-specific subjective choice of parameters may be acceptable as this parameter choice must occur only once per estimated device. A more precise approach may involve the recording of a large data set of measured shape changes as induced via known applied wrenches. Given these same wrenches, a regression approach may be used to fit the dynamic model's parameters. This may be useful for reducing estimation error, but is not necessary for the use of the proposed method.

In summary, the proposed dynamic modelling and estimation are a valid method for estimating the disturbance wrench that is applied by the compliant tether body on the tip of an endoscope. The method can be used to both estimate the local distal shape of a tip-actuated endoscope, and estimation parameters can be used in the device's controller for improving performance. Further work is needed to evaluate the feasibility of full computed-torque control; however, the preliminary results presented here suggest feasibility.

Chapter 7

Conclusions

This dissertation presented actuation concepts and applications related to mobile-dipole magnetic actuation of endoscopic devices. The mobile-dipole actuation strategy is feasible for endoscopic screening and intervention. A permanent magnet that is moved in space using a serial robot has the benefits of small magnetic form factor for high strength, a large magnetic workspace, multiple DoF control, a relatively low cost-to-workspace ratio, and portability. The magnetic endoscopy system proposed in this dissertation, the MFE, may potentially be made to be disposable as the use of magnetic fields does not necessitate a complex mechanism for actuation; a limiting factor may be the cost of the imaging module. The work presented in this dissertations includes an investigation of: CL control and singularities of a mobile-dipole actuation system, the use of autonomy for clinical tasks, the influence of localization uncertainty on magnetic force uncertainty, and the use of computed-torque control of a tip-actuated tethered robot.

The contributions of this dissertation to the field are the following: (1) an analysis of magnetic wrench singularities in mobile-dipole actuation where no assumptions are made on the alignment of the IM's heading, (2) the co-development of the first magnetic CL control system where all methods used are clinically relevant, (3) the development and *in vivo* validation of the first instances of task autonomy in robotic magnetic endoscopy, i.e. retroflexion and EUS servoing, (4) the development of the first EUS servoing system that does not rely on mechanical connection for probe actuation, (5) the proposal of an algorithm for reducing magnetic force uncertainty in magnetic CL control systems where the localization of the IM is subject to uncertainty, (6) the proposal of a probabilistic approach for estimating the wrench disturbance applied by a tether on a tip-actuated endoscopic robot to enable computed-torque control. These contributions have addressed knowledge gaps in the field; however, further work is necessary to achieve clinical translation of the technology.

Investigations in this dissertations included a consideration of inefficiencies in mobile-dipole control approaches. First, an EM velocity-wrench bound was described. A limitation on EM velocity, which is desired in proximity to a patient, prevents the application of any magnetic wrench on the IM. This constraint on the output exists as the wrench results from a unique configuration of the EM and IM. This effect may result in control delays that may require further consideration of path-planning. Second, effective rotation axes were investigated when implementing a retroflexion algorithm for the MFE. Given an EM configuration and a desired heading of the IM, it may be beneficial to rotate an IM in a direction that does not define the shortest angular path to its desired heading in order to apply a higher magnitude of torque. This is due to the inability to instantaneously change the directions of applied field in permanent magnet systems. This path-efficiency concept results in a potential of planning indirect motion paths that may be more effective for overcoming environmental disturbances. In future work, considerations such as energy minimization and path-efficiency may be integrated into control algorithms to improve IM motion efficacy and minimize the amount of translation and rotation that an EM must undergo to apply an IM control task.

Task autonomy (Level 2 autonomy [59]) was investigated for endoscope retroflexion and GI US servoing. This dissertations contains the first works in task autonomy for robotic endoscopy. Both applications were demonstrated in benchtop and *in vivo* trials. The algorithms were implemented to reduce the reliance on an operator to complete manual control tasks. In the case of both applications, the manual control tasks were not intuitive for an operator. Supplanting manual control with task autonomy may reduce the cognitive burden of an operator and enable them to focus attention on diagnostics. The studies presented in this dissertation suggest that autonomy has a future in robotic endoscopy. Other tasks that may be investigated in the future include translation through an entire lumen as well as identification and image-centering of a lesion to facilitate targeted biopsy. Higher levels of autonomy may be investigated in the future by expanding the GI US servoing work of this dissertation. Machine learning techniques may be employed for lesion characterization. A first step in this direction may be the autonomous measuring of tissue thickness

which, it itself, may indicate disease [110].

The use of model-based control of tip-actuated tethered endoscopes was investigated as the tether of the MFE provided significant motion disturbance. In order to maintain a low cost and simple design of the MFE, a sensorless, probabilistic, approach was employed with a goal of capturing the disturbance wrench that the tether imparts. Solving for the disturbance wrench is non-trivial as the environment imparts significant disturbances on motion as well. An extended Kalman filter with a dynamic model was used to estimate the configuration of the model that, in turn, gives insight on wrench disturbance. The disturbance torque was used to impart a compensation torque in a trajectory controller. The proposed method was also demonstrated for the sensorless shape estimation of the distal portion of the MFE. In future work, the proposed method may be extended to a full inverse-dynamic control. This is likely to assist with the aforementioned issues of control inefficiency.

In conclusion, the mobile-dipole actuation approach is feasible and, with further investigation, may provide for a robust method of diagnostic endoscopy. Further investigations of task autonomy, path planning, and dynamics-based control may improve the efficacy system mobility. Auxiliary imaging methods, e.g. US, may be used to enhance diagnostic functionality. This technology may enhance operator experience as the robotic system offers a mechanically decoupled actuation system, e.g. electrical inputs result in endoscope motion, and task autonomy. User experience may be improved as the device induces small amounts of tissue stress which are likely to apply little discomfort for a patient, potentially removing the use of sedation from the standard procedure.

BIBLIOGRAPHY

[1] Addisu Z. Taddese, Piotr R. Slawinski, Keith L. Obstein, and Pietro Valdastri. Closed loop control of a tethered magnetic capsule endoscope. In *Proc. 2016 Robotics: Sci. and Syst.*, AnnArbor, Michigan, USA, 2016.

[2] Addisu Z Taddese, Piotr R Slawinski, Keith L Obstein, and Pietro Valdastri. Nonholonomic Closed-loop Velocity Control of a Soft-tethered Magnetic Endoscope. In *IEEE/RSJ Int. Conf. Intell. Robot. Syst. (IROS 2016)*, Daejeon, South Korea, 2016.

[3] Piotr R Slawinski, Addisu Z Taddese, Kyle B Musto, Keith L Obstein, and Pietro Valdastri. Autonomous retroflexion of a magnetic flexible endoscope (©2017 ieee. reprinted, with permission, 07/2017). *IEEE Robotics and Automation Letters*, 2(3):1352–1359, 2017.

[4] Piotr R. Slawinski, Nabil Simaan, Addisu Z. Taddese, Keith L. Obstein, and Pietro Valdastri. Sensitivity ellipsoids for force control of magnetic robots with localization uncertainty (©2019 ieee. reprinted, with permission, 06/2019) *(In-Press)*. *IEEE Transactions on Robotics*, 2019.

[5] Piotr R Slawinski, Addisu Z Taddese, Keith L Obstein, and Pietro Valdastri. *Encyclopedia of Medical Robotics: Minimally invasive surgical robotics, Chapter 17: Robotic Capsule Endoscopy*. World Scientific, Singapore, 2017.

[6] Piotr R Slawinski, Collin T Garcia, Addisu Z Taddese, Keith L Obstein, and Pietro Valdastri. Towards recovering a lost degree of freedom in magnet-driven robotic capsule endoscopy (asme: reprinted with permission). In *2017 Design of Medical Devices Conference*, pages V001T08A011–V001T08A011. American Society of Mechanical Engineers, 2017.

[7] Piotr R Slawinski, Nabil Simaan, Keith L Obstein, and Pietro Valdastri. Sensorless estimation of the planar distal shape of a tip-actuated endoscope (©2019 ieee. reprinted, with permission, 06/2019) *(In press)*. 2019.

[8] GT Gillies, RC Ritter, WC Broaddus, MS Grady, MA Howard III, and RG McNeil. Magnetic manipulation instrumentation for medical physics research. *Review of Scientific Instruments*, 65(3):533–562, 1994.

[9] Federico Carpi and Carlo Pappone. Stereotaxis niobe® magnetic navigation system for endocardial catheter ablation and gastrointestinal capsule endoscopy. *Expert review of medical devices*, 6(5):487–498, 2009.

[10] Bich Lien Nguyen, Jose L Merino, and Eli S Gang. Remote navigation for ablation procedures–a new step forward in the treatment of cardiac arrhythmias. *European Cardiology*, 6(3):50–56, 2010.

[11] Christophe Chautems, Burak Zeydan, Samuel Charreyron, George Chatzipirpiridis, Salvador Pané, and Bradley J Nelson. Magnetically powered microrobots: a medical revolution underway? *European Journal of Cardio-Thoracic Surgery*, 51(3):405–407, 2017.

[12] Zhuan Liao, Xi Hou, En-Qiang Lin-Hu, Jian-Qiu Sheng, Zhi-Zheng Ge, Bo Jiang, Xiao-Hua Hou, Ji-Yong Liu, Zhen Li, Qi-Yang Huang, et al. Accuracy of magnetically controlled capsule endoscopy, compared with conventional gastroscopy, in detection of gastric diseases. *Clinical Gastroenterology and Hepatology*, 14(9):1266–1273, 2016.

[13] P. R. Slawinski, K. L. Obstein, and P. Valdastri. Emerging issues and future developments in capsule endoscopy. *Techniques in Gastrointestinal Endoscopy*, 17(1):40–46, 2015.

[14] Piotr R Slawinski, Keith L Obstein, and Pietro Valdastri. Capsule endoscopy of the future: Whats on the horizon? *World Journal of Gastroenterology: WJG*, 21(37):10528, 2015.

[15] Lisandro Leon, Frank M Warren, and Jake J Abbott. Optimizing the magnetic dipole-field source for magnetically guided cochlear-implant electrode-array insertions. *Journal of Medical Robotics Research*, 3(01):1850004, 2018.

[16] Nabil Simaan, Rashid M. Yasin, and Long Wang. Medical technologies and challenges of robot-assisted minimally invasive intervention and diagnostics. *Annual Review of Control, Robotics, and Autonomous Systems*, 1(1):465–490, 2018.

[17] Taoming Liu, Russell Jackson, Dominique Franson, Nate Lombard Poirot, Reinhardt Kam Criss, Nicole Seiberlich, Mark A Griswold, and M Cenk Çavuşoğlu. Iterative jacobian-based inverse kinematics and open-loop control of an mri-guided magnetically actuated steerable catheter system. *IEEE/ASME Transactions on Mechatronics*, 22(4):1765–1776, 2017.

[18] Jacky Shui Ho Chan, Amelia Chien Wei Chao, Vincent Chi Ho Cheung, Sophia Sau Kuen Wong, Whitney Tang, Justin Che Yuen Wu, Henry Lik Yuen Chan, Francis Ka Leung Chan, Joseph Jao Yiu Sung, and Siew Chien Ng. Gastrointestinal disease burden and mortality: A public hospital-based study from 2005 to 2014. *Journal of gastroenterology and hepatology*, 2018.

[19] Anne F Peery, Seth D Crockett, Alfred S Barritt, Evan S Dellon, Swathi Eluri, Lisa M Gangarosa, Elizabeth T Jensen, Jennifer L Lund, Sarina Pasricha, Thomas Runge, et al. Burden of gastrointestinal, liver, and pancreatic diseases in the united states. *Gastroenterology*, 149(7):1731–1741, 2015.

[20] Béatrice Lauby-Secretan, Nadia Vilahur, Franca Bianchini, Neela Guha, and Kurt Straif. The iarc perspective on colorectal cancer screening. *New England Journal of Medicine*, 378(18):1734–1740, 2018.

[21] Keith L Obstein and Pietro Valdastri. Advanced endoscopic technologies for colorectal cancer screening. *World journal of gastroenterology: WJG*, 19(4):431, 2013.

[22] Linda Rabeneck, Lawrence F Paszat, Robert J Hilsden, Refik Saskin, Des Leddin, Eva Grunfeld, Elaine Wai, Meredith Goldwasser, Rinku Sutradhar, and Therese A Stukel. Bleeding

and perforation after outpatient colonoscopy and their risk factors in usual clinical practice. *Gastroenterology*, 135(6):1899–1906, 2008.

[23] Jason Ferreira, Mona Akbari, Laurie Gashin, Garret Cullen, Alan Moss, Daniel A Leffler, Mark Aronson, and Adam S Cheifetz. Prevalence and lifetime risk of endoscopy-related complications among patients with inflammatory bowel disease. *Clinical Gastroenterology and Hepatology*, 11(10):1288–1293, 2013.

[24] Meinhard Classen, Guido NJ Tytgat, Charles J Lightdale, Jacques JGJM Bergman, and Douglas G Adler. *Gastroenterological endoscopy*. Thieme Stuttgart, New York, 2002.

[25] Boris Vucelic, Douglas Rex, Roland Pulanic, Jorge Pfefer, Irena Hrstic, Bernard Levin, Zamir Halpern, and Nadir Arber. The aer-o-scope: proof of concept of a pneumatic, skill-independent, self-propelling, self-navigating colonoscope. *Gastroenterology*, 130(3):672–677, 2006.

[26] Felice Cosentino, Emanuele Tumino, Giovanni Rubis Passoni, Elisabetta Morandi, and Alfonso Capria. Functional evaluation of the endotics system, a new disposable self-propelled robotic colonoscope: in vitro tests and clinical trial. *The International journal of artificial organs*, 32(8):517–527, 2009.

[27] Revolutionary high-end, single use, self-propelled endoscopes enjoy the benefits of all worlds. https://consis-medical.com/. Accessed: 2018-07-25.

[28] Thomas Rösch, Andreas Adler, Heiko Pohl, Elke Wettschureck, Martin Koch, Bertram Wiedenmann, and Nicolas Hoepffner. A motor-driven single-use colonoscope controlled with a hand-held device: a feasibility study in volunteers. *Gastrointestinal endoscopy*, 67(7):1139–1146, 2008.

[29] Levin J Sliker and Gastone Ciuti. Flexible and capsule endoscopy for screening, diagnosis and treatment. *Expert Review of Medical Devices*, 11(6):649–666, 2014.

[30] Gang Chen, Minh Tu Pham, and Tanneguy Redarce. Sensor-based guidance control of a continuum robot for a semi-autonomous colonoscopy. *Robotics and autonomous systems*, 57(6-7):712–722, 2009.

[31] P. Valdastri, G. Ciuti, A. Verbeni, A. Menciassi, P. Dario, A. Arezzo, and M. Morino. Magnetic air capsule robotic system: proof of concept of a novel approach for painless colonoscopy. *Surgical Endoscopy*, 26(5):1238–1246, 2012.

[32] Chytra Pawashe, Steven Floyd, and Metin Sitti. Modeling and experimental characterization of an untethered magnetic micro-robot. *The International Journal of Robotics Research*, 28(8):1077–1094, 2009.

[33] Michael P Kummer, Jake J Abbott, Bradley E Kratochvil, Ruedi Borer, Ali Sengul, and Bradley J Nelson. Octomag: An electromagnetic system for 5-dof wireless micromanipulation. *IEEE Transactions on Robotics*, 26(6):1006–1017, 2010.

[34] Bumjin Jang, Emiliya Gutman, Nicolai Stucki, Benedikt F Seitz, Pedro D Wendel-García, Taylor Newton, Juho Pokki, Olgac Ergeneman, Salvador Pane, Yizhar Or, et al. Undulatory locomotion of magnetic multilink nanoswimmers. *Nano letters*, 15(7):4829–4833, 2015.

[35] Gábor Kósa, Péter Jakab, Ferenc Jólesz, and Nobuhiko Hata. Swimming capsule endoscope using static and rf magnetic field of mri for propulsion. In *Robotics and Automation, 2008. ICRA 2008. IEEE International Conference on*, pages 2922–2927. IEEE, 2008.

[36] Jean-Francois Rey, H Ogata, N Hosoe, K Ohtsuka, N Ogata, K Ikeda, H Aihara, I Pangtay, T Hibi, S Kudo, et al. Feasibility of stomach exploration with a guided capsule endoscope. *Endoscopy*, 42(07):541–545, 2010.

[37] Andrew J Petruska and Jake J Abbott. Omnimagnet: An omnidirectional electromagnet for controlled dipole-field generation. *IEEE Transactions on Magnetics*, 50(7):1–10, 2014.

[38] Viviane Lalande, Frederick P Gosselin, and Sylvain Martel. Catheter steering using a magnetic resonance imaging system. In *Engineering in Medicine and Biology Society (EMBC), 2010 Annual International Conference of the IEEE*, pages 1874–1877. IEEE, 2010.

[39] Maxime Latulippe and Sylvain Martel. Dipole field navigation: Theory and proof of concept. *IEEE Transactions on Robotics*, 31(6):1353–1363, 2015.

[40] Sylvain Martel. Beyond imaging: Macro-and microscale medical robots actuated by clinical mri scanners. *Science Robotics*, 2(3):eaam8119, 2017.

[41] Dominic R Frutiger, Karl Vollmers, Bradley E Kratochvil, and Bradley J Nelson. Small, fast, and under control: wireless resonant magnetic micro-agents. *The International Journal of Robotics Research*, 29(5):613–636, 2010.

[42] Eric Diller, Joshua Giltinan, and Metin Sitti. Independent control of multiple magnetic microrobots in three dimensions. *The International Journal of Robotics Research*, 32(5):614–631, 2013.

[43] Jakub Sikorski, Imro Dawson, Alper Denasi, Edsko EG Hekman, and Sarthak Misra. Introducing bigmaga novel system for 3d magnetic actuation of flexible surgical manipulators. In *Robotics and Automation (ICRA), 2017 IEEE International Conference on*, pages 3594–3599. IEEE, 2017.

[44] Arthur W Mahoney and Jake J Abbott. Five-degree-of-freedom manipulation of an untethered magnetic device in fluid using a single permanent magnet with application in stomach capsule endoscopy. *The International Journal of Robotics Research*, 35(1-3):129–147, 2016.

[45] Patrick Ryan and Eric Diller. Five-degree-of-freedom magnetic control of micro-robots using rotating permanent magnets. In *Robotics and Automation (ICRA), 2016 IEEE International Conference on*, pages 1731–1736. IEEE, 2016.

[46] Louis B Kratchman, Trevor L Bruns, Jake J Abbott, and Robert J Webster. Guiding elastic rods with a robot-manipulated magnet for medical applications. *IEEE Transactions on Robotics*, 33(1):227–233, 2017.

[47] Katie M Popek, Tucker Hermans, and Jake J Abbott. First demonstration of simultaneous localization and propulsion of a magnetic capsule in a lumen using a single rotating magnet. In *Robotics and Automation (ICRA), 2017 IEEE International Conference on*, pages 1154–1160. IEEE, 2017.

[48] Ilker Tunay. Modeling magnetic catheters in external fields. In *Engineering in Medicine and Biology Society, 2004. IEMBS'04. 26th Annual International Conference of the IEEE*, volume 1, pages 2006–2009. IEEE, 2004.

[49] Federico Carpi and Carlo Pappone. Magnetic maneuvering of endoscopic capsules by means of a robotic navigation system. *IEEE Transactions on Biomedical Engineering*, 56(5):1482–1490, 2009.

[50] Federico Carpi, Nathan Kastelein, Michael Talcott, and Carlo Pappone. Magnetically controllable gastrointestinal steering of video capsules. *IEEE Transactions on Biomedical Engineering*, 58(2):231–234, 2011.

[51] Gastone Ciuti, Pietro Valdastri, Arianna Menciassi, and Paolo Dario. Robotic magnetic steering and locomotion of capsule endoscope for diagnostic and surgical endoluminal procedures. *Robotica*, 28(2):199–207, 2010.

[52] Arthur W Mahoney and Jake J Abbott. Control of untethered magnetically actuated tools with localization uncertainty using a rotating permanent magnet. In *2012 4th IEEE RAS & EMBS International Conference on Biomedical Robotics and Biomechatronics (BioRob)*, pages 1632–1637. IEEE, 2012.

[53] Addisu Z. Taddese, Piotr R Slawinski, Marco Pirotta, Elena De Momi, Keith L. Obstein, and Pietro Valdastri. Enhanced real-time pose estimation for closed loop robotic manipulation of

magnetically actuated capsule endoscopes. *The International Journal of Robotics Research*, 37:890–911, 2018.

[54] Christophe Chautems and Bradley J Nelson. The tethered magnet: Force and 5-dof pose control for cardiac ablation. In *Robotics and Automation (ICRA), 2017 IEEE International Conference on*, pages 4837–4842. IEEE, 2017.

[55] Janis Edelmann, Andrew J Petruska, and Bradley J Nelson. Magnetic control of continuum devices. *The International Journal of Robotics Research*, 36(1):68–85, 2017.

[56] Alberto Arezzo, Arianna Menciassi, Pietro Valdastri, Gastone Ciuti, Gioia Lucarini, Marco Salerno, Christian Di Natali, Mauro Verra, Paolo Dario, and Mario Morino. Experimental assessment of a novel robotically-driven endoscopic capsule compared to traditional colonoscopy. *Digestive and liver disease*, 45(8):657–662, 2013.

[57] Janis Edelmann, Andrew J Petruska, and Bradley J Nelson. Estimation-based control of a magnetic endoscope without device localization. *Journal of Medical Robotics Research*, 3(01):1850002, 2018.

[58] Azad Shademan, Ryan S Decker, Justin D Opfermann, Simon Leonard, Axel Krieger, and Peter CW Kim. Supervised autonomous robotic soft tissue surgery. *Science translational medicine*, 8(337):337ra64–337ra64, 2016.

[59] Guang-Zhong Yang, James Cambias, Kevin Cleary, Eric Daimler, James Drake, Pierre E Dupont, Nobuhiko Hata, Peter Kazanzides, Sylvain Martel, Rajni V Patel, et al. Medical roboticsregulatory, ethical, and legal considerations for increasing levels of autonomy. *Sci. Robot*, 2(4):8638, 2017.

[60] Shane O'sullivan, Nathalie Nevejans, Colin Allen, Andrew Blyth, Simon Leonard, Ugo Pagallo, Katharina Holzinger, Andreas Holzinger, Mohammed Imran Sajid, and Hutan Ashrafian. Legal, regulatory, and ethical frameworks for development of standards in artifi-

cial intelligence (ai) and autonomous robotic surgery. *The International Journal of Medical Robotics and Computer Assisted Surgery*, 15(1):e1968, 2019.

[61] G Fagogenis, M Mencattelli, Z Machaidze, B Rosa, K Price, F Wu, V Weixler, M Saeed, JE Mayer, and PE Dupont. Autonomous robotic intracardiac catheter navigation using haptic vision. *Science Robotics*, 4(29):eaaw1977, 2019.

[62] Edward P Furlani. *Permanent magnet and electromechanical devices: materials, analysis, and applications*. Academic press, 2001.

[63] Andrew J Petruska and Jake J Abbott. Optimal permanent-magnet geometries for dipole field approximation. *IEEE transactions on magnetics*, 49(2):811–819, 2013.

[64] Andrew J Petruska, Arthur W Mahoney, and Jake J Abbott. Remote manipulation with a stationary computer-controlled magnetic dipole source. *IEEE Transactions on Robotics*, 30(5):1222–1227, 2014.

[65] Jake J Abbott, Kathrin E Peyer, Marco Cosentino Lagomarsino, Li Zhang, Lixin Dong, Ioannis K Kaliakatsos, and Bradley J Nelson. How should microrobots swim? *The international journal of Robotics Research*, 28(11-12):1434–1447, 2009.

[66] Chengzhi Hu, Salvador Pané, and Bradley J Nelson. Soft micro-and nanorobotics. *Annual Review of Control, Robotics, and Autonomous Systems*, 1:53–75, 2018.

[67] Jinxing Li, B Esteban-Fernández de Ávila, Wei Gao, Liangfang Zhang, and Joseph Wang. Micro/nanorobots for biomedicine: Delivery, surgery, sensing, and detoxification. *Sci. Robot.*, 2(4), 2017.

[68] Addisu Zerihun Taddese. *Magnetic Pose Estimation and Robotic Manipulation of Magnetically Actuated Capsule Endoscopes*. PhD thesis, 2018.

[69] Tsuneo Yoshikawa. Analysis and control of robot manipulators with redundancy. In

Robotics research: the first international symposium, pages 735–747. Mit Press Cambridge, MA, USA, 1984.

[70] Yoshihiko Nakamura. *Advanced robotics: redundancy and optimization*. Addison-Wesley Longman Publishing Co., Inc., 1990.

[71] Eric Diller, Joshua Giltinan, Guo Zhan Lum, Zhou Ye, and Metin Sitti. Six-degree-of-freedom magnetic actuation for wireless microrobotics. *The International Journal of Robotics Research*, 35(1-3):114–128, 2016.

[72] Andrew J Petruska and Bradley J Nelson. Minimum bounds on the number of electromagnets required for remote magnetic manipulation. *IEEE Transactions on Robotics*, 31(3):714–722, 2015.

[73] Piotr R Slawinski, Addisu Z Taddese, Kyle B Musto, Shabnam Sarker, Pietro Valdastri, and Keith L Obstein. Autonomously controlled magnetic flexible endoscope for colon exploration. *Gastroenterology*, 154(6):1577–1579, 2018.

[74] Morgan Quigley, Ken Conley, Brian Gerkey, Josh Faust, Tully Foote, Jeremy Leibs, Rob Wheeler, and Andrew Y Ng. Ros: an open-source robot operating system. In *ICRA workshop on open source software*, number 3.2, page 5. Kobe, 2009.

[75] Nathan P Koenig and Andrew Howard. Design and use paradigms for Gazebo, an open-source multi-robot simulator. In *IEEE/RSJ Int. Conf. Intell. Robot. Syst. (IROS 2004)*, Sendai, Japan, 2004.

[76] Michal F Kaminski, Jaroslaw Regula, Ewa Kraszewska, Marcin Polkowski, Urszula Wojciechowska, Joanna Didkowska, Maria Zwierko, Maciej Rupinski, Marek P Nowacki, and Eugeniusz Butruk. Quality indicators for colonoscopy and the risk of interval cancer. *New England Journal of Medicine*, 362(19):1795–1803, 2010.

[77] Moshe Rubin, Leigh Lurie, Konika Bose, and Sang H Kim. Expanding the view of a standard colonoscope with the third eye® panoramic cap. *World journal of gastroenterology: WJG*, 21(37):10683, 2015.

[78] Sujievvan Chandran, Frank Parker, Rhys Vaughan, Brent Mitchell, Scott Fanning, Gregor Brown, Jenny Yu, and Marios Efthymiou. Right-sided adenoma detection with retroflexion versus forward-view colonoscopy. *Gastrointestinal endoscopy*, 81(3):608–613, 2015.

[79] Robert E Sedlack, Vanessa M Shami, Douglas G Adler, Walter J Coyle, Barry DeGregorio, Kulwinder S Dua, Christopher J DiMaio, Linda S Lee, Lee McHenry, Shireen A Pais, et al. Colonoscopy core curriculum. *Gastrointestinal endoscopy*, 76(3):482–490, 2012.

[80] Anke M Leufkens, Daniel C DeMarco, Amit Rastogi, Paul A Akerman, Kassem Azzouzi, Richard I Rothstein, Frank P Vleggaar, Alessandro Repici, Giacomo Rando, Patrick I Okolo, et al. Effect of a retrograde-viewing device on adenoma detection rate during colonoscopy: the terrace study. *Gastrointestinal endoscopy*, 73(3):480–489, 2011.

[81] P. Valdastri, G. Ciuti, A. Verbeni, A. Menciassi, P. Dario, A. Arezzo, and M. Morino. Magnetic air capsule robotic system: proof of concept of a novel approach for painless colonoscopy. *Surgical endoscopy*, 26(5):1238–1246, 2012.

[82] Christian Di Natali, Marco Beccani, and Pietro Valdastri. Real-time pose detection for magnetic medical devices. *IEEE Transactions on Magnetics*.

[83] Christian Di Natali, Marco Beccani, Nabil Simaan, and Pietro Valdastri. Jacobian-based iterative method for magnetic localization in robotic capsule endoscopy. *IEEE Transactions on Robotics*, 32(2):327–338, 2016.

[84] T. D. Than, G. Alici, S. Harvey, G. O'Keefe, H. Zhou, W. Li, T. Cook, and S. Alam-Fotias. An effective localization method for robotic endoscopic capsules using multiple positron emission markers. *IEEE Transactions on Robotics*, 30(5):1174–1186, 2014.

[85] K. M. Popek and J. J. Abbott. 6-d localization of a magnetic capsule endoscope using a stationary rotating magnetic dipole field. *Hamlyn Symposium on Medical Robotics*, pages 47–48, 2015.

[86] A. Liegeois. Automatic supervisory control of the configuration and behavior of multibody mechanisms. *IEEE Transactions on Systems, Man, and Cybernetics*, 7(12):868–871, 1977.

[87] BNS Bhatnagar, CLN Sharma, SN Gupta, MM Mathur, and DCS Reddy. Study on the anatomical dimensions of the human sigmoid colon. *Clinical Anatomy*, 17(3):236–243, 2004.

[88] A. Alazmani, A. Hood, D. Jayne, A. Neville, and P. Culmer. Quantitative assessment of colorectal morphology: Implications for robotic colonoscopy. *Medical engineering & physics*, 38(2):148–154, 2016.

[89] Gideon Sandler, Sarah Leishman, Helen Branson, Craig Buchan, and Andrew JA Holland. Body wall thickness in adults and children—relevance to penetrating trauma. *Injury*, 41(5):506–509, 2010.

[90] Viacheslav I Egorov, Ilia V Schastlivtsev, Edward V Prut, Andrey O Baranov, and Robert A Turusov. Mechanical properties of the human gastrointestinal tract. *Journal of biomechanics*, 35(10):1417–1425, 2002.

[91] HD Hoeg, A Brett Slatkin, Joel W Burdick, and Warren S Grundfest. Biomechanical modeling of the small intestine as required for the design and operation of a robotic endoscope. In *Robotics and Automation, 2000. Proceedings. ICRA'00. IEEE International Conference on*, volume 2, pages 1599–1606. IEEE, 2000.

[92] Ryan E Childers, J Lucas Williams, and Amnon Sonnenberg. Practice patterns of sedation for colonoscopy. *Gastrointestinal endoscopy*, 82(3):503–511, 2015.

[93] C. Di Natali, M. Beccani, K. L. Obstein, and P. Valdastri. A wireless platform for in vivo measurement of resistance properties of the gastrointestinal tract. *Physiological measurement*, 35(7):1197, 2014.

[94] Levin J Sliker, Gastone Ciuti, Mark E Rentschler, and Arianna Menciassi. Frictional resistance model for tissue-capsule endoscope sliding contact in the gastrointestinal tract. *Tribology International*, 2016.

[95] M. Moshkowitz, Y. Hirsch, I. Carmel, T. Duvdevany, I. Fabian, E. P. Willenz, and J. Cohen. A novel device for rapid cleaning of poorly prepared colons. *Endoscopy*, 42(10):834–836, 2010.

[96] *Joseph C Norton, *Piotr R Slawinski, Holly S Lay, James W Martin, Benjamin F Cox, Gerard Cummins, Marc Desmulliez, Richard E Clutton, Keith L Obstein, Sandy Cochran, and Pietro Valdastri. Intelligent magnetic manipulation for gastrointestinal ultrasound *(* indicates equal contribution) In-Press. Science Robotics*, 4(31):eaav7725, 2019.

[97] Armando Peixoto, Marco Silva, Pedro Pereira, and Guilherme Macedo. Biopsies in gastrointestinal endoscopy: When and how. *GE Portuguese journal of gastroenterology*, 23(1):19–27, 2016.

[98] Roger M Feakins. Inflammatory bowel disease biopsies: updated british society of gastroenterology reporting guidelines. *Journal of clinical pathology*, 66(12):1005–1026, 2013.

[99] Michael D Yao, Erik C von Rosenvinge, Catherine Groden, and Peter J Mannon. Multiple endoscopic biopsies in research subjects: safety results from a national institutes of health series. *Gastrointestinal endoscopy*, 69(4):906–910, 2009.

[100] Anouar Teriaky, Abdullah AlNasser, Carolyn McLean, James Gregor, and Brian Yan. The utility of endoscopic biopsies in patients with normal upper endoscopy. *Canadian Journal of Gastroenterology and Hepatology*, 2016, 2016.

[101] Alina Boeriu, Cristian Boeriu, Silvia Drasovean, Ofelia Pascarenco, Simona Mocan, Mircea Stoian, and Daniela Dobru. Narrow-band imaging with magnifying endoscopy for the evaluation of gastrointestinal lesions. *World journal of gastrointestinal endoscopy*, 7(2):110, 2015.

[102] PSP Thong, M Olivo, WWL Chin, R Bhuvaneswari, K Mancer, and KC Soo. Clinical application of fluorescence endoscopic imaging using hypericin for the diagnosis of human oral cavity lesions. *British journal of cancer*, 101(9):1580, 2009.

[103] Neel Sharma, Nobuyoshi Takeshita, and Khek Yu Ho. Raman spectroscopy for the endoscopic diagnosis of esophageal, gastric, and colonic diseases. *Clinical endoscopy*, 49(5):404, 2016.

[104] Nathan Gluck, Beni Shpak, Rita Brun, Thomas Rösch, Nadir Arber, and Menachem Moshkowitz. A novel prepless x-ray imaging capsule for colon cancer screening. *Gut*, 65(3):371–373, 2016.

[105] Nadir Ghanem, Carsten Altehoefer, Alex Furtwängler, Jan Winterer, Oliver Schäfer, Oliver Springer, Elmar Kotter, and Mathias Langer. Computed tomography in gastrointestinal stromal tumors. *European radiology*, 13(7):1669–1678, 2003.

[106] Ehab M Kamel, Miriam Thumshirn, Kaspar Truninger, Marc Schiesser, Michael Fried, Barbara Padberg, Didier Schneiter, Sandro J Stoeckli, Gustav K Von Schulthess, and Katrin DM Stumpe. Significance of incidental 18f-fdg accumulations in the gastrointestinal tract in pet/ct: correlation with endoscopic and histopathologic results. *Journal of Nuclear Medicine*, 45(11):1804–1810, 2004.

[107] K Inui, S Nakazawa, J Yoshino, K Yamao, H Yamachika, T Wakabayashi, N Kanemaki, and H Hidano. Endoscopic mri: preliminary results of a new technique for visualization and staging of gastrointestinal tumors. *Endoscopy*, 27(07):480–485, 1995.

[108] Tsung-Han Tsai, James G Fujimoto, and Hiroshi Mashimo. Endoscopic optical coherence tomography for clinical gastroenterology. *diagnostics*, 4(2):57–93, 2014.

[109] Eugene P DiMagno and Matthew J DiMagno. Endoscopic ultrasonography: from the origins to routine eus. *Digestive diseases and sciences*, 61(2):342–353, 2016.

[110] Svein Ødegaard, Lars B Nesje, Ole Didrik Lærum, and Michael B Kimmey. High-frequency ultrasonographic imaging of the gastrointestinal wall. *Expert review of medical devices*, 9(3):263–273, 2012.

[111] J Due-Hansen, K Midtbø, E Poppe, A Summanwar, GU Jensen, L Breivik, DT Wang, and K Schjølberg-Henriksen. Fabrication process for cmut arrays with polysilicon electrodes, nanometre precision cavity gaps and through-silicon vias. *Journal of Micromechanics and Microengineering*, 22(7):074009, 2012.

[112] HS Lay, Y Qiu, M Al-Rawhani, J Beeley, R Poltarjonoks, V Seetohul, D Cumming, S Cochran, G Cummins, MPY Desmulliez, et al. Progress towards a multi-modal capsule endoscopy device featuring microultrasound imaging. *2016 Ieee International Ultrasonics Symposium (Ius)*, 2016.

[113] Daniel Rohrbach, Brian Wodlinger, Jerrold Wen, Jonathan Mamou, and Ernest Feleppa. High-frequency quantitative ultrasound for imaging prostate cancer using a novel micro-ultrasound scanner. *Ultrasound in medicine & biology*, 44(7):1341–1354, 2018.

[114] Benjamin F Cox, Fraser Stewart, Holly Lay, Gerard Cummins, Ian P Newton, Marc PY Desmulliez, Robert JC Steele, Inke Näthke, and Sandy Cochran. Ultrasound capsule endoscopy: Sounding out the future. *Annals of translational medicine*, 5(9), 2017.

[115] Cecile Delgorge, Fabien Courrèges, L Al Bassit, Cyril Novales, Christophe Rosenberger, Natalie Smith-Guerin, Concepció Brù, Rosa Gilabert, Maurizio Vannoni, Gérard Poisson, et al. A tele-operated mobile ultrasound scanner using a light-weight robot. *IEEE Transactions on Information Technology in Biomedicine*, 9(1):50–58, 2005.

[116] Shuyang Chen, Jianren Wang, and Peter Kazanzides. Integration of a low-cost three-axis sensor for robot force control. In *2018 Second IEEE International Conference on Robotic Computing (IRC)*, pages 246–249. IEEE, 2018.

[117] Matthew W Gilbertson and Brian W Anthony. Force and position control system for free-hand ultrasound. *IEEE Transactions on Robotics*, 31(4):835–849, 2015.

[118] Philippe Arbeille, Jose Ruiz, Philippe Herve, Muriel Chevillot, Gerard Poisson, and Frank Perrotin. Fetal tele-echography using a robotic arm and a satellite link. *Ultrasound in obstetrics & gynecology*, 26(3):221–226, 2005.

[119] Farshid Najafi and Nariman Sepehri. A novel hand-controller for remote ultrasound imaging. *Mechatronics*, 18(10):578–590, 2008.

[120] Victor G Maturo, Noel R Zusmer, Albert J Gilson, William M Smoak, Warren R Janowitz, Barbara E Bear, John Goddard, and Donald E Dick. Ultrasound of the whole breast utilizing a dedicated automated breast scanner. *Radiology*, 137(2):457–463, 1980.

[121] Misop Han, Chunwoo Kim, Pierre Mozer, Felix Schäfer, Shadie Badaan, Bogdan Vigaru, Kenneth Tseng, Doru Petrisor, Bruce Trock, and Dan Stoianovici. Tandem-robot assisted laparoscopic radical prostatectomy to improve the neurovascular bundle visualization: a feasibility study. *Urology*, 77(2):502–506, 2011.

[122] Caitlin M Schneider, Peter D Peng, Russell H Taylor, Gregory W Dachs II, Christopher J Hasser, Simon P DiMaio, and Michael A Choti. Robot-assisted laparoscopic ultrasonography for hepatic surgery. *Surgery*, 151(5):756–762, 2012.

[123] Paul Mignon, Philippe Poignet, and Jocelyne Troccaz. Automatic robotic steering of flexible needles from 3d ultrasound images in phantoms and ex vivo biological tissue. *Annals of biomedical engineering*, pages 1–12, 2018.

[124] Salvatore Virga, Oliver Zettinig, Marco Esposito, Karin Pfister, Benjamin Frisch, Thomas Neff, Nassir Navab, and Christoph Hennersperger. Automatic force-compliant robotic ultrasound screening of abdominal aortic aneurysms. In *Intelligent Robots and Systems (IROS), 2016 IEEE/RSJ International Conference on*, pages 508–513. IEEE, 2016.

[125] Salvatore Virga, Rüdiger Göbl, Maximilian Baust, Nassir Navab, and Christoph Hennersperger. Use the force: deformation correction in robotic 3d ultrasound. *International journal of computer assisted radiology and surgery*, 13(5):619–627, 2018.

[126] Samuel B Kesner and Robert D Howe. Robotic catheter cardiac ablation combining ultrasound guidance and force control. *The International Journal of Robotics Research*, 33(4):631–644, 2014.

[127] Max L Balter, Alvin I Chen, Timothy J Maguire, and Martin L Yarmush. Adaptive kinematic control of a robotic venipuncture device based on stereo vision, ultrasound, and force guidance. *IEEE Transactions on Industrial Electronics*, 64(2):1626–1635, 2017.

[128] Pierre Chatelain, Alexandre Krupa, and Nassir Navab. 3d ultrasound-guided robotic steering of a flexible needle via visual servoing. In *IEEE Int. Conf. on Robotics and Automation, ICRA'15*, 2015.

[129] Caroline Nadeau, Hongliang Ren, Alexandre Krupa, and Pierre Dupont. Intensity-based visual servoing for instrument and tissue tracking in 3d ultrasound volumes. *IEEE Transactions on Automation Science and Engineering*, 12(1):367–371, 2015.

[130] Mickaël Sauvée, Philippe Poignet, and Etienne Dombre. Ultrasound image-based visual servoing of a surgical instrument through nonlinear model predictive control. *The International Journal of Robotics Research*, 27(1):25–40, 2008.

[131] Paul M Novotny, Jeffrey A Stoll, Pierre E Dupont, and Robert D Howe. Real-time visual servoing of a robot using three-dimensional ultrasound. In *Robotics and Automation, 2007 IEEE International Conference on*, pages 2655–2660. IEEE, 2007.

[132] J Hong, Takeyoshi Dohi, Makoto Hashizume, K Konishi, and N Hata. An ultrasound-driven needle-insertion robot for percutaneous cholecystostomy. *Physics in Medicine & Biology*, 49(3):441, 2004.

[133] Gustaaf J Vrooijink, Momen Abayazid, Sachin Patil, Ron Alterovitz, and Sarthak Misra. Needle path planning and steering in a three-dimensional non-static environment using two-dimensional ultrasound images. *The International journal of robotics research*, 33(10):1361–1374, 2014.

[134] Shuangyi Wang, James Housden, Davinder Singh, and Kawal Rhode. Automatic adjustments of a trans-oesophageal ultrasound robot for monitoring intra-operative catheters. In *IOP Conference Series: Materials Science and Engineering*, volume 280, page 012032. IOP Publishing, 2017.

[135] Deukhee Lee and Alexandre Krupa. Intensity-based visual servoing for non-rigid motion compensation of soft tissue structures due to physiological motion using 4d ultrasound. In *Intelligent Robots and Systems (IROS), 2011 IEEE/RSJ International Conference on*, pages 2831–2836. IEEE, 2011.

[136] Alexandre Krupa, David Folio, Cyril Novales, Pierre Vieyres, and Tao Li. Robotized tele-echography: an assisting visibility tool to support expert diagnostic. *IEEE Systems Journal*, 10(3):974–983, 2016.

[137] Purang Abolmaesumi, Septimiu E Salcudean, Wen-Hong Zhu, Mohammad Reza Sirouspour, and Simon Peter DiMaio. Image-guided control of a robot for medical ultrasound. *IEEE Transactions on Robotics and Automation*, 18(1):11–23, 2002.

[138] Rafik Mebarki, Alexandre Krupa, and François Chaumette. 2-d ultrasound probe complete guidance by visual servoing using image moments. *IEEE Transactions on Robotics*, 26(2):296–306, 2010.

[139] Alexandre Krupa, Gabor Fichtinger, and Gregory D Hager. Real-time motion stabilization with b-mode ultrasound using image speckle information and visual servoing. *The International Journal of Robotics Research*, 28(10):1334–1354, 2009.

[140] Deborah R Kaye, Dan Stoianovici, and Misop Han. Robotic ultrasound and needle guidance for prostate cancer management: review of the contemporary literature. *Current opinion in urology*, 24(1):75, 2014.

[141] MP Brewin, LC Pike, DE Rowland, and MJ Birch. The acoustic properties, centered on 20 mhz, of an iec agar-based tissue-mimicking material and its temperature, frequency and age dependence. *Ultrasound in medicine & biology*, 34(8):1292–1306, 2008.

[142] C Atuma, V Strugala, A Allen, and Lena Holm. The adherent gastrointestinal mucus gel layer: thickness and physical state in vivo. *American Journal of Physiology-Gastrointestinal and Liver Physiology*, 280(5):G922–G929, 2001.

[143] Rohit Chandra, Anders J Johansson, Mats Gustafsson, and Fredrik Tufvesson. A microwave imaging-based technique to localize an in-body rf source for biomedical applications. *IEEE Transactions on Biomedical Engineering*, 62(5):1231–1241, 2015.

[144] Kaveh Pahlavan, Guanqun Bao, Yunxing Ye, Sergey Makarov, Umair Khan, Pranay Swar, D Cave, Andrew Karellas, Prashant Krishnamurthy, and Kamran Sayrafian. Rf localization for wireless video capsule endoscopy. *International Journal of Wireless Information Networks*, 19(4):326–340, 2012.

[145] Michael Fluckiger and Bradley J Nelson. Ultrasound emitter localization in heterogeneous media. In *Engineering in Medicine and Biology Society, 2007. EMBS 2007. 29th Annual International Conference of the IEEE*, pages 2867–2870. IEEE, 2007.

[146] Trung Duc Than, Gursel Alici, Hao Zhou, Steven Harvey, and Weihua Li. Enhanced localization of robotic capsule endoscopes using positron emission markers and rigid-body

transformation. *IEEE Transactions on Systems, Man, and Cybernetics: Systems*, (99):1–15, 2017.

[147] Donghoon Son, Sehyuk Yim, and Metin Sitti. A 5-d localization method for a magnetically manipulated untethered robot using a 2-d array of hall-effect sensors. *IEEE/ASME Transactions on Mechatronics*, 21(2):708–716, 2016.

[148] Xudong Guo, Cheng Wang, and Rongguo Yan. An electromagnetic localization method for medical micro-devices based on adaptive particle swarm optimization with neighborhood search. *Measurement*, 44(5):852–858, 2011.

[149] Tsuneo Yoshikawa. Manipulability of robotic mechanisms. *The international journal of Robotics Research*, 4(2):3–9, 1985.

[150] Xin Li, Xilun Ding, and Gregory S Chirikjian. Analysis of angular-error uncertainty in planar multiple-loop structures with joint clearances. *Mechanism and Machine Theory*, 91:69–85, 2015.

[151] Pasquale Chiacchio, Stefano Chiaverini, Lorenzo Sciavicco, and Bruno Siciliano. Global task space manipulability ellipsoids for multiple-arm systems. *IEEE Transactions on Robotics and Automation*, 7(5):678–685, 1991.

[152] Lorenzo Sciavicco and Bruno Siciliano. *Modelling and control of robot manipulators*. Springer Science & Business Media, 2012.

[153] Alain Liegeois. Automatic supervisory control of the configuration and behavior of multibody mechanisms. *IEEE transactions on systems, man, and cybernetics*, 7(12):868–871, 1977.

[154] K Somani Arun, Thomas S Huang, and Steven D Blostein. Least-squares fitting of two 3-d point sets. *IEEE Transactions on pattern analysis and machine intelligence*, 9(5):698–700, 1987.

[155] Marco Salerno, Gastone Ciuti, Gioia Lucarini, Rocco Rizzo, Pietro Valdastri, Arianna Menciassi, Alberto Landi, and Paolo Dario. A discrete-time localization method for capsule endoscopy based on on-board magnetic sensing. *Measurement Science and Technology*, 23(1):015701, jan 2012.

[156] Katie M Popek, Thomas Schmid, and Jake J Abbott. Six-Degree-of-Freedom Localization of an Untethered Magnetic Capsule Using a Single Rotating Magnetic Dipole. *IEEE Robotics and Automation Letters*, 2(1):305–312, jan 2017.

[157] M. Salerno, R. Rizzo, E. Sinibaldi, and A. Menciassi. Force calculation for localized magnetic driven capsule endoscopes. In *IEEE International Conference on Robotics and Automation*, pages 5354–5359, 2013.

[158] Olgaç Ergeneman, Görkem Dogangil, Michael P Kummer, Jake J Abbott, Mohammad K Nazeeruddin, and Bradley J Nelson. A magnetically controlled wireless optical oxygen sensor for intraocular measurements. *IEEE Sensors Journal*, 8(1):29–37, 2008.

[159] Jake J Abbott, Olgaç Ergeneman, Michael P Kummer, Ann M Hirt, and Bradley J Nelson. Modeling magnetic torque and force for controlled manipulation of soft-magnetic bodies. *IEEE Transactions on Robotics*, 23(6):1247–1252, 2007.

[160] Vi NT Le, Nghia H Nguyen, Kamal Alameh, Rukshen Weerasooriya, and Peter Pratten. Accurate modeling and positioning of a magnetically controlled catheter tip. *Medical physics*, 43(2):650–663, 2016.

[161] Bruno Scaglioni, Luca Previtera, James Martin, Joseph Norton, Keith L Obstein, and Pietro Valdastri. Explicit model predictive control of a magnetic flexible endoscope. *IEEE Robotics and Automation Letters*, 2018.

[162] Kevin M Lynch and Frank C Park. *Modern Robotics*. Cambridge University Press, 2017.

[163] Andrew Orekhov, Colette Abah, and Nabil Simaan. Snake-like robots for minimally invasive, single port, and intraluminal surgeries. *The Encyclopedia of Medical Robotics*, 1, 2018.

[164] MK Konings, EB Van de Kraats, T Alderliesten, and WJ Niessen. Analytical guide wire motion algorithm for simulation of endovascular interventions. *Medical and Biological Engineering and Computing*, 41(6):689–700, 2003.

[165] Mahta Khoshnam, Mahdi Azizian, and Rajni V Patel. Modeling of a steerable catheter based on beam theory. In *2012 IEEE International Conference on Robotics and Automation*, pages 4681–4686. IEEE, 2012.

[166] Gregory S Chirikjian. Conformational modeling of continuum structures in robotics and structural biology: A review. *Advanced Robotics*, 29(13):817–829, 2015.

[167] Jessica Burgner-Kahrs, D Caleb Rucker, and Howie Choset. Continuum robots for medical applications: A survey. *IEEE Transactions on Robotics*, 31(6):1261–1280, 2015.

[168] Robert J Webster III and Bryan A Jones. Design and kinematic modeling of constant curvature continuum robots: A review. *The International Journal of Robotics Research*, 29(13):1661–1683, 2010.

[169] Tipakorn Greigarn, Russell Jackson, Taoming Liu, and M Cenk Çavuşoğlu. Experimental validation of the pseudo-rigid-body model of the mri-actuated catheter. In *2017 IEEE International Conference on Robotics and Automation (ICRA)*, pages 3600–3605. IEEE, 2017.

[170] D Caleb Rucker, Bryan A Jones, and Robert J Webster III. A geometrically exact model for externally loaded concentric-tube continuum robots. *IEEE transactions on robotics: a publication of the IEEE Robotics and Automation Society*, 26(5):769, 2010.

[171] Kai Xu and Nabil Simaan. Analytic formulation for kinematics, statics, and shape restora-

tion of multibackbone continuum robots via elliptic integrals. *Journal of Mechanisms and Robotics*, 2(1):011006, 2010.

[172] Seok Chang Ryu and Pierre E Dupont. Fbg-based shape sensing tubes for continuum robots. In *2014 IEEE International Conference on Robotics and Automation (ICRA)*, pages 3531–3537. IEEE, 2014.

[173] Beobkyoon Kim, Junhyoung Ha, Frank C Park, and Pierre E Dupont. Optimizing curvature sensor placement for fast, accurate shape sensing of continuum robots. In *2014 IEEE international conference on robotics and automation (ICRA)*, pages 5374–5379. IEEE, 2014.

[174] Stephen Tully, George Kantor, Marco A Zenati, and Howie Choset. Shape estimation for image-guided surgery with a highly articulated snake robot. In *2011 IEEE/RSJ International Conference on Intelligent Robots and Systems*, pages 1353–1358. IEEE, 2011.

[175] Chaoyang Shi, Xiongbiao Luo, Peng Qi, Tianliang Li, Shuang Song, Zoran Najdovski, Toshio Fukuda, and Hongliang Ren. Shape sensing techniques for continuum robots in minimally invasive surgery: A survey. *IEEE Transactions on Biomedical Engineering*, 64(8):1665–1678, 2017.

[176] Deepak Trivedi and Christopher D Rahn. Model-based shape estimation for soft robotic manipulators: The planar case. *Journal of Mechanisms and Robotics*, 6(2):021005, 2014.

[177] Deepak Trivedi, Amir Lotfi, and Christopher D Rahn. Geometrically exact models for soft robotic manipulators. *IEEE Transactions on Robotics*, 24(4):773–780, 2008.

[178] Vilas K Chitrakaran, Aman Behal, Darren M Dawson, and Ian D Walker. Setpoint regulation of continuum robots using a fixed camera. *Robotica*, 25(5):581–586, 2007.

[179] G. Bradski. The OpenCV Library. *Dr. Dobb's Journal of Software Tools*, 2000.

[180] T. F. Chan and R. V. Dubey. A weighted least-norm solution based scheme for avoiding joint

limits for redundant joint manipulators. *IEEE Transactions on Robotics and Automation*, 11(2):286–292, 1995.

[181] Michael A Henson and Dale E Seborg. *Nonlinear process control*. Prentice Hall PTR Upper Saddle River, New Jersey, 1997.

[182] Benjamin S Terry, Allison B Lyle, Jonathan A Schoen, and Mark E Rentschler. Preliminary mechanical characterization of the small bowel for in vivo robotic mobility. *Journal of biomechanical engineering*, 133(9):091010, 2011.